Toward Accurate and Large-scale Silicon Photonics

by

Jie Sun

Submitted to the Department of Electrical Engineering and Computer Science in partial fulfillment of the requirements for the degree of

Doctor of Philosophy in Electrical Engineering

at the

MASSACHUSETTS INSTITUTE OF TECHNOLOGY

Feburary 2013

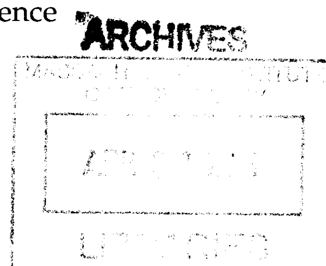

© Massachusetts Institute of Technology 2013. All rights reserved.

Author ....
Department of Electrical Engineering and Computer Science
Feburary 1, 2013

Certified by ....
Michael R. Watts
Associate Professor of Electrical Engineering
Thesis Supervisor

Certified by ....
Henry I. Smith
Professor of Electrical Engineering
Thesis Supervisor

Accepted by ....
Leslie Kolodziejski
Chairman, Department Committee on Graduate Students

Toward Accurate and Large-scale Silicon Photonics

by

Jie Sun

Submitted to the Department of Electrical Engineering and Computer Science
on Feburary 1, 2013, in partial fulfillment of the
requirements for the degree of
Doctor of Philosophy in Electrical Engineering

Abstract

Silicon photonics, emerging from the interface of silicon technology and photonic technology, is expected to inherit the incredible integration ability of silicon technology that has boomed the microelectronic industry for half a century, as well as the unparalleled communication capability of photonic technology that has revolutionized the information industry for decades. Being a prevailing research topic in the past decade, silicon photonics has seen tremendous progresses with the successful demonstrations and commercializations of almost all of the key components, including on-chip light source, low-loss silicon waveguide, and ultrafast silicon modulators and detectors. It seems silicon photonics is ready to take off by following the successful path the microelectronic industry has been traveling through to achieve a large-scale integration of millions of photonic devices on the silicon chip with the aide of the well-established complementary metal-oxide-semiconductor (CMOS) technology.

However, there remain some substantial challenges in silicon photonics, including the reliable design and fabrication of silicon photonic devices with unprecedented accuracy, and the large-scale integration of otherwise discrete silicon photonic devices. To this end, this thesis explored several examples as possible means of addressing these two challenges in silicon photonics. Two different ways of improving silicon photonic device accuracy were presented from perspectives of fabrication and device design respectively, followed by a successful integration demonstration where more than 4,000 components worked together on a silicon chip to form a functional large-scale silicon photonic system, representing the largest silicon photonic integration demonstrated to date.

Thesis Supervisor: Michael R. Watts
Title: Associate Professor of Electrical Engineering

Thesis Supervisor: Henry I. Smith
Title: Professor of Electrical Engineering

Acknowledgments

The journey of attaining a Ph.D. in engineering, particularly at MIT, is a unique experience filled with depression and excitement, frustration and success. Ph.D is not only a degree but also a kind of life in which we fall, we learn, and we grow. It is a worthful journey with hard work that ultimately paid off. My journey at MIT would not be so wonderful without any of the following people I would like to give my heartful thanks to.

First and foremost, I would like to thank my advisors, professors Michael R. Watts and Henry I. Smith. I am always grateful to have the opportunity to work with two outstanding experts in different but closely-related research areas like Mike and Hank. This gives me great privilege to enrich my research experience from device design to fabrication. Without Mike's persistence, the achievement made in this thesis work would not come true. He never gives up hope on anything even when everyone else thinks it is impossible to accomplish. While Hank gives his students exceptional freedom to try different things in research, his door is always open for discussions. I am especially impressed by his passion and diligence in work as well as his remarkable scientific inquisitiveness.

I would like to thank Prof. Erich P. Ippen for serving my thesis committee and for giving me valuable advices on my thesis work. I would also like to thank Prof. Vladimir Stojanović, Prof. Rajeev Ram, and Prof. Franz X. Kärtner for their generous financial support and insightful technical discussions on my Ph.D. work. I would also like to thank Prof. Jeffrey Todd Hastings of University of Kentuky, Prof. Thomas E. Murphy of University of Maryland, Prof. Minghao Qi of Purdue University, and Prof. Miloš Popović of University of Colorado for their helps with various projects I was involved at MIT.

One of the amazing treasures of MIT is its students. During my years at MIT, I was privileged to have the opportunity to work with the most brilliant engineering students in the world. I would like to give special thanks to Dr. Trey Holzwarth and Dr. Marcus Dahlem who helped me a lot with my research in the first two

years of my Ph.D. study. I would like to thank my officemates Erman Timurdoğan, Ami Yaacobi, Dr. Sidney Tsai, Linlee Cheong, Dr. Thomas Reisinger, and Dr. Shabnam Ghadarghadr for the research discussions and for making my work time so joyful at MIT. In addition, I would like to thank all the people in the Photonic Microystems Group and the NanoStructures Laboratory, and also the POEM team and EPIC team at MIT. Special thanks also give to Jim Daley and Mark K. Mondol for coordinating the lab logistics with great patience.

Last but not least, I would like to thank my parents Xizhang Sun and Juan Wang in China. I am always feeling their unconditional love even I am geographically apart from home.

To

my parents Xizhang Sun, and Juan Wang

and

grandparents Hongjun Sun, and Shijun Wang

Contents

Chapter 1 Introduction 15

1.1 Silicon Photonics 15

1.2 Challenges in Silicon Photonics 21

Part I Toward Accurate Silicon Photonic Devices 25

Chapter 2 Accurate Device by Improved Nanofabrication 27

2.1 Frequency Mismatch and Intrafield Distortion 28

2.2 Intrafield Distortion Induced Frequency Mismatch 34

2.3 Intrafield Distortion Correction 38

Chapter 3 Accurate Device by Advanced Design 43

3.1 Basics of Bragg Gratings 44

3.2 Sampled Bragg Grating 50

3.2.1 Ordinary Sampled Bragg Grating 50

3.2.2 Sampled Bragg Grating with Arbitrary Filter Shapes 52

3.2.3 Sampled Bragg Grating with Phase Shift 59

3.3 Measured SBG with Phase Shift 64

Part II Toward Large-scale Silicon Photonic Integration **71**

Chapter 4 Nanophotonic Phased Array: Theory **73**
4.1 1-Dimensional Optical Phased Array 74
4.1.1 A Revisit to Young's Interference Experiment 74
4.1.2 Phased Array: A Fourier System 77
4.2 Large-scale 2-Dimensional Phased Array 80
4.3 Noise Analysis of Large-scale Phased Array 86
Chapter 5 Large-scale Passive Phased Array **93**
5.1 Device Design: Dielectric Nanoantenna 94
5.1.1 Minimizing the Back-reflection 95
5.1.2 Minimizing the Down-emission 97
5.2 System Design: Power Balance and Phase Alignment 104
5.2.1 Optical Power Distribution 104
5.2.2 Optical Phase Management 110
5.3 The Fabricated 64×64 Nanophotonic Phased Array 111
5.4 Image Noise in Nanophotonic Phased Array 119
Chapter 6 Large-scale Active Phased Array **125**
6.1 Integrated Silicon Thermo-optic Heater 125
6.2 8×8 Active Phased Array 132
6.3 Amplitude-modulated Phased Array 140

Chapter 7 Conclusions and Perspectives **149**
7.1 Summary of Accomplishments 149
7.2 Future Work 150

Bibliography **155**

List of Figures

1-1 A schematic of an on-chip silicon photonic link. 17

1-2 A gallery of representative silicon photonic devices demonstrated to date. 19

2-1 Frequency mismatch in high-order microring resonators. 29

2-2 Illustration of the intrafield distortion problem in SEBL. 30

2-3 Measurement method of the intrafield distortion in the SEBL system. 32

2-4 Measured intrafield distortion in a Raith 150 SEBL system at MIT. . . 33

2-5 The structure of the waveguides used in the experimental demonstration. 36

2-6 Experimental validation of the correlation between the intrafield distortion in the SEBL and the frequency mismatch in high-order microring resonators. 37

2-7 Measured filter spectra of a second-order microring resonator with and without intrafield distortion correction. 39

2-8 Statistical result of the frequency mismatch of a number of second-order microring resonators with and without intrafield distortion correction. 40

3-1 Schematic of a uniform grating on a stripe waveguide. 45
3-2 Modeling of the Bragg grating based on the perturbation theory. . . . 46
3-3 Simulated transmission and reflection spectra of a typical uniform Bragg grating. 49
3-4 A Schematic of an ordinary sampled Bragg grating on a ridge waveguide. 52
3-5 Simulated reflection and transmission spectra of a typical SBG. 53
3-6 SBG with a non-periodic sampling function $S_1(z)$ to achieve arbitrary filter shape. 55
3-7 Design of the SBG with arbitrary filter shape. 56
3-8 Simulated SBG reflection spectrum with the targeted filter shape in the $-1^{tt}channel$. 58
3-9 Ordinary phase-shifted Bragg grating. 61
3-10 Sampled Bragg Grating with a phase shift. 62
3-11 Fabrication process flow for the phase-shift Bragg gratings using the SBG structure. 65
3-12 A schematic of the cross-section of the silicon ridge waveguide with grating on top. 66
3-13 SEMs of the fabricated SBG. 67
3-14 Measured transmission spectrum of the fabricated SBG. 68

4-1 A 1-D optical phased array. 75
4-2 The far-field simulation of 1-D optical phased array. 76
4-3 Fourier transform interpretation of 1-D optical phased array. 78
4-4 2-D phased array. 81
4-5 The modified Gerchberg-Saxton (GS) method. 83
4-6 Phased array synthesis with modified GS algorithm. 84
4-7 Convergence of the modified GS algorithm. 85
4-8 Simulated far-field pattern when $\Delta_x = \Delta_y \gg \lambda/2$. 86
4-9 Far-field simulation of large-scale phased array under phase noise. . 89

4-10 Far-field SNR under different near-field phase noise. 90

5-1 Schematics of optical nanoantenna design. 95

5-2 Minimization of back-reflection in dielectric nanoantennas. 96

5-3 Antenna emission angle due to grating period detuning. 98

5-4 Asymmetric structure to have more up-emission. 99

5-5 Emitting efficiency of the optical antennas. 101

5-6 Near-field and far-field simulations of the proposed optical nanoantennas. 102

5-7 Scanning-electron-micrograph of the fabricated optical nanoantenna. 104

5-8 Schematic of conventional optical phased array architecture. 105

5-9 Schematic of the proposed architecture for the large-scale nanophotonic phased array. 106

5-10 Power distribution scheme in large-scale phased array with uniform emission. 108

5-11 The bus-to-row and row-to-unit coupler lengths to achieve uniform emission in a 64×64 phased array. 108

5-12 An individual pixel in the large-scale nanophotonic phased array. . . 111

5-13 Optical and scanning-electron images of the fabricated 64×64 nanophotonic phased array. 112

5-14 A schematic of the near and far field measurement setup. 113

5-15 Near-field measurement. 114

5-16 Fourier relation between the near-field emission and its far-field pattern. 115

5-17 A close-up image of the simulated viewable far field. 116

5-18 Measured far-field patterns of a 64×64 phased array and a 32×32 phased array. 118

5-19 The multiple reflection of the down-emission in phased arrays. 120

5-20 Far-field simulations with multiple reflection from the down-emission taken into account. 122

5-21 Far-field simulations with white phase noise considered. 124

6-1 Schematics of thermo-optic heater configurations. 127
6-2 Electrical connections with adiabatic waveguide bend. 130
6-3 Schematic of an active pixel with a tunable phase shifter in the tunable phased array. 132
6-4 Schematic of an 8×8 active phased array. 133
6-5 Optical micrograph of a fabricated 8×8 active phased array. 134
6-6 Experimental results of the 8×8 active phased array for beam steering and shaping. 136
6-7 The beam splitting mechanism of the 8×8 nanophotonic phased array. 137
6-8 Illustration of side lobes in the 8×8 nanophotonic phased array with uniform emission amplitude. 142
6-9 Amplitude modulation profile of the 8×8 nanophotonic phased array. 143
6-10 8×8 nanophotonic phased array with Gaussian-shaped amplitude modulation. 145
6-11 Active tuning of the 8×8 nanophotonic phased array with Gaussian-shaped amplitude modulation. 146

7-1 Potential application of the SBG-based quarter-wave phase-shift array for the on-chip optical wavelength division multiplexing (WDM) communication. 152
7-2 Proposed active phased array pixels where the phase tuning is realized by the wavelength shifting of an over-coupled resonant structure. 153

CHAPTER 1

Introduction

1.1 Silicon Photonics

Silicon, definitely the most popular element in the periodic table since the invention of the silicon transistors in the 1950s and the complementary metal-oxide-semiconductor (CMOS) technology in the 1960s, has fueled the microelectronic industry for almost half a century. The silicon CMOS technology, being known for its unparalleled ability to make things smaller and smaller, has witnessed the technology scaling from 10μm technology node in the 1970s to the current 22nm node as of 2012, and has enabled the miniaturization of the world's first computer (Electronic Numerical Integrator And Computer, ENIAC) that took up the space of an entire building to the current mobile computing devices that fit into one's palm.

In the similar time frame, photonic technology has revolutionized the communication industry since the first appearance of the laser in the early 1960s and the deployment of the first transatlantic fiber optic cable in the late 1980s. Photon, with its exceptional capability to transmit big data at the speed of light, has lit up fiber optic cables around the globe from the 1990s and has powered the internet boom

ever since.

Silicon photonics, a technological term that combines the two great inventions of the last century, is a prevailing technology that is expected to inherit the unrivaled advantages of both the silicon technology and the photonic technology: to transmit and process big data with light on a small silicon chip enabled by the well-established state-of-the-art silicon CMOS technology. This has been the ultimate goal and a major driving force of silicon photonics since its debut. Silicon photonics benefits from the silicon technology and the photonic technology; and vice versa, silicon photonics is expected to advance these two fields in the near future. On one hand, the optical interconnection powered by silicon photonics is considered an important way, if not the only way, to address the ever-demanding power consumption and bandwidth problems in the current silicon electronics. On the other hand, silicon photonics makes possible the integration of discrete components in the current optical communication system onto a compact silicon chip in a cost-effective way that roots in the very large-scale integration capability of silicon CMOS technology that has been developed for half a century. Therefore, silicon photonics is a technology that benefits from and is expected to push forward both the silicon technology and the photonics technology.

The first decade of this century has seen tremendous progresses in the field of silicon photonics [1] with the successful development of high-performance components that are the key to realize the great mission of silicon photonics: the on-chip optical data communication. Figure 1-1 depicts a typical silicon photonic link for the on-chip optical data communication, including the multi-wavelength laser array to provide different colors of light for the on-chip wavelength division multiplexing (WDM), the optical multiplexer to combine different colors of light and the demultiplexer to separate different colors of light, the optical modulator to convert electrical data to light signal at one place of the chip (*e.g.* the microprocessor) and the optical detector to translate modulated light to electrical data stream at another place (*e.g.* the memory), as well as the silicon waveguides that connect all of the components.

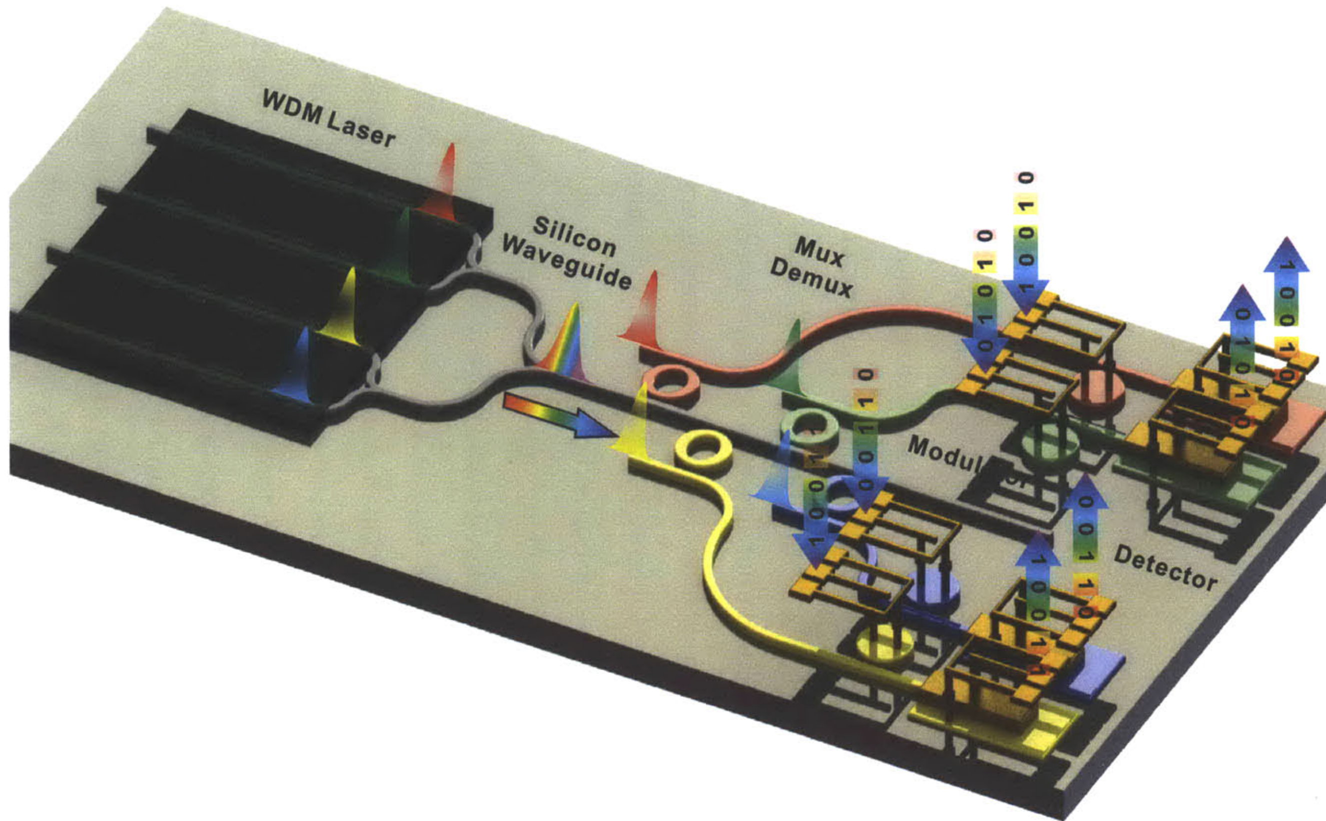

Figure 1-1 A schematic of an on-chip silicon photonic link, composed of the wavelength division multiplexing (WDM) laser array, the optical multiplexer (MUX) and demultiplexer (DEMUX), modulators, detectors, and the silicon waveguides connecting them.

Low-loss silicon waveguide is the backbone of the silicon photonic circuits. Fortunately, silicon is transparent at the conventional optical communication wavelengths around 1.55μm, thanks to the relative large bandgap of silicon ($h\nu$ = 1.11eV, or λ = 1.13μm). Depending on the geometry of the waveguide cross-section, the propagation loss of the silicon waveguide has reached as low as 0.8dB/cm [2] for the stripe waveguide and 0.027dB/cm [3] for the ridge waveguide. Figure 1-2(a) shows a silicon stripe waveguide [4] and Fig. 1-2(b) is a silicon ridge waveguide [3]. The ultra low-loss waveguide makes silicon very suitable for light propagation and processing, and forms the cornerstone of silicon photonics.

Silicon, unlike the III-V materials such as InGaAsP, is a material with indirect bandgap. This indirect bandgap prevents direct light generation from the electron-hole recombination, a process that creates light in semiconductor lasers. To date, a truly silicon laser with light generated directly from silicon by electrical pumping is still a dream, in spite of some demonstrations of silicon lasers based on nonlinear processes [5]. However, various alternative ways to create lasers on silicon chips have already been demonstrated. Figure 1-2(c) shows a hybrid silicon laser where a layer of III-V material is either wafer-bonded or epitaxy-grown on top of the silicon waveguide to provide optical gain when pumped with electrical current, through evanescent coupling of the optical mode from silicon to III-V material [6]. Another approach, the Erbium (Er) doped waveguide laser, is shown in Fig. 1-2(d), in which the optical gain is provided by the Er-doped cladding layer surrounding the silicon-compatible SiN waveguide when optically pumped with a shorter wavelength laser (980nm or 1480nm) [7]. Although the laser is not electrically pumped, this approach has the advantage that it can generate multiple wavelengths from a single input wavelength because of the broad gain bandwidth of Er. By use of a CMOS compatible material Germanium (Ge) to provide optical gain through electrical pumping, the Germanium laser has recently been demonstrated, representing a very promising candidate for silicon photonics light source [8]-[9].

The optical multiplexer (MUX) combines light of different colors, and the demultiplexer (DEMUX) reverses the process. These two devices work together to

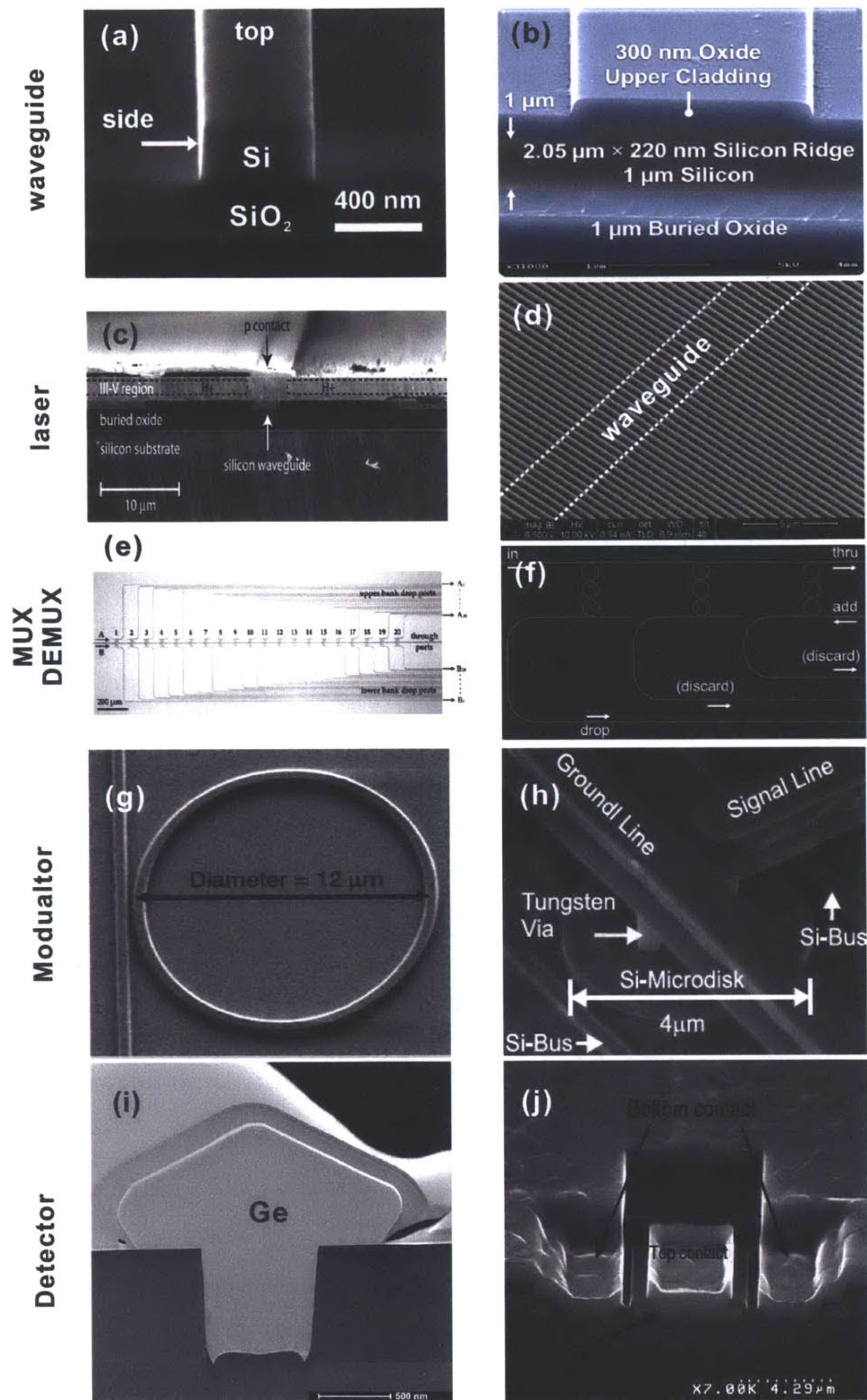

Figure 1-2 A gallery of representative silicon photonic devices demonstrated to date. *Image sources are mentioned in the main text.*

form a WDM system that significantly increases the bandwidth of the data transmitted in a single waveguide. Figure 1-2(e) illustrates a 20-channel second-order microring resonator filter bank that serves as a DEMUX to decompose incoming broadband light into 20 channels evenly spaced in wavelength [10]. Figure 1-2(f) shows a three-stage third-order microring resonator add/drop filer that can be used as a MUX to add new wavelengths into the bus waveguide [11]. In the optical multiplexers and demultiplexers, it is essential to keep an even wavelength spacing between one channel and another. It is usually necessary to add active wavelength tunability to these filters, since the resonant wavelength of these microring filters is extremely sensitive to fabrication deviations and post-fabrication tuning is always required to have all these channels aligned to the wavelength grid of the on-chip WDM system [10].

Silicon photonic modulator converts the electrical data into optical signal. All of the high-speed silicon photonic modulators demonstrated to date exclusively make use of the plasma dispersion effect where the refractive index of silicon is a function of the electron and hole concentration [12]. While the MachZehnder interferometer based silicon photonic modulator is advantageous in its broadband nature, microring resonator based modulator is preferred in that its compact footprint as small as 2μm in radius is suitable for the on-chip WDM networks and modulation speed as high as 25Gb/s has been realized without pre-emphasis [13]. Figure 1-2(g) shows the first silicon photonic microring modulator demonstrated by the Cornell group [14], and Fig. 1-2(h) shows a micro-disk modulator using the vertical p-n junction [15].

Germanium is a CMOS-compatible material that is widely used in silicon photonics as a means to detect optical signals. Electrical current is generated when the energy of a photon is absorbed by Ge to create an electron-hole pair. Figure 1-2(i) [16] and Fig. 1-2(j) [17] shows two examples of integrated high-speed Ge detector on silicon.

To summarize, by use of silicon or silicon compatible materials, all of the devices required to generate, transmit, and process light have already been demonstrated

individually in the silicon photonic platform with high performance and compact size, which holds the promise for the great success of silicon photonics in the future.

1.2 Challenges in Silicon Photonics

As shown in Fig. 1-2, all of the key silicon photonic devices have already been demonstrated with high performance, compact footprint, and compatibility with the state-of-the-art CMOS technology. It seems silicon photonics is ready to take off with a bright future by following the successful path the microelectronic industry has been traveling in the past decades. That is, to integrate thousands of or even millions of these individual components into a small silicon chip to form a functional silicon photonic system with unparalleled performances. However, there are still several essential problems that need to be addressed before this ultimate goal of silicon photonics can be reached.

First, the accuracy of individual silicon photonic devices needs to be greatly improved. Silicon, with a high refractive index of 3.48 at 1.55μm wavelength, tightly confines the optical mode to sub-micron size. This on one hand makes the silicon photonic devices more compact, but on the other hand, it also makes silicon photonic devices extremely vulnerable to fabrication errors. For example, most of the microring based filters and modulators need active tunability to align the resonant wavelength after fabrication [18]. This not only adds complexity to the system, but also greatly increases the power budget of the silicon photonic systems which largely compromises the benefit brought by the silicon photonics technology that is supposed to be power efficient. Therefore, it is necessary to investigate how to accurately fabricate silicon photonic devices.

Second, the great advantage of silicon photonics lies in its potential ability to integrate a large number of otherwise discrete components to form a functional system. Although all of the key components of silicon photonics have already been demonstrated with high performance, the path to large-scale integration of a large number of silicon photonic devices on a chip is still not clear. Without large-

scale integration, all of the great success achieved by previously demonstrated high-performance individual devices will be in vain. It took the microelectronic industry almost two decades from the invention of the first discrete transistor to the deployment of the very-large-scale integrated (VLSI) circuit. How long will it take silicon photonics to reach the stage of large-scale integration? With the aide of the well-established CMOS processing technology, it is expected to take silicon photonics a much shorter time to arrive there. However, due to the extreme sensitivity of silicon photonic devices to fabrication fluctuations, it is definitely not trivial to have a large number of extremely sensitive devices work together as a system. Consequently it is essential to study from a system level how the integrated silicon photonic system performs when a large number of components are included.

To this end, this thesis investigated the two major challenges of silicon photonics through several examples. Part I discussed two different ways to achieve more accurate silicon photonic devices, including Chapter 2 where the accuracy of silicon photonic microring resonator filters is improved by an optimized fabrication technique, and Chapter 3 where the silicon photonic filter is made more accurate with an advanced photonic design based on the sampled Bragg grating. Part II investigated a large-scale silicon nanophotonic phased array as an example of large-scale silicon photonic integration, including the general theory of phased array given by Chapter 4, followed by demonstrations of large-scale passive phased array and active phased array presented in Chapter 5 and Chapter 6 respectively. Although the silicon nanophotonic phased array is not conventionally considered as a typical silicon photonic system for on-chip data communication, the successful demonstration of more than 4,000 components integrated in a silicon chip indeed validates the incredible integration capability of silicon photonics that has never been explored elsewhere before. Moreover, this nanophotonic phased array demonstration extends the functionality of silicon photonics well beyond its traditional communication application to new areas such as laser detection and ranging (LADAR), holographic display, biomedical sensing, *etc.*, which in turn greatly adds

to the motivations of silicon photonics.

PART I

Toward Accurate Silicon Photonic Devices

Chapter 2	**Accurate Device by Improved Nanofabrication**	**27**
Chapter 3	**Accurate Device by Advanced Design**	**43**

The demanding accuracy requirement of silicon photonic devices is always challenging. In Part I, two different ways to achieve a more accurate silicon photonic device are presented. The most direct and efficient way to improve the device accuracy is to improve the precision of the nanofabrication tools and processes, as is discussed in Chapter 2. While advanced fabrication is not always available or economic, an alternative way to improve the device accuracy is to employ novel device designs to accommodate the available fabrication resources, as is shown in Chapter 3.

CHAPTER 2

Accurate Device by Improved Nanofabrication

The most direct and efficient way to achieve silicon photonic devices with high accuracy is to improve the precision of the fabrication tools and hence to reduce the dimensional errors of the resulting devices. In this chapter, we will demonstrate that, by minimizing the intrafield distortion error in the scanning electron-beam lithography (SEBL) system, the fabrication accuracy of silicon photonic devices can be improved and high performance is thus achievable. As an example, we will show that the frequency mismatch in the second-order microring resonators, which is a universal problem in high-order microring resonators, is largely reduced by minimizing the intrafield distortion in an SEBL tool. This chapter will start with an introduction to the frequency mismatch problem in high-order microring resonator filters and the intrafield distortion in SEBL systems, followed by evidences showing the correlation between the frequency mismatch and the intrafield distortion, and finally an experimental demonstration showing that the frequency mismatch can be mitigated by minimizing the intrafield distortion in SEBL.

2.1 Frequency Mismatch and Intrafield Distortion

Microring resonator is an important component in silicon photonics, which finds immediate applications from optical lasers, through electrooptic modulators, to add/drop filters. High-performance microring resonator requires multiple identical microrings to be used, in order to achieve a better filter shape [19]-[20]. Figure 2-1(a) depicts a second-order microring resonator for applications such as the add/drop filter in optical routing, where the waveguide-to-ring and ring-to-ring coupling coefficients can be engineered to realize various filter responses, such as maximally flat and Chebyshev filters [21]. The microrings are normally designed to be identical to each other in terms of geometry and resonant frequency. However, the small device size and high refractive index contrast present a number of fabrication challenges, as the optical properties of such filters is extremely sensitive to nanoscale dimensional deviations [22]. One of the crucial issues in high-order microring filters is the resonant-frequency mismatch between the microrings, which markedly reduces the filter performance [23]-[27]. As shown in Fig. 2-1(b), in a second-order microring filter originally designed to achieve maximally flat response, the flatness and symmetry of the through-port response, the in-band extinction, as well as the filter roll-off are largely degraded due to the mismatch of resonant frequencies of the two microrings. This frequency mismatch problem constantly appears in high-order microring resonators. It is necessary to study the origin of this frequency mismatch in order to solve this problem and hence to improve the performance of high-order microring resonators. Since the photonic structures surrounding the two microrings are symmetric, proximity effect in lithography is not responsible for the relative frequency mismatch. Also the two microrings are too close to each other to have noticeable thickness difference between them. Here we will show this frequency mismatch is mainly caused by the intrafield distortion problem in the SEBL.

SEBL is widely used in making microelectronic as well as photonic devices, either by direct SEBL writing or by optical lithography in which the optical mask

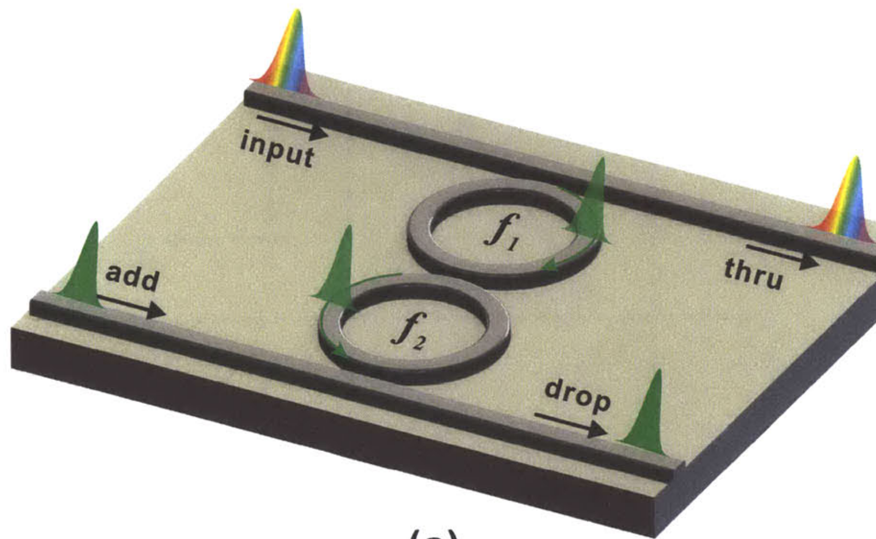

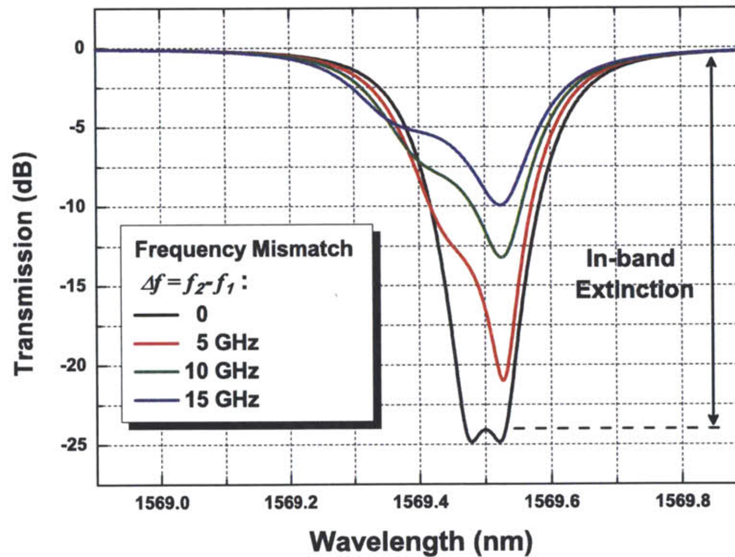

Figure 2-1 (a) A schematic of the second-order microring-resonator filter. $f_{1,2}$ represents the resonant frequencies of the two microrings. (b) The impact of frequency mismatch on the through-port response of the second-order microring resonators (simulation). The frequency mismatch is given by $\Delta f = f_2 - f_1$.

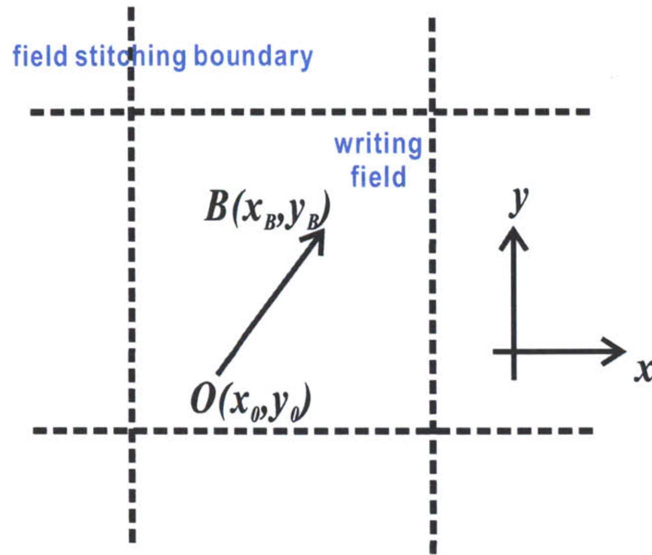

Figure 2-2 Illustration of the intrafield distortion problem in SEBL. The electron beam that is designed to expose the point **O**:(x_0, y_0) is actually deflected to the point **B**:(x_B, y_B) because of imperfections in the SEBL system. The intrafield distortion is denoted by the vector $\overrightarrow{OB}$.

is also made from SEBL. In SEBL, the electron beam is deflected by magnetic lenses within the writing field which is normally around 100μm square. The fields are then stitched together to form a larger area by precisely moving the laser-interferometer-controlled stage on which the substrate is mounted. To avoid severe field-stitching errors, microring resonators are usually written in a single writing field. Intrafield distortion is due to systematic beam-deflection error within a single field, caused by electron-optics imperfection and digital-analog converter error. It exists in every SEBL system. Figure 2-2 illustrates the problem. The beam is supposed to expose point **O**:(x_0, y_0) but the actual beam position is at point **B**:(x_B, y_B). The displacement vector

$$\overrightarrow{OB} = \hat{x}\Delta x + \hat{y}\Delta y = \hat{x}(x_B - x_0) + \hat{y}(y_B - y_0) \tag{2.1}$$

is called intrafield distortion at position **O**:(x_0, y_0), where Δx and Δy represent intrafield distortion in x- and y-direction, respectively. Intrafield distortion is

position-dependent, that is, Δx and Δy are functions of the designed beam position **O**:(x_0, y_0) [28]. Intrafield distortion can be measured by use of a nanoscale metrology method [29]. Figure 2-3(a) shows the principle of intrafield-distortion measurement. A metal grid with a fine pitch, generated on a silicon substrate by interference lithography, was utilized as a metrological reference. One-dimensional grating and two-dimensional grid created by interference lithography have excellent long-range spatial coherence, and hence can be served as precise rulers in nanoscale. The grid was then scanned by the SEBL system in x- and y-direction, and the secondary-electron signals collected by the detector. The corresponding intrafield distortion, Δx and Δy, at various positions in the writing field was then determined by comparing the phase of the collected signal to that of an ideal grid signal. The blue line in Fig. 2-3(b) illustrates the ideal secondary electron signal when the grid is scanned in the x- or y-direction, while the red line shows the actual signal where a phase difference $\Delta\varphi$ is seen because of the intrafield distortion. The intrafield distortion in the x- or y-direction at this point is then given by

$$\Delta_{x,y} = 2\pi \cdot \frac{\Delta\varphi}{p} \tag{2.2}$$

where p is the period of the grid, and $\Delta\varphi$ can be accurately measured by taking the Fourier transform of the spatial signal shown in Fig. 2-3(b).

Figure 2-4 shows the measured intrafield distortion in a 100μm×100μm writing field in a Raith 150 SEBL system at MIT. Each point in the field has an associated Δx and Δy. From Fig. 2-4(a), it is seen that the maximum distortion in x-direction occurs at the right edge of the writing field. This is attributed to the fly-back of the beam on this edge. Similarly, the maximum distortion in y-direction appears at the lower edge of the writing field. The maximum total intrafield distortion is around 20nm, which occurs at the lower-right corner of the writing field.

Based on the measurement of intrafield distortion shown in Fig. 2-4, the actual beam position (x_B, y_B) can be approximated by a polynomial function of the

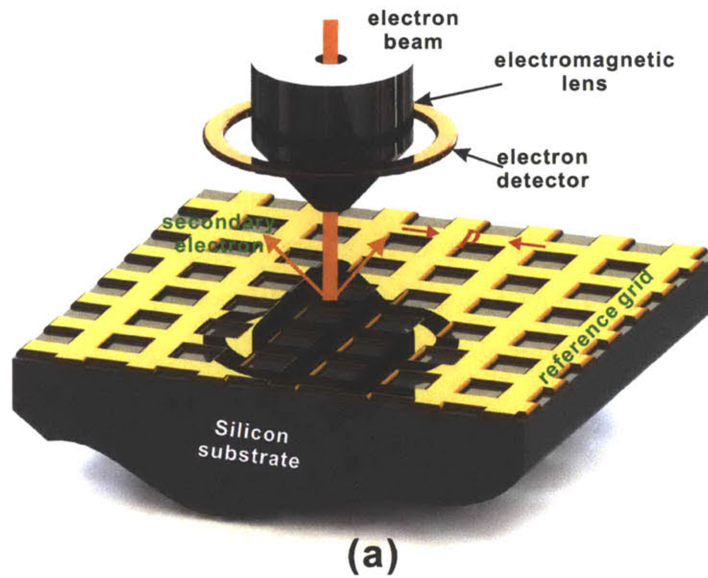

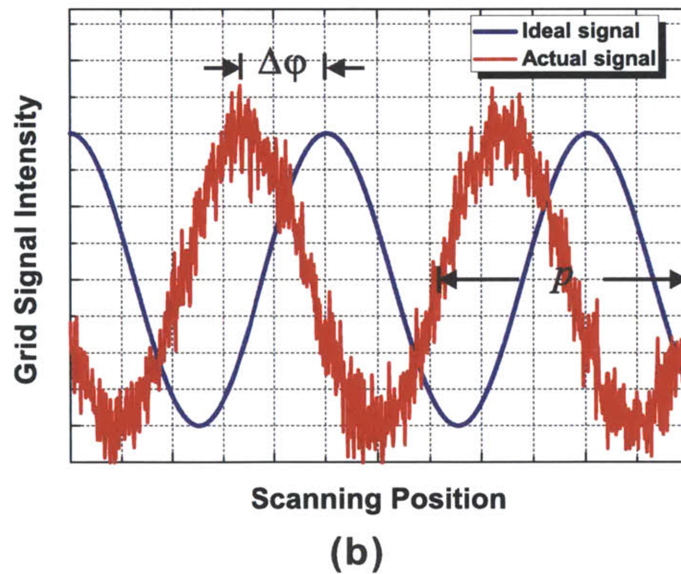

Figure 2-3 (a) Measurement setup of the intrafield distortion in the SEBL system, where a metal grid made from the interference lithography is used as a precise ruler in the nanoscale. (b) The intrafield distortion is determined by the phase difference between the ideal signal (blue) and the actual signal (red) when scanning the grid with the electron beam in x- or y-direction.

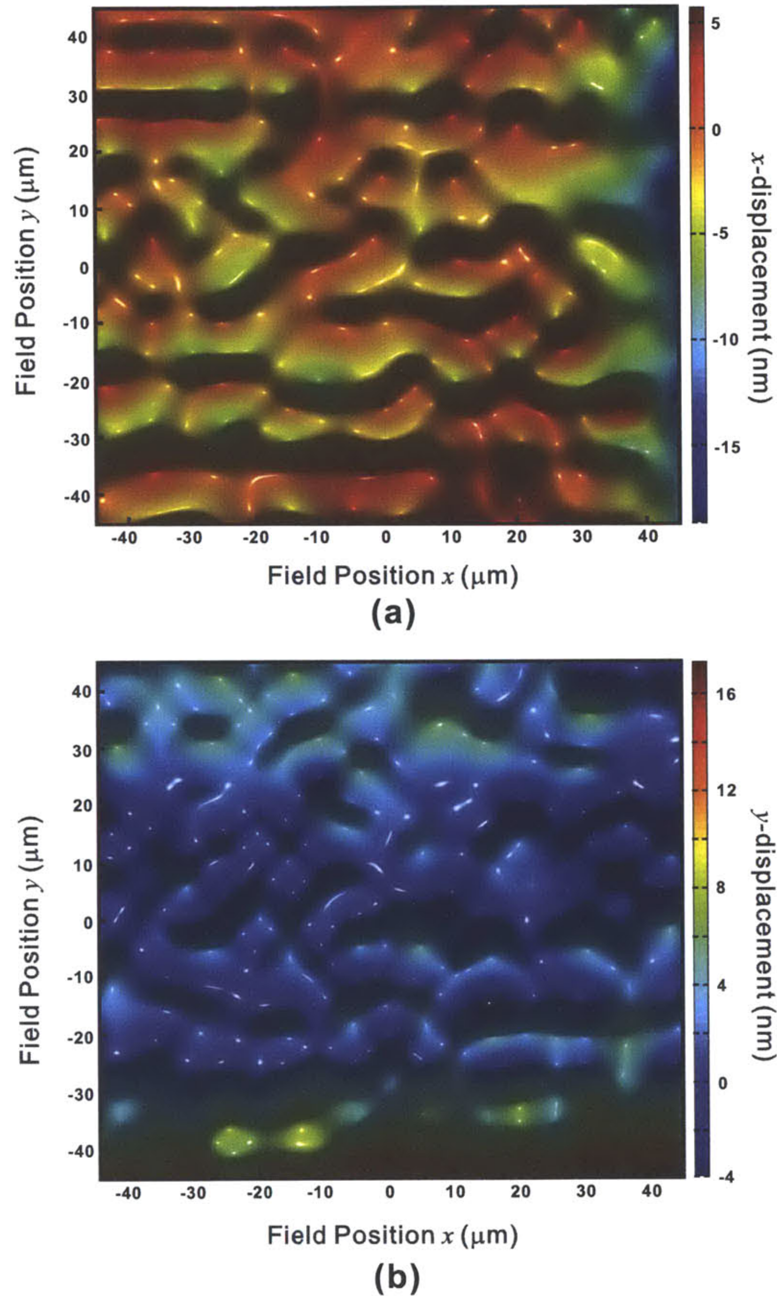

Figure 2-4 Measured intrafield distortion in (a) x- and (b) y-direction in a 100μm×100μm writing field of a Raith 150 SEBL system at MIT. The two dimensional quasi-periodic character of the distortion (i.e. the quasi-periodic peaks and valleys in the above distortion maps) is probably an indicator of digital-analog converter imperfection of the system.

designed beam position (x_0, y_0) as

$$\begin{cases} x_B = f(x_0, y_0) = x_0 + \Delta x = a_0 + a_1 x_0 + a_2 y_0 + a_3 x_0^2 + a_4 x_0 y_0 + a_5 y_0^2 \\ y_B = g(x_0, y_0) = y_0 + \Delta y = b_0 + b_1 x_0 + b_2 y_0 + b_3 x_0^2 + b_4 x_0 y_0 + b_5 y_0^2 \end{cases} \quad (2.3)$$

where the coefficients a_n and b_n can be extracted by numerically fitting Equation 2.3 to the distortion maps of Fig. 2-4(a) and (b). In this work, the polynomial in Equation 2.3 is approximated to the 4th order.

In the fabrication of microring filters using SEBL, the geometric parameters of the microrings, such as the radius and width, usually deviate from designed values due to this intrafield distortion. The resonant frequency, which is very sensitive to dimensional variations, is accordingly changed. For instance, 1nm dimensional variation in radius and width will result in tens of GHz frequency shift, depending on the design and material of the microrings. In high-order microring filters, as the rings are located at different positions of the writing field, each microring experiences a different frequency shift because of the position-dependent nature of intrafield distortion. Therefore, frequency mismatch between the microrings occurs. And the amount of this frequency mismatch varies with the position of the filter in the writing field.

2.2 Intrafield Distortion Induced Frequency Mismatch

In this section, we will experimentally demonstrate the frequency mismatch problem in high-order microring resonators is mainly caused by the intrafield distortion in the SEBL system [30].

Second-order microring resonator filters are used in the experiment for the ease of fabrication and analysis. The cross section of the waveguides used in this experiment is shown in Fig. 2-5(a). A core layer of 400nm silicon-rich silicon nitride (SiN, refractive index $n = 2.18$) on a 3μm SiO_2 cladding is used for the bus waveguides and the microrings, with air top and side cladding. The SiN layer is deposited by

Low-Pressure-Chemical-Vapor-Deposition (LPCVD), providing a uniform thickness across the wafer. The widths of bus and ring waveguides are 700nm and 900nm, respectively. The ring radius is 8μm. The bus-to-ring and ring-to-ring gaps are 120nm and 380nm, respectively. Finite-Difference simulation shows that, in this design, 1nm deviation in the radius and width of the microring will cause -18.4GHz and -33GHz resonant-frequency shift of the microring, respectively.

The fabrication process of the microring resonators is described as follows [24]. A silicon wafer is first thermally oxidized to form a 3μm thick SiO_2 as the undercladding to prevent light leaking into the silicon substrate. A layer of 400nm low-stress SiN is then deposited by LPCVD in a vertical thermal reactor with a gas mixture of SiH_2Cl_2 and NH_3. Then 200nm poly-methyl-methacrylate (PMMA) is spun on as the e-beam resist, followed by another spin of 60nm Aquasave which is a water-soluble conductive polymer to prevent surface charging of the resist during e-beam writing. The PMMA is exposed to define the patterns with the Raith 150 SEBL system whose intrafield distortion is previously measured as shown in Fig. 2-5. Then the Aquasave is removed in water, followed by resist development to remove areas that are scanned by e-beam since PMMA is a positive e-beam resist. Next, 45nm Nickel (Ni) is evaporated on the wafer, followed by a liftoff to remove the unexposed PMMA. With the Ni as a hard mask, the waveguides are dry etched in a gas mixture of CHF_3 and O_2. Finally, the Ni hard mask is removed in a commercial wet Ni etchant. Scanning-electron micrographs (SEMs) of the fabricated second-order filter are shown in Fig. 2-5(b).

Second-order filters written at 10 different positions relative to the writing field are fabricated, and the frequency mismatch obtained from the through- and drop-port spectra. For each position, six filters were fabricated in six different physical writing fields (but at the same position relative to each writing field) to get the averaged frequency mismatch at that particular position. Each of these filters took up a single writing field. The red dots in Fig. 2-6(a) and (b) are the measured average frequency mismatch when the filters are centered at $(x, 0)$ and $(0, y)$ in the writing field, respectively. The error bars indicate the frequency mismatch

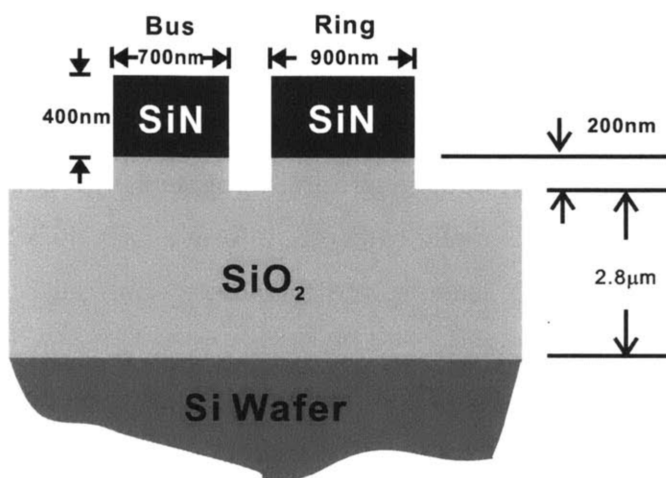

(a)

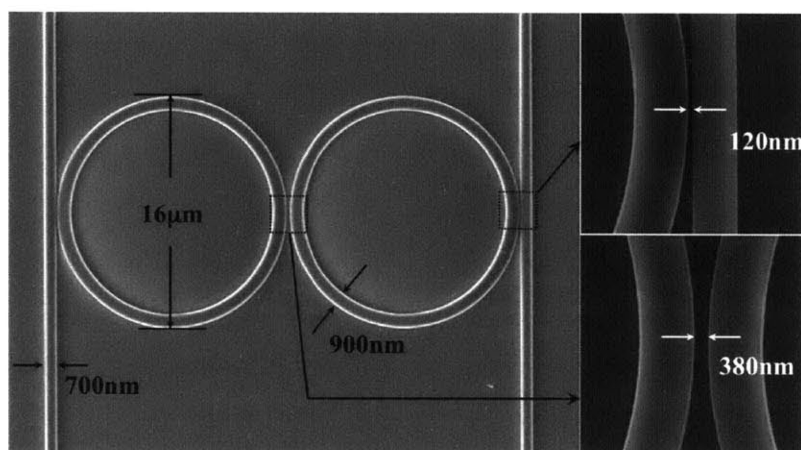

(b)

Figure 2-5 (a) Diagram of waveguides cross-section. (b) Scanning-electron micrograph of the fabricated second-order microring filter, and details in bus-ring and ring-ring coupling regions.

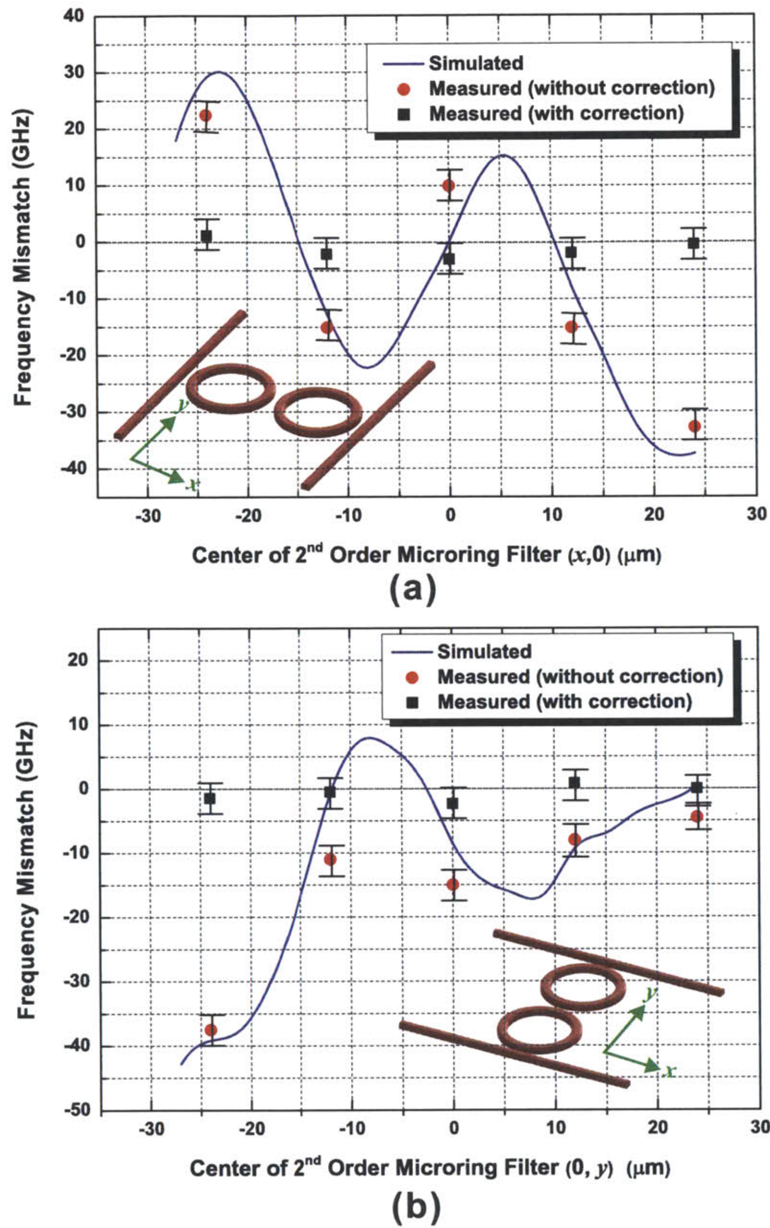

Figure 2-6 Frequency mismatch between the two rings of second-order microring filters at various positions in the SEBL writing field: (a) the positions of the center of the second-order filter are at $y = 0$ and various values of x, from $x = -24\mu\text{m}$ to $x = +24\mu\text{m}$, and (b) the positions of the center of the second-order filter are at $x = 0$ and various values of y from $y = -24\mu\text{m}$ to $y = +24\mu\text{m}$. The inset diagrams illustrate the orientations of the filters in the two cases. The continuous lines are the simulation results. The red dots are measured frequency mismatch without intrafield-distortion correction, and the black squares are with correction.

fluctuation caused by some random factors in fabrication. Based on Equation 2.3, geometric deviations of the microrings and the corresponding frequency mismatch caused by intrafield distortion can also be simulated at various positions of the writing field. The simulation results are shown in Fig. 2-6 as continuous curves. It is seen that the simulation agrees well with the experiment, which demonstrates that the intrafield distortion in SEBL is the major cause of frequency mismatch in high-order microring filters.

2.3 Intrafield Distortion Correction

SEBL is the most widely used lithography tool in fabrication of silicon photonic devices because of its high resolution; however, as discussed above, intrafield distortion in SEBL compromises the performance of these devices. In this work, we propose a simple method to correct the intrafield distortion in SEBL. As mentioned above, the designed beam position (x_0, y_0) and actual beam position (x_B, y_B) are related by the polynomial function $f(x, y)$ and $g(x, y)$ as described by Eq. 2.3. Thus, by pre-distorting the designed beam position to a modified position (x_1, y_1) in the layout, where (x_1, y_1) satisfies

$$x_0 = f(x_1, y_1) \ , \ y_0 = g(x_1, y_1) \tag{2.4}$$

then the actual beam position will return to the desired position (x_0, y_0). Hence, the intrafield distortion can be corrected.

Using this correction method, second-order filters at various positions in the writing field are fabricated. The black squares in Fig. 2-6 are the measured frequency mismatch after correction. The frequency mismatch is around 0, which validates the correction method. Figure 2-7 shows a typical result of the filter responses with and without intrafield-distortion correction. In this particular filter, frequency mismatch is reduced from -11.5GHz to -1.2GHz. Figure 2-8(a) and (b) illustrate the statistical distribution of the measured frequency mismatch of a num-

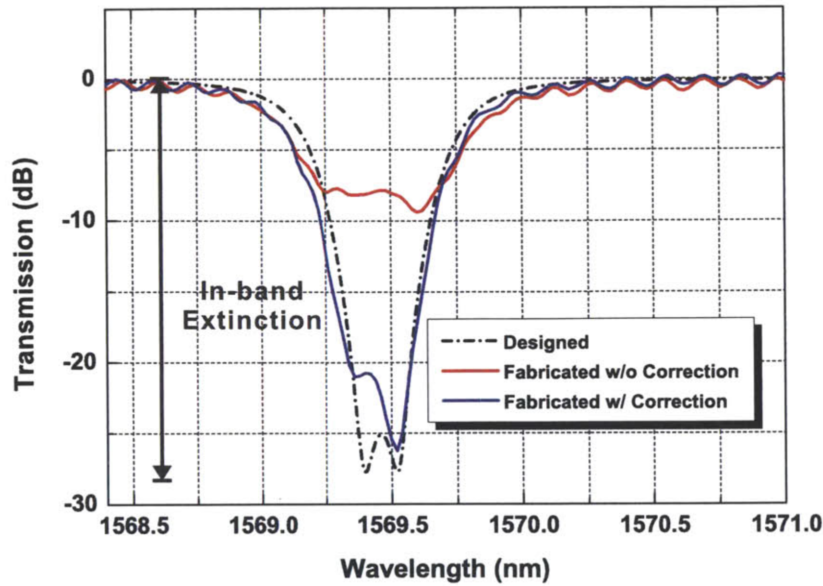

Figure 2-7 The filter spectra of a second-order microring resonator with and without intrafield distortion correction. The filter shape is largely improved by applying the intrafield distortion correction.

ber of filters, without and with intrafield-distortion correction, respectively. The multi-peak distribution in Fig. 2-8(a) indicates the position-dependent nature of the frequency mismatch. The distributions are fitted by a normal distribution, where μ represents the average frequency mismatch while the standard deviation σ corresponds to the fluctuation of frequency mismatch introduced by random fabrication errors other than the intrafield distortion. It can be seen that the average frequency mismatch is reduced from -8.6GHz to 0.28GHz by applying the correction method. Standard deviations σ in Fig. 2-8(a) and (b) are close, which is reasonable because σ depends on uncontrolled random variations in fabrication process. It should be possible to further reduce σ by optimizing the fabrication process.

In this chapter, we have shown an example where more accurate silicon photonic devices can be achieved by an improved nanofabrication technique. In particular, we experimentally demonstrated that the frequency mismatch in high-order microring resonator filters is caused primarily by intrafield distortion in SEBL. The intrafield distortion map of an SEBL system was measured. The frequency mis-

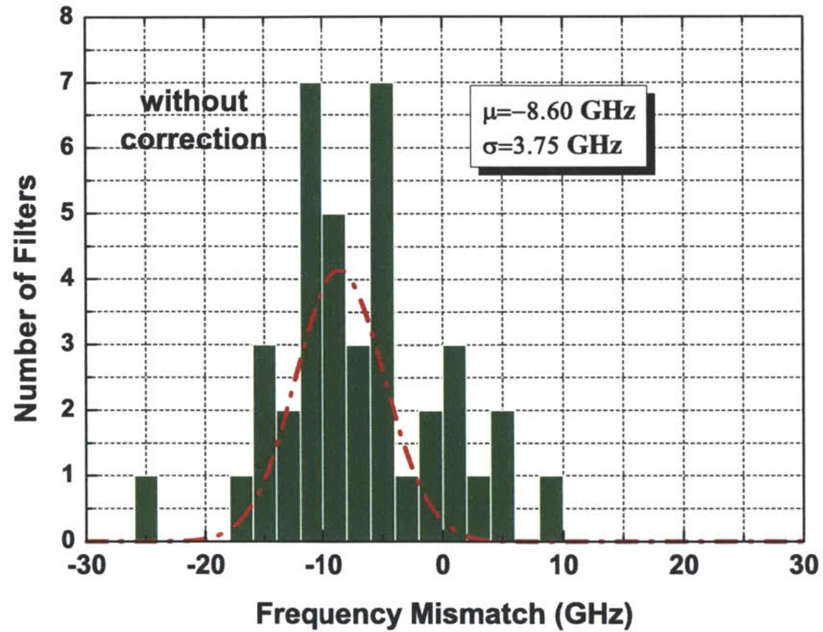

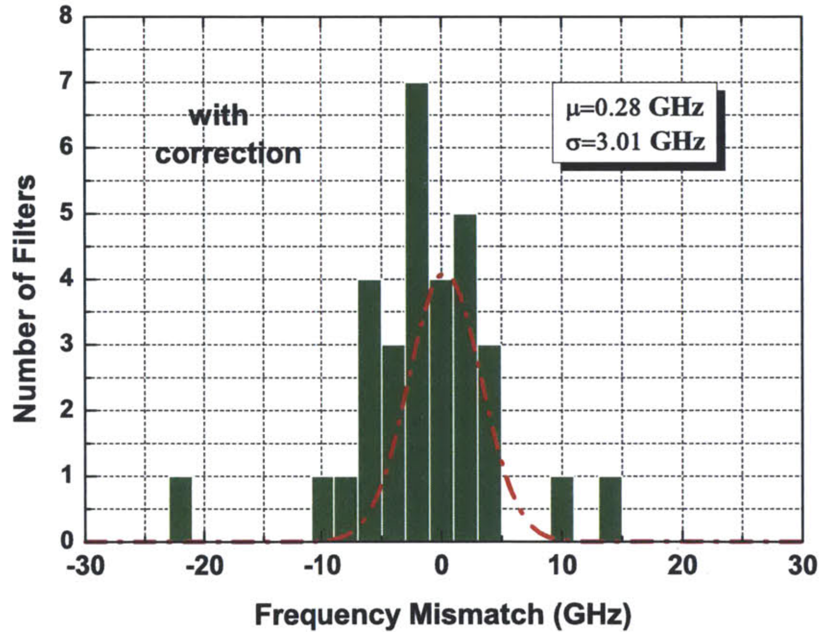

Figure 2-8 Statistics of frequency mismatch of a number of second-order filters at several positions in the SEBL writing field, where μ is the average frequency mismatch, and σ is the standard deviation of frequency mismatch: (a) without distortion correction and (b) with distortion correction. Note that the correction results in a reduction of μ from -8.6GHz to 0.28GHz.

match of second-order microring filters centered at various positions in the SEBL writing field was simulated based on the distortion map, which is consistent with experimental results. A simple method was also proposed to correct the intrafield distortion. By use of this correction method, the average frequency mismatch in second-order microring filters was reduced from -8.6GHz to 0.28GHz.

CHAPTER 3

Accurate Device by Advanced Design

In Chapter 2, we have shown accurate silicon photonic devices can be achieved by improved fabrication techniques with more precision. The improvement of fabrication tools and techniques is absolutely the most important way to improve the device performance, which has been witnessed by the advancement of electronic industry for half a century from the initial 10μm to the current 22nm technology node. However, when the high-precision fabrication is not readily available or is not economic, it is important to incorporate advanced device designs to accommodate the available fabrication techniques. In Chapter 2, we have also seen that holographic gratings patterned by interference lithography has the best accuracy that could even serve as a ruler to measure the nano-scale deviations in the scanning-electron-beam lithography (SEBL) system. It is therefore obvious that grating-based photonic devices can easily achieve the best accuracy. As a matter of fact, grating structures are indeed widely used in photonics such as in the semiconductor lasers as a feedback cavity. However, grating structure fabricated with interference lithography is rarely used in silicon photonics. One important reason is that gratings made by interference lithography are not flexible. Grating has a

simple filter shape with limited applications, whereas other popular silicon photonic structures such as microring resonators can produce various filter shapes that are suitable for a broad range of applications. Provided that complex filter shapes can be achieved in the grating-based structures, a wider range of silicon photonic applications can be expected in grating to taking advantage of its high accuracy originating from the interference lithography. In this chapter, we will introduce a novel silicon photonic grating structure, namely the sampled Bragg grating (SBG), in which various filter shapes can be realized based on the precise gratings made from interference lithography. This chapter will start with a brief introduction to Bragg gratings, followed by the theory and design methods of the SBG in order to achieve complex filter shapes, and finally an experimental demonstration of a silicon photonic SBG with a quarter-wave phase shift.

3.1 Basics of Bragg Gratings

Figure 3-1 depicts the basic structure of a grating, namely the uniform grating, where rectangular grooves with a period of Λ are etched into the surface of an optical waveguide. Gratings are widely used as diffractive elements in optics for centuries. The Bragg grating, the type of grating that we will focus on in this work, can be considered as a diffraction grating which diffracts the forward-travelling wave into backward-traveling wave. According to the diffraction equation, in order to have the diffracted beam in the opposite direction against the input beam, the period of the grating should satisfy the following Bragg condition

$$\Lambda = \frac{\lambda_0}{2n_{\text{eff}}} \tag{3.1}$$

where λ_0 is the free-space wavelength of the light, and n_{eff} is the effective index of the waveguide where light propagates. According to the perturbation theory, the waveguide with corrugated grating on top can be considered as a two-layer waveguide where the etched grating is replaced by a uniform artificial material

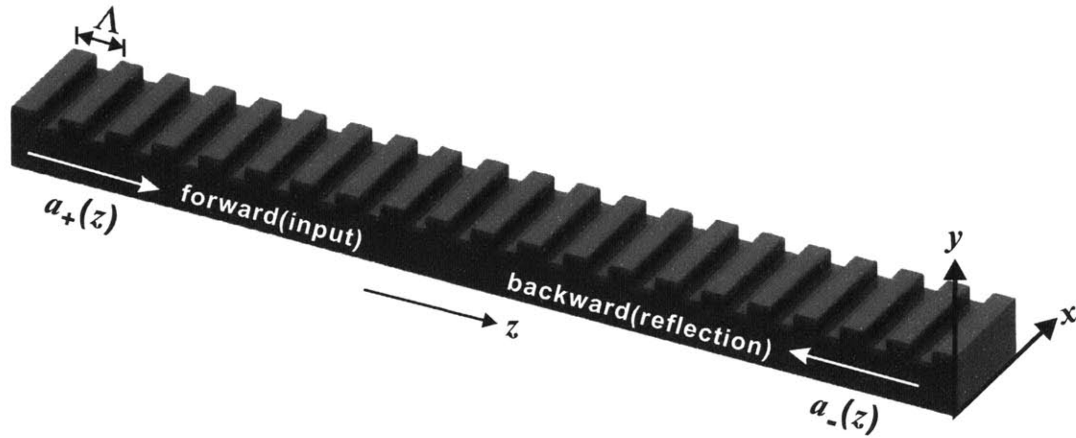

Figure 3-1 Schematic of a uniform grating on a stripe waveguide.

with refractive index n_g, plus a perturbation layer with alternating high-low refractive indices $\pm\Delta n_0$ characterized by a position dependent refractive index $\Delta n(z)$, as shown by Fig. 3-2 [31]. The refractive index of the artificial layer in Fig. 3-2(b) is given by

$$n_g^2 = (1 - D) \cdot n_0^2 + D \cdot n_1^2 \tag{3.2}$$

where n_1 and n_0 are the refractive index of the core material and the cladding material respectively, and D is the duty cycle of the grating. The effective index n_{eff} of the grating used in Equation 3.1 can be calculated from a 2-D mode solver based on this z-invariant waveguide shown in Fig.3-2(b). The Bragg grating can be mathematically described by its perturbation to the electromagnetic mode, *i.e.* the refractive index modulation $\Delta n(z)$

$$\Delta n(z) = \frac{1}{2}\Delta n_0 \cdot \exp\left(j\frac{2\pi z}{\Lambda}\right) + c.c. \tag{3.3}$$

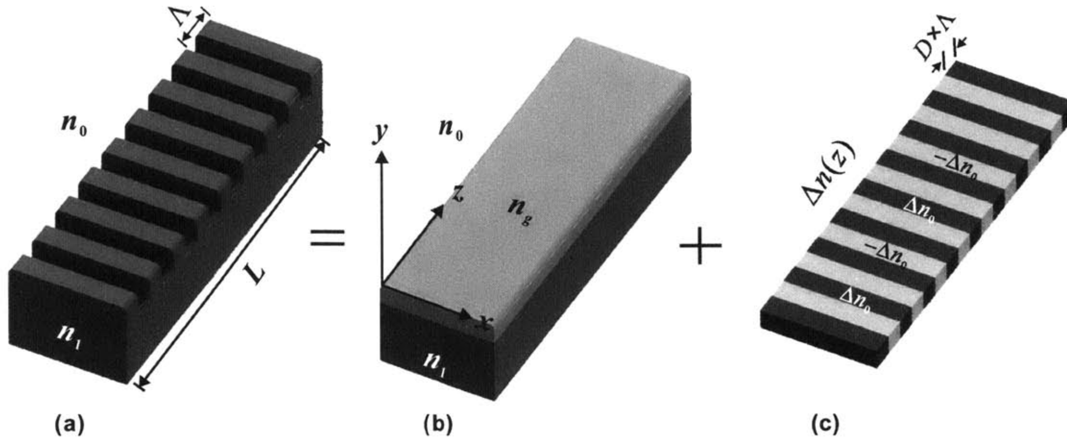

Figure 3-2 (a) The Bragg grating corrugation can be modeled as (b) a z-invariant waveguide with an artificial layer whose refractive index is n_g to replace the corrugated grating, plus a perturbational z-variant function $\Delta n(z)$ with alternating high-low refractive indices $\pm\Delta n_0$.

where $c.c.$ stands for the complex conjugate of the first part of the equation. Δn_0 gives the strength of the grating perturbation which depends on both the refractive index contrast and the geometry of the grating. Δn_0 is a constant for uniform Bragg grating but can be variant in z-direction in complex Bragg gratings such as apodized Bragg grating and chirped Bragg grating. Note that although the grating perturbation has a rectangular shape, it is described by a sinusoidal function here for convenience. This is an adequate approximation since the periodic rectangles can be decomposed into many sinusoidal components and the first order weights the most. For the uniform Bragg grating with a length L, its reflection coefficient at a specific wavelength λ can be analytically derived

$$r(\lambda) = \frac{\frac{\kappa}{\gamma}\sinh(j\gamma L)}{\cosh(j\gamma L) + \frac{\sigma}{\gamma}\sinh(j\gamma L)} \tag{3.4}$$

where

$$\begin{aligned}\sigma &= \frac{2n_{\text{eff}}\pi}{\lambda} - \frac{\pi}{\Lambda} \\ \gamma^2 &= \sigma^2 - |\kappa|^2\end{aligned} \tag{3.5}$$

κ is the coupling coefficient between the forward-propagating mode and the backward-propagation mode, and can be solved from the coupled mode theory as [32]

$$\kappa = \frac{k^2}{2\pi k_z}(n_1^2 - n_0^2)\sin(\pi D)\cdot\Gamma \tag{3.6}$$

where k is the free space wave vector, and k_z is the propagation constant of light in the waveguide shown in Fig. 3-2(b). Γ is a factor that describes the extent to which the electromagnetic wave overlaps with the grating

$$\Gamma = \frac{\displaystyle\iint_{n(x,y)=n_g} E(x,y)\,dxdy}{\displaystyle\iint E(x,y)\,dxdy} \tag{3.7}$$

The coupling coefficient κ is also related to the grating strength parameter Δn_0 used in Equation 3.3 by

$$\kappa = \frac{\pi}{2n_{\text{eff}}\Lambda}\Delta n_0 \tag{3.8}$$

Most frequently the gratings are represented by its transfer matrix $T(\lambda)$

$$T(\lambda) = \begin{bmatrix}\cosh(\gamma L) - j\frac{\sigma}{\gamma}\sinh(\gamma L) & -\frac{\kappa^*}{\gamma}\sinh(\gamma L) \\ \frac{\kappa}{\gamma}\sinh(\gamma L) & \cosh(\gamma L) + j\frac{\sigma}{\gamma}\sinh(\gamma L)\end{bmatrix} \tag{3.9}$$

and

$$\begin{bmatrix} a_+(L) \\ a_-(L) \end{bmatrix} = \begin{bmatrix} \cosh(\gamma L) - j\frac{\sigma}{\gamma}\sinh(\gamma L) & -\frac{\kappa^*}{\gamma}\sinh(\gamma L) \\ \frac{\kappa}{\gamma}\sinh(\gamma L) & \cosh(\gamma L) + j\frac{\sigma}{\gamma}\sinh(\gamma L) \end{bmatrix} \cdot \begin{bmatrix} a_+(0) \\ a_-(0) \end{bmatrix} \tag{3.10}$$

where $a_+(z)$ and $a_-(z)$ are the forward and backward wave component along the grating respectively. In gratings where the coupling coefficient $\kappa(z)$ varies along z-direction, such as the apodized grating and the chirped grating, the grating can be divided into many small segments and each segment can be treated as a uniform grating with a constant κ. Then the transfer matrix of the whole grating can be obtained through the multiplication of the transfer matrices of all of the uniform segments. The reflection and transmission coefficients are then given by

$$r(\lambda) = \frac{a_-(0)}{a_+(0)} \quad , \quad t(\lambda) = \frac{a_+(L)}{a_+(0)} \tag{3.11}$$

The reflection coefficient r can be analytically derived from the coupled mode theory for a grating with z-variant coupling coefficient $\kappa(z)$ [33]

$$\frac{d}{dz}r = j\kappa^* r^2 + 2j\sigma r + j\kappa(z) \tag{3.12}$$

Equation 3.12 has no explicit solution. However, in weak gratings where $r \ll 1$ and hence $r^2 \approx 0$, Equation 3.12 can be solved as a first order differential equation which gives

$$r(\sigma) = -\int_{-\infty}^{\infty} j\kappa(z)e^{-j2\sigma z}\,dz \tag{3.13}$$

Equation 3.13 reveals that the reflection coefficient r and the coupling coefficient

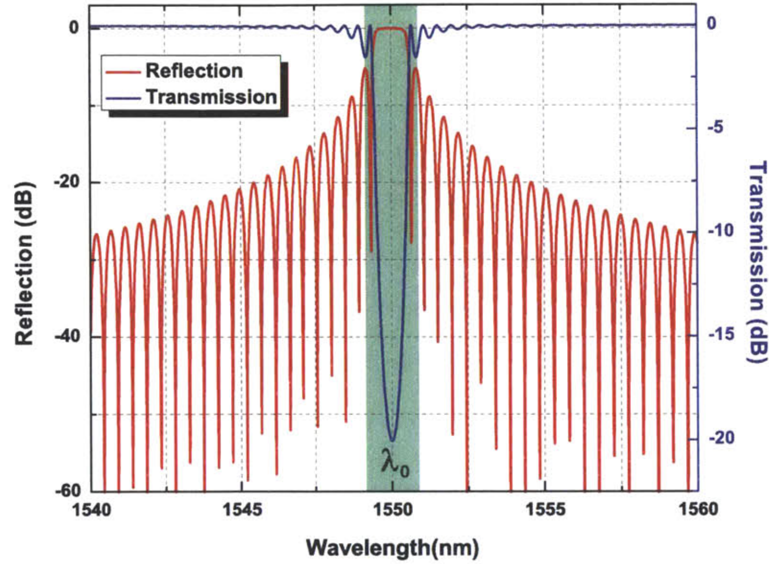

Figure 3-3 Simulated transmission and reflection spectra of a typical uniform Bragg grating. A band gap is seen as highlighted by the green color, centered at wavelength λ_0 which is related to the grating period by the Bragg condition in Equation 3.1.

$\kappa(z)$ in Bragg gratings are a Fourier transform pair

$$r(\frac{\sigma}{2}) = -j\mathscr{F}\left(\kappa\left(z\right)\right) \tag{3.14}$$

where the symbol $\mathscr{F}$ stands for the Fourier transform. The Fourier transform relation shown in Equation 3.14 will serve as a powerful tool for the filter synthesis of Bragg gratings, and will be extensively used in the rest of this chapter. Although this Fourier transform relation is derived for weak gratings, it also provides valuable intuitions for the synthesis and analysis of strong Bragg gratings.

Figure 3-3 simulates the transmission and reflection spectra of a typical uniform Bragg grating. It is seen that a photonic band gap is created by the periodic perturbation, centered at wavelength λ_0 that is related to the grating period Λ by the Bragg condition $\lambda_0 = 2n_{\text{eff}}\Lambda$.

3.2 Sampled Bragg Grating

3.2.1 Ordinary Sampled Bragg Grating

Figure 3-4 shows a schematic of an ordinary sampled Bragg grating (SBG), where a uniform grating is modulated, or sampled, by an on-off envelope function $S(z)$. Note that a ridge waveguide is used here instead of the stripe waveguide shown in Section 3.1 for the ease of fabrication. Because ridge waveguide can operate at single mode with a relatively large cross section which largely facilitates the lithography.

Similar to Equation 3.3, the SBG can be mathematically described by its refractive index modulation

$$\Delta n(z) = \frac{1}{2}\Delta n_0 \exp\left(j\frac{2\pi z}{\Lambda}\right) \cdot S(z) + c.c. \tag{3.15}$$

where $S(z)$ is normally a periodic function that can be decomposed into Fourier series

$$S(z) = \sum_{m=-\infty}^{\infty} \frac{\sin\frac{m\pi}{2}}{m\pi} \exp\left(j\frac{2m\pi}{P}z\right) \tag{3.16}$$

where P ($P \gg \Lambda$) is the period of the sampling function $S(z)$. The duty cycle of $S(z)$ is assumed to be 0.5 in Equation 3.16 as usually used in SBGs. Substituting Equation 3.16 into Equation 3.15 yields

$$\Delta n(z) = \frac{1}{2}\Delta n_0 \cdot \sum_{m=-\infty}^{\infty} \frac{\sin\frac{m\pi}{2}}{m\pi} \exp\left(j2\pi\left(\frac{1}{\Lambda} + \frac{m}{P}\right)z\right) + c.c. \tag{3.17}$$

It is seen from Equation 3.17 that an SBG can be seen as a combination of a series of weighted uniform Bragg gratings, each of which has an equivalent grating period

Λ_m given by

$$\Lambda_m = \frac{\Lambda P}{P + m\Lambda} \approx \Lambda - \frac{m\Lambda^2}{P} \tag{3.18}$$

where the assumption $\Lambda \ll P$ is taken into account in the approximation. Each uniform grating will generate a photonic band gap in the grating spectrum centered at the corresponding Bragg wavelength

$$\lambda_m = 2n_{\text{eff}}\Lambda_m = \lambda_0 - m \cdot \frac{\lambda_0^2}{2n_{\text{eff}}P} \tag{3.19}$$

Therefore, it can be envisioned that the spectrum of the SBG is composed of many photonic band gaps, or channels, which appear as valleys in the transmission spectrum and peaks in the reflection spectrum. The channel spacing $\Delta\lambda_c$ is given by

$$\Delta\lambda_c = \frac{\lambda_0^2}{2n_{\text{eff}}P} \tag{3.20}$$

where $\lambda_0 = 2n_{\text{eff}}\Lambda$ which is the original Bragg wavelength of the uniform grating and also the center wavelength of the 0th-order ($m = 0$) channel of the SBG. It is also noticed that each channel has a weighting factor F_m given by

$$F_m = \frac{\sin\frac{m\pi}{2}}{m\pi} \tag{3.21}$$

which is 2 for the 0th-order and 1 for the $\pm 1^{\text{st}}$-oder ($m = \pm 1$) channels. As a result, the 0th-order channel has the strongest grating strength while the $\pm 1^{\text{st}}$ channels are weaker by 3dB in terms of reflectivity.

Figure 3-5 shows the simulated reflection and transmission spectra of a typical SBG. As predicted by the analysis above, multiple channels appear in the spectra, with the given channel spacing λ_c. The reflectivity of the $\pm 1^{\text{st}}$-order is 3-dB lower than that of the 0th order. Also note that the even orders ($m = \pm 2, \pm 4, \cdots$) are eliminated from the spectra because $F_{\pm 2, \pm 4, \cdots} = 0$ according to Equation 3.21. This

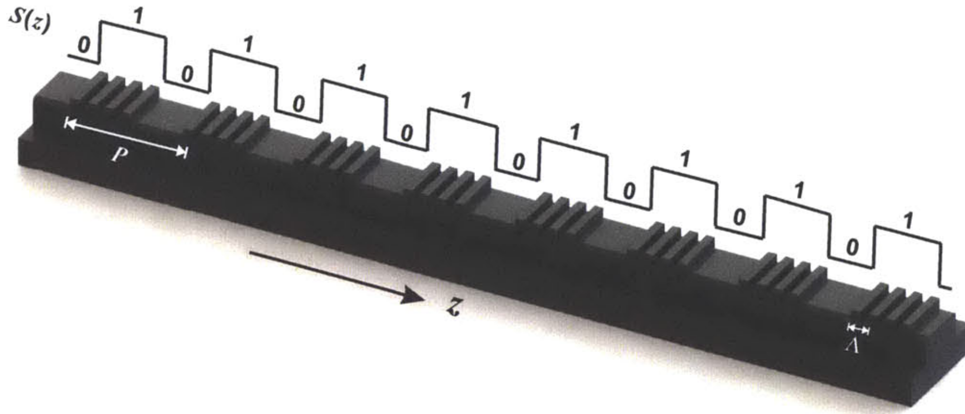

Figure 3-4 A schematic of an ordinary sampled Bragg grating (SBG) on a ridge waveguide. SBG can be seen as a uniform Bragg grating that is on-off modulated by an envelope function $S(z)$ that is usually periodic with a period P ($P \gg \Lambda$).

multi-channel spectra of the SBG can also be intuitively visualized with the Fourier transform shown by Equation 3.14, much like the generation of sidebands when a pure sinusoidal signal is modulated or sampled by a periodic function.

3.2.2 Sampled Bragg Grating with Arbitrary Filter Shapes

Now let us take a look at the key topic we seek to solve in this chapter: the design of arbitrary filters using the SBG, which is essentially a filter synthesis problem. Assume a specific filter with reflection spectrum $r(\lambda)$ is desired in the design. According to the Fourier transform relation between the reflection spectrum and the coupling coefficient $\kappa(z)$ given by Equation 3.14, the corresponding $\kappa(z)$ can be solved as

$$\kappa(z) = j\mathscr{F}^{-1}\left(r_\sigma\left(\frac{\sigma}{2}\right)\right) \tag{3.22}$$

where $r_\sigma\left(\frac{\sigma}{2}\right) = r(\lambda)$. The solution of $\kappa(z)$ can be represented by a complex

$$\kappa(z) = |\kappa(z)| \cdot \exp\left(j\varphi(z)\right) \tag{3.23}$$

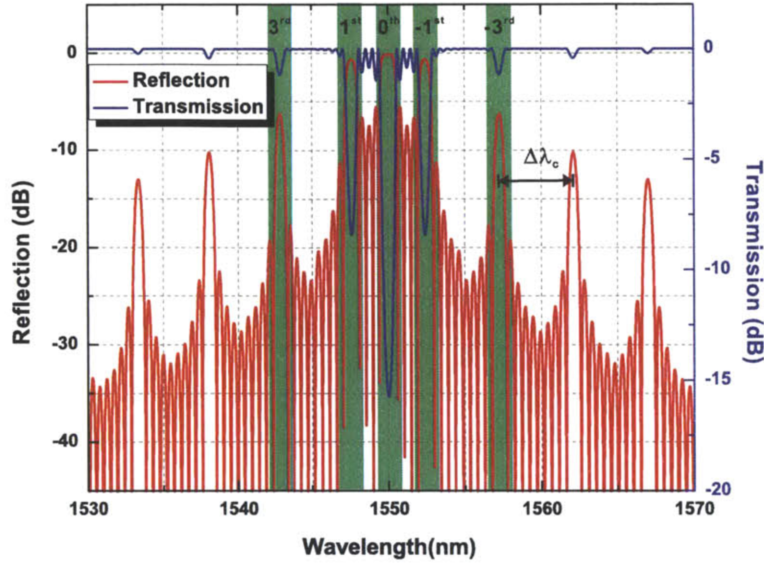

Figure 3-5 Simulated reflection and transmission spectra of a typical SBG. Multiple channels are generated in the spectra, with a channel spacing $\Delta\lambda_c$ indicated by Equation 3.20.

Using Equation 3.8, the refractive index modulation of the desired Bragg grating is

$$\Delta n_0(z) = \frac{2n_{\text{eff}}\Lambda}{\pi} \cdot \kappa(z) = \Delta n_1(z) \cdot \exp\left(j\varphi(z)\right) \tag{3.24}$$

where $\Delta n_1(z) = \frac{2n_{\text{eff}}\Lambda}{\pi} \cdot |\kappa(z)|$ is a real function. Using Equation 3.3, the filter synthesis problem now becomes how to design a Bragg grating whose refractive index modulation function $\Delta n(z)$ has the following form

$$\Delta n(z) = \frac{1}{2}\Delta n_1(z) \cdot \exp\left(j\left(\varphi(z) + \frac{2\pi z}{\Lambda}\right)\right) + c.c. \tag{3.25}$$

This problem can be further decomposed into two sub-problems

(1) To achieve a phase modulation $\exp\left(j\left(\varphi(z) + \frac{2\pi z}{\Lambda}\right)\right)$ in the perturbation refractive index $\Delta n(z)$.

(2) To achieve an amplitude or the grating strength modulation $\Delta n_1(z)$ in the

perturbation refractive index $\Delta n(z)$. This is essentially a grating apodization.

Now we introduce an 'imaginary'sampling function $S_1(z)$ whose Fourier series is designed to be

$$S_1(z) = \sum_{m=-\infty}^{\infty} F_m \exp\left(j\left(\frac{2m\pi}{P}z - m\varphi(z)\right)\right) \tag{3.26}$$

If a uniform Bragg grating is modulated by such a sampling function, according to Equation 3.17, the resulting SBG has a refractive index modulation

$$S_1(z) = \sum_{m=-\infty}^{\infty} F_m \exp\left(j\left(\frac{2m\pi}{P}z + \frac{2\pi}{\Lambda}z - m\varphi(z)\right)\right) \tag{3.27}$$

It is seen that the desired phase modulation in Problem (1) is achieved in the -1st-order ($m = -1$) of the SBG except for a trivial difference that the wavelength is shifter by $\Delta\lambda_c$. However, it is still not clear what the modulation function $S_1(z)$ looks like. Let

$$z_1 = z - \frac{P}{2\pi}\varphi(z) \tag{3.28}$$

Then the sampling function $S_1(z)$ is

$$S_1(z) = \sum_{m=-\infty}^{\infty} F_m \exp\left(j\frac{2m\pi}{P}z_1\right) \tag{3.29}$$

which is a standard on-off modulation in coordinate z_1, the same as the sampling function described by Equation 3.16 where its qth sampling starts at $z = q \cdot P$. By analogy, the qth sampling of $S_1(z) = 1$ starts at

$$z_1^q = z^q - \frac{P}{2\pi}\varphi(z^q) = q \cdot P \tag{3.30}$$

where $q \in \mathbb{N}$. Equation 3.30 can be numerically solved to find the corresponding sampling start point z^q so that the phase modulation $\exp\left(j\left(\varphi(z) + \frac{2\pi z}{\Lambda}\right)\right)$ can be

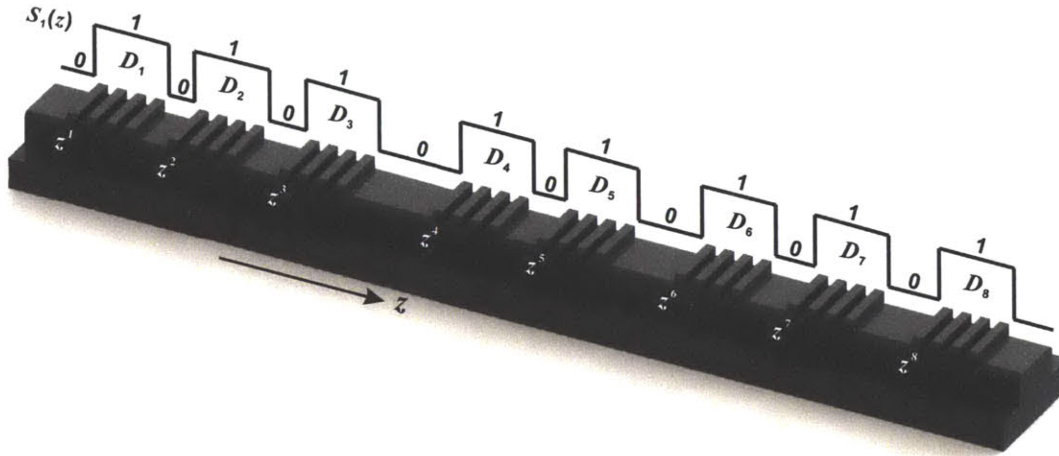

Figure 3-6 SBG with a non-periodic sampling function $S_1(z)$ to achieve arbitrary filter shape. The sampling position z_k and the duty cycle D_k of each sampling segment can be calculated by Equation 3.30 and Equation 3.31 respectively.

achieved in this SBG in its -1st channel. Figure 3-6 depicts the SBG with sampling function $S_1(z)$ which can achieve the desired phase modulation. Unlike the ordinary SBG, the sampling function $S_1(z)$ is non-periodic in this case. Problem (1) is now solved.

Next we will use an example to show the design procedure of arbitrary filter shape using the SBG based on the above analytical derivations. Our design target is a filter that has a super-Gaussian shape with 4-nm 3-dB bandwidth as the amplitude response of its reflection spectrum and a group delay dispersion of 20ps/nm as the phase response of its reflection spectrum. Figure 3-7(a) depicts the reflection spectrum of the targeted filter. With the Fourier transform given by Equation 3.22, the required grating coupling coefficient $\kappa(z)$ can be calculated, with amplitude $|\kappa(z)|$ and phase $\varphi(z)$, as shown by Fig. 3-7(b). By use of Equation 3.30, the sampling position z^q of the SBG can be obtained, as shown in Fig. 3-7(c). Using the sampling position z^q, the reflection spectrum of the SBG is simulated with the transfer matrix method, as shown in Fig. 3-8(a). Similar to the ordinary SBG, multiple channels are seen in the reflection spectrum. The even-order channels $m = \pm2, \pm4. \cdots$ are again suppressed because the duty cycle is kept at 0.5 for each sampling segment. Figure

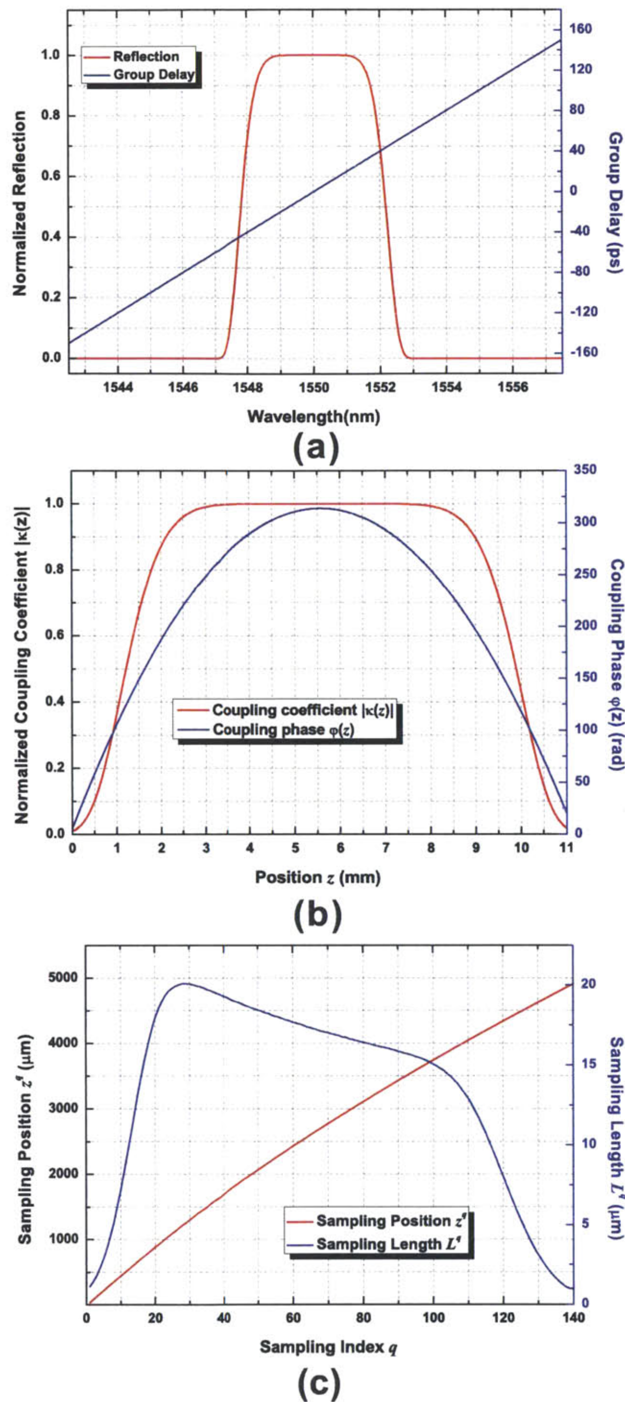

Figure 3-7 (a) The targeted filter shape with a super-Gaussian shaped amplitude of 4-nm bandwidth and a group delay dispersion of 20ps/nm in the reflection spectrum. (b) The calculated coupling coefficient of the desired grating $\kappa(z) = |\kappa(z)| \cdot \exp(\varphi(z))$. (c) The design parameters of the corresponding SBG: the sampling position z^q and the sampling length L^q in the qth sampling segment.

3-8(b) shows the close-up view of the -1st channel, where it is seen the desired filter response is achieved with super-Gaussian shaped reflection and linear group delay. However, it is also seen that the top of the reflection band is rough and the group delay has noticeable ripples.

The imperfect filter response of the SBG shown in Fig. 3-8(b) is because only Problem (1) is addressed so far by properly placing those sampling segments to achieve the desired phase modulation $\exp\left(j\left(\varphi(z) + \frac{2\pi z}{\Lambda}\right)\right)$, while the amplitude modulation in Problem (2) is not taken into account. Problem (2) is addressed by grating apodization, *i.e.* varying the grating strength along the grating direction. This is relatively easy to achieve in fiber Bragg gratings where the grating strength is determined by the exposure dose of the photosensitive fiber to ultraviolet light [34]-[35]. Grating apodization is not straightforward to apply in integrated Bragg gratings where planar fabrication process is used to make the gratings of the same depth. Though apodization can be achieved in sidewall gratings where the grating strength is controlled by the amount of the grating width etched into the waveguide sidewalls, precise control over the grating width is extremely challenging. However, the SBG structure provides a convenient method to apodize the grating. It is known that the strength of a segment of Bragg grating depends not only on the cross-sectional geometry of the grating but also on the length L of the grating. This can be seen from Equation 3.4 that the reflectivity of the grating is roughly determined by $\kappa \cdot L$. Therefore, changing the length L of the grating is equivalent to changing the cross-sectional geometry (*i.e.* κ) of the grating. As a consequence, apodization can also be realized by changing the length L^q of each sampling segment which is easy to employ with the planar fabrication process. In practice, this apodization is achieved in this work by adjusting the duty cycle of each sampling segment. The length L^q of the qth sampling segment is then given by

$$L^q = \frac{1}{2} \cdot \frac{|\kappa(z^q)|}{\max\{\kappa(z)\}} \cdot (z^q - z^{q-1}) \tag{3.31}$$

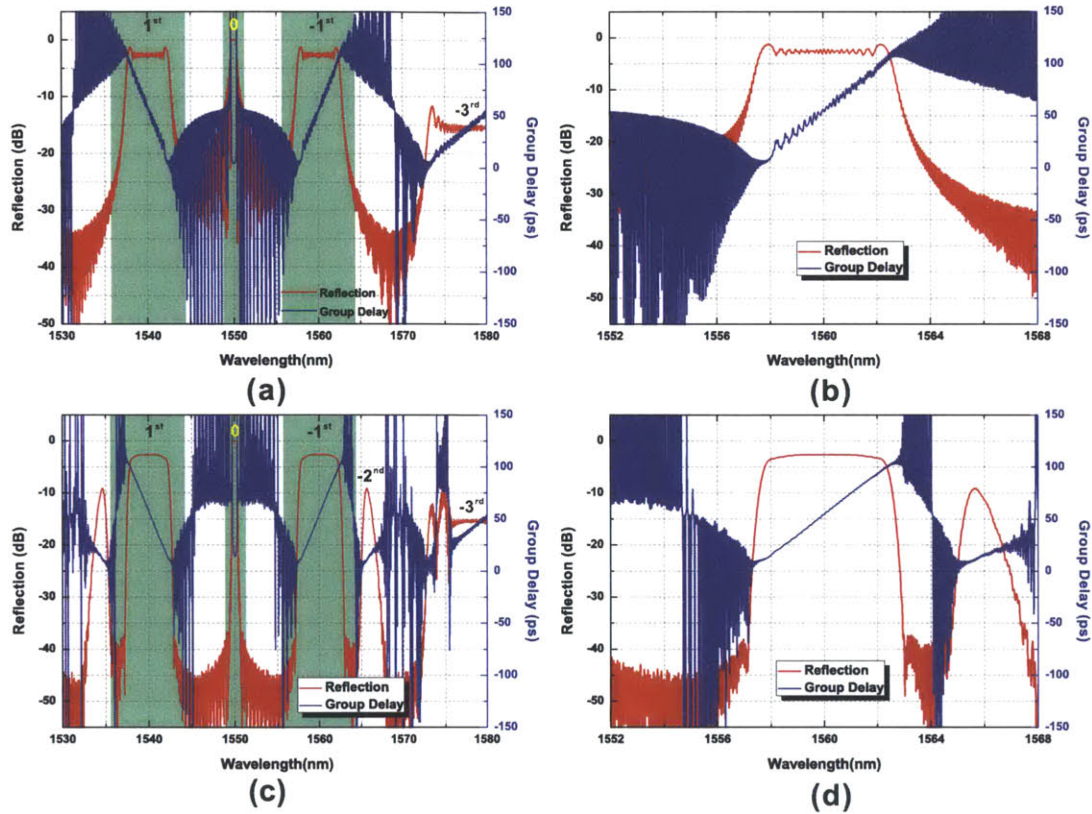

Figure 3-8 (a) The simulated reflection spectrum of the SBG with the designed sampling position. No apodization is applied. (b) A close-up view of the -1st channel. The targeted filter shape is realized. The reflection band of the filter is rough and the group delay has large ripples. (c) The simulated reflection spectrum of the SBG with the designed sampling position. The SBG is apodized with the duty-cycle apodization. (d) A close-up view of the -1st channel, where a smooth spectrum is achieved in the reflection band, as designed.

where the largest duty cycle in the sampling segments is 0.5. The blue curve in Fig. 3-7(c) shows the calculated segment length L^q of the qth sampling segment of the SBG to achieved the desired apodization profile $|\kappa(z)|$. Figure 3-8(c) and (d) show the simulated filter spectra of the SBG with the proposed duty-cycle apodization. It is seen the filter performance is largely improved with smooth reflection and group delay curves in comparison with the SBG without apodization shown in Fig. 3-8(a) and (b).

Till now we have demonstrated that arbitrary filter shape (but physically possible) can be realized in the SBG using the synthesis method discussed above. In spite of the complicated derivation shown above, the essence of this method lies in, in analogy to signal processing, that a specifically shaped sampling envelope maps to a sideband in the spectrum with a corresponding filter shape through Fourier transform. Adjusting the shape of the sampling envelope changes the filter shape in the sideband accordingly. The sampling envelope contains two parts, the amplitude which is realized through apodization and the phase which is realized by the position of the sampling. Although many side channels exist in the SBG spectrum, the ability to generate arbitrary filter shapes in one of these channels is technologically intriguing for on-chip optical signal processing such as arbitrary waveform generation and many other applications.

3.2.3 Sampled Bragg Grating with Phase Shift

Phase-shifted Bragg grating is a useful grating structure that has a broad range of applications such as the distributed feedback (DFB) semiconductor lasers [36]. As shown in Fig. 3-9(a), the phased shifted Bragg grating is formed by shifting the second half of the grating by a distance of ΔL. Therefore, its refractive index modulation $\Delta n(z)$ is

$$\Delta n(z) = \begin{cases} \Delta n_0 \cdot \exp\left(j\dfrac{2\pi z}{\Lambda}\right), & \textit{if} \;\; z < 0 \\ \Delta n_0 \cdot \exp\left(j\left(\dfrac{2\pi z}{\Lambda} + \dfrac{2\pi \Delta L}{\Lambda}\right)\right), & \textit{if} \;\; z > 0 \end{cases} \tag{3.32}$$

When $\Delta L = \Lambda/2$, a π phase shift is introduced. Since $\Lambda = \lambda_B/2$ where λ_B is the Bragg wavelength in the waveguide, this π phase shift is conventionally referred to as quarter-wave phase shift ($\Delta L = \lambda_B/4$). The quarter-wave phase shift structure is widely used in semiconductor DFB laser diodes to achieve single longitudinal lading mode with narrow bandwidth [37]. However, it is not easy to make high-quality quarter-wave phase shift Bragg gratings. Although electron beam lithography (EBL) is generally used to make such structures, the coherence of the grating generated by the EBL is usually poor. While interference lithography can make uniform gratings with perfect coherence, it is not straightforward how to introduce a phase shift in the uniform grating.

By use of the proposed SBG structure, such a phase-shitted Bragg grating can be easily achieved [38]-[40]. As shown by Fig. 3-10(a), the uniform grating is modulated by an envelope $S_1(z)$. A phase shift is inserted into $S_1(z)$ by shifting the second part ($z > 0$) of the sampling function by ΔL. The sampling function can be written as

$$\Delta S_1(z) = \begin{cases} S(z) = \sum\limits_{m=-\infty}^{\infty} F_m \exp\left(j\frac{2m\pi}{P}z\right), & if\ \ z < 0 \\ S(z+\Delta L) = \sum\limits_{m=-\infty}^{\infty} F_m \exp\left(j\left(\frac{2m\pi}{P}z + \frac{2m\pi\Delta L}{P}\right)\right), & if\ \ z > 0 \end{cases} \tag{3.33}$$

The refractive index modulation of this SBG is

$$\Delta n(z) = \begin{cases} \Delta n_0 \cdot \sum\limits_{m=-\infty}^{\infty} \exp\left(j\left(\frac{2\pi z}{\Lambda} + \frac{2m\pi z}{P}\right)\right), & if\ \ z < 0 \\ \Delta n_0 \cdot \sum\limits_{m=-\infty} \exp\left(j\left(\frac{2\pi z}{\Lambda} + \frac{2m\pi z}{P} + \frac{2m\pi\Delta L}{P}\right)\right), & if\ \ z > 0 \end{cases} \tag{3.34}$$

Compared to Equation 3.32, it is seen a quarter-wave phase shift is generated in the -1st channel when $\Delta L = P/2$. The quarter-wave phase shift based on the SBG takes advantage of the excellent coherence of the underline uniform grating fabricated by interference lithography, and the phase shift is generated by shifting the sampling

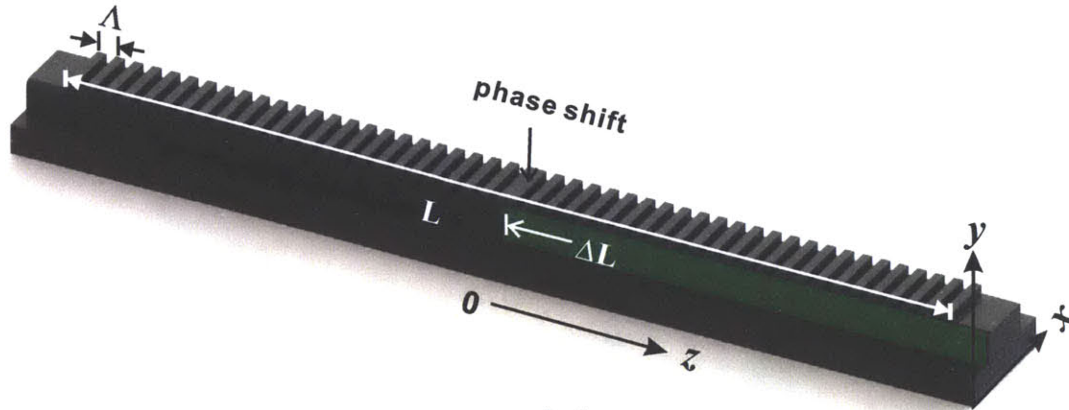

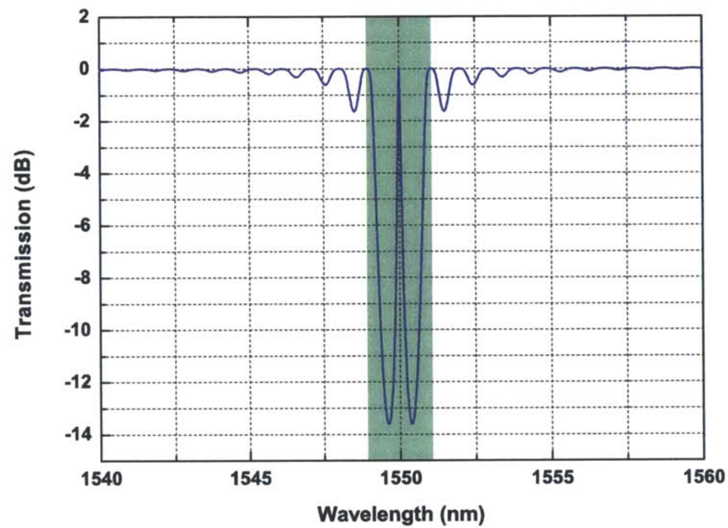

Figure 3-9 (a) A schematic of an ordinary phase-shifted Bragg grating. A defect is introduced in the periodic Bragg grating structure by shifting the second half ($z > 0$) of the Bragg grating by a distance ΔL. (b) Transmission spectrum of a quarter-wave phase-shifted Bragg grating. A transmission peak is observed in the photonic band gap, a characteristic spectrum of the phased-shifted Bragg grating.

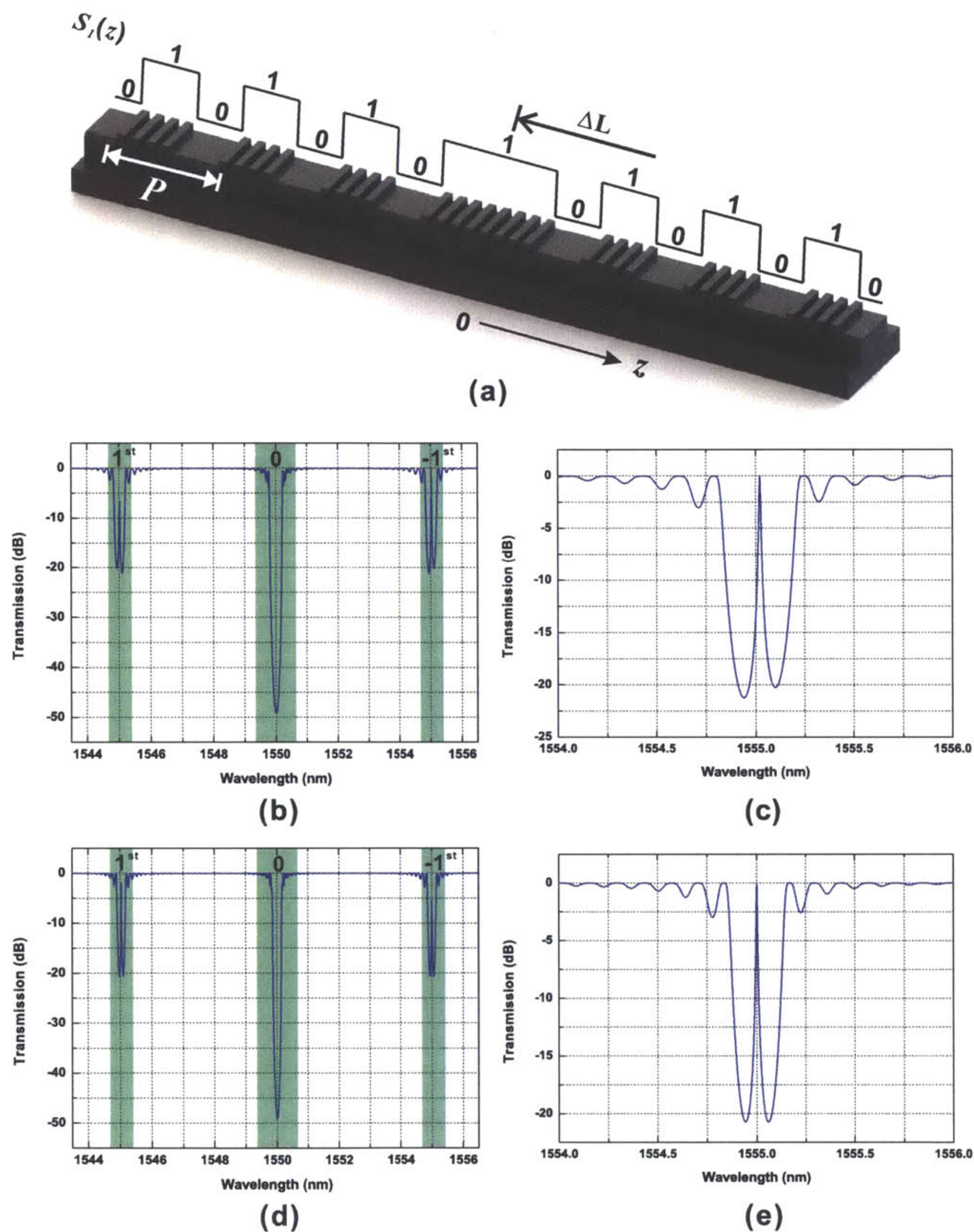

Figure 3-10 (a) A schematic of the SBG with a phase shift. A defect is introduced in the sampling function $S_1(z)$ instead of in the Bragg grating itself. (b) Transmission spectrum of the SBG with a quarter-wave phase shift. The characteristic shape of a quarter-wave phase shift grating is observed in the -1st channel. (c) A close-up view of the -1st channel. It is seen the spectrum is not symmetric about the resonance. (d) Transmission spectrum of the SBG with a quarter-wave phase shift with adjustment Δl applied. (e) A close-up view of the -1st channel. The spectrum is now symmetric because of the adjustment.

function by $P/2$ which is much larger than the grating period Λ and is thus much easier to control through optical lithography. Figure 3-10(b) shows the simulated transmission spectrum of the SBG, and Fig. 3-10(c) shows a close-up view of the -1st channel. It is seen the desired quarter-wave phase shift is achieved in the -1st channel. However, unlike the ordinary quarter-wave phase shift grating shown in Fig. 3-9(b), the spectrum in the -1st is not symmetric about the resonance. This can be improved by slightly adjusting the length ΔL by several percent determined by an optimization algorithm. Figure 3-10(d) shows the simulated SBG spectrum after the adjustment is applied, and a close-up view of the -1st channel is shown in Fig. 3-10(e).

Note that the wavelength of the resonance peak in the -1st channel is determined by

$$\lambda_c = 2n_{\mathrm{eff}}\Lambda + \Delta\lambda_c = 2n_{\mathrm{eff}}\Lambda + \frac{\lambda_0^2}{2n_{\mathrm{eff}}P} \tag{3.35}$$

where $\Delta\lambda_c$ is the channel spacing specified by Equation 3.20. In a DFB laser diode with quarter-wave phase shift, this resonance peak represents the lasing wavelength. This SBG-based quarter-wave phase-shift structure has its unique advantage in building multi-wavelength laser arrays that are widely used in optical transmission systems. In the ordinary phase-shift structure shown in Fig. 3-9, in order to change the lasing wavelength by 1nm, a change of the grating period well below 1nm is required according to Equation 3.1, which is extremely hard to achieve, let alone the fact that the wavelength spacing in modern optical transmission system can be as dense as 0.2nm. However, in the SBG-based quarter-wave phase-shift structure, the lasing wavelength is controlled by the sampling period P which is much easier to control since $P \gg \Lambda$. In order to change the lasing wavelength λ_c by 1nm, the change of sampling period P is

$$\Delta P = \left(\frac{P}{\Lambda}\right)^2 \cdot \frac{1}{2n_{\mathrm{eff}}} \text{ (nm)} \tag{3.36}$$

which is usually very large. Therefore, the quarter-wave phase-shift array can

now be easily fabricated using the SBG structure with the same underline grating generated by precise interference lithography and with different sampling periods P, as shown in Fig. 3-11.

3.3 Measured SBG with Phase Shift

In Section 3.2, we demonstrated arbitrary filter shapes can be realized in the SBG structure, such as the chirped grating shown in Section 3.2.2, and the quarter-wave phase-shift grating shown in Section 3.2.3. In this section, we will experimentally demonstrate the quarter-wave phase-shift grating in silicon as an example to show the fabrication techniques in making such SBGs.

Figure 3-11 shows the fabrication process flow used in this work to make the sampled Bragg grating in silicon. A SiO_2 masking layer is first deposited on top of an SOI wafer. Interference lithography with a simple Lloyd's mirror setup, followed by reactive ion etching (RIE) in CF_4, is used to form a uniform base grating in the SiO_2 mask as shown by Fig. 3-11(a). Interference lithography provides large-area gratings with good long-range spatial-phase coherence and precise period control. Next, the sampling pattern is defined using optical-contact-lithography, and transferred to the SiO_2 hard mask by wet etching with hydrofluoric acid (HF) as shown by Fig. 3-11(b). The optical mask of the sampling pattern is composed of many different sampling functions to achieve different filter shapes in one lithography step, such as the one discussed in Section 3.2.2 and the quarter-wave phase-shift array where the sampling period P is adjusted to obtain different resonant wavelengths. Low-resolution lithography can be used here as the feature size is usually large ($P \gg \Lambda$). A second optical-contact-lithography step is used to pattern the waveguide ridge in photoresist, followed by an HF etching to remove the excess grating hard mask on the sides of the ridge. Again, high-resolution lithography is not required here since the ridge waveguide can have a larger width w while still maintains single mode operation. Then the waveguide ridge is transferred to silicon by RIE with hydrogen bromide (HBr) gas, using the photoresist as the etch

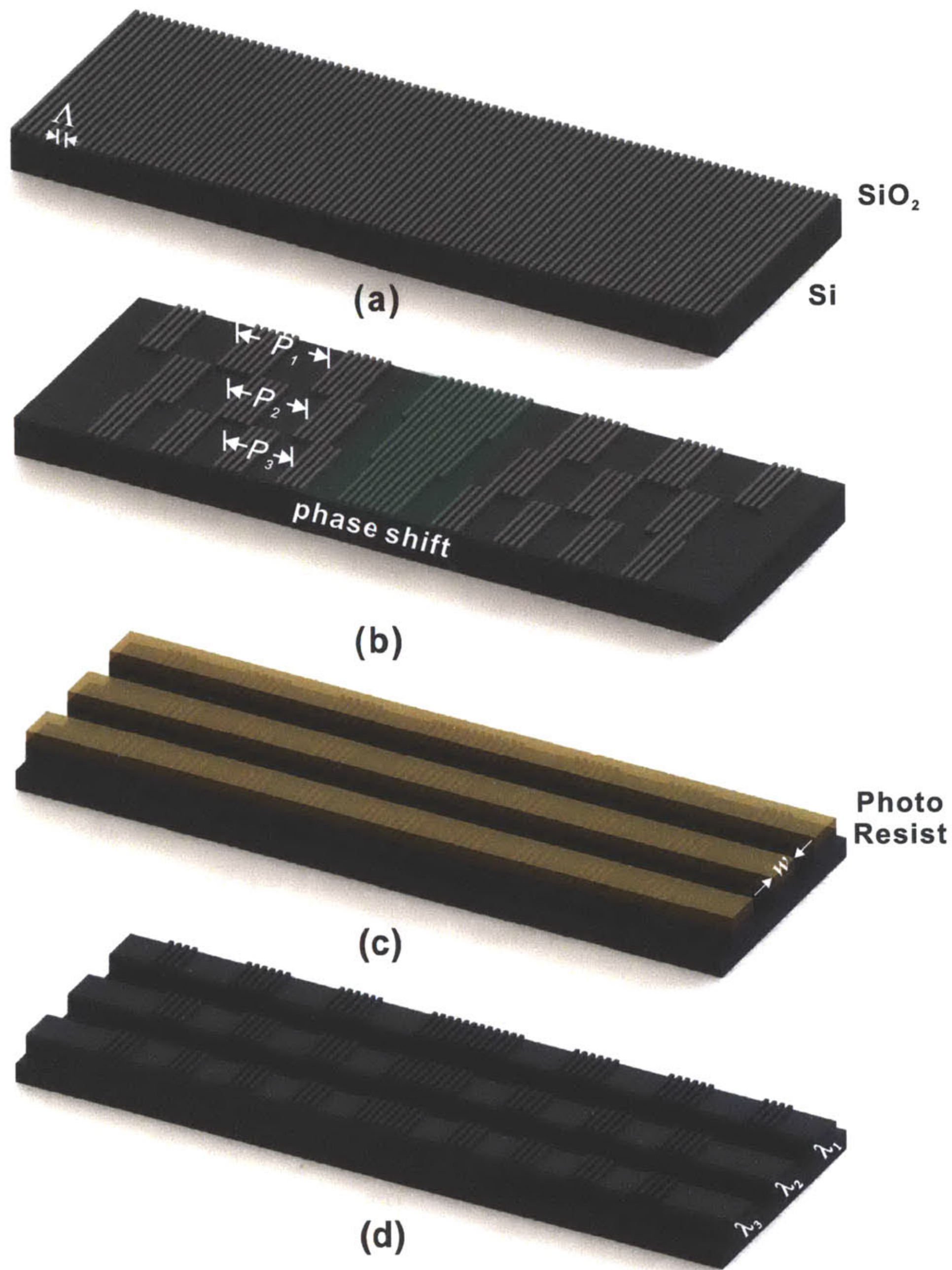

Figure 3-11 Fabrication process flow for the phase-shift Bragg gratings using the SBG structure. Note that only the silicon device layer of the SOI is shown.

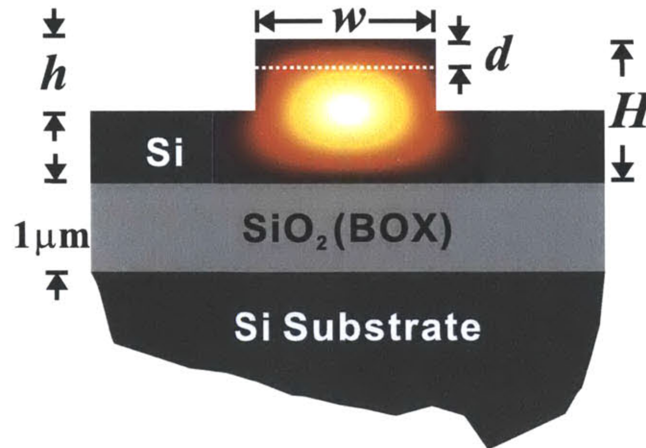

Figure 3-12 A schematic of the cross-section of the silicon ridge waveguide with grating on top. The fundamental TE mode profile is also shown.

mask as shown in Fig. 3-11(c). Finally, after removing the photoresist, a second HBr etching transfers the sampled grating into the silicon waveguide using the SiO_2 hard mask, followed by a final HF dip to remove the remaining SiO_2 hard mask, as shown by Fig. 3-11(d). Note that although metal is a commonly used etch mask in grating fabrication, it should be avoided in making silicon gratings since it introduces optical loss through silicide formation in the dry etching steps [41].

Figure 3-12 shows a schematic of the cross-section of the silicon ridge waveguide. The parameters of the waveguide are H = 1.4μm, h = 0.8μm, w = 2.2μm, and the grating depth d is 0.28μm. These dimensions ensured that a single transverse-electric (TE) mode, whose mode profile is also shown in Fig. 3-12, propagates with an effective refractive index of 3.41. The mode overlap with the grating region provided a grating coupling coefficient of 102cm^{-1}, calculated from coupled-mode theory as shown in Equation 3.7. The period Λ of the base grating is 219nm and the sampling period P was 21.2μm (P/Λ = 97), corresponding to a channel spacing $\Delta\lambda_c$ = 15.5nm. The length ΔL is set to around 10.6μm to generate a quarter-wave phase-shift. Figure 3-13 shows the scanning-electron micrographs of the fabricated SBG. It is seen the uniform Bragg grating is modulated on and off on top of the silicon ridge waveguide.

Figure 3-14 shows the measured spectrum of the fabricated SBG. Multiple chan-

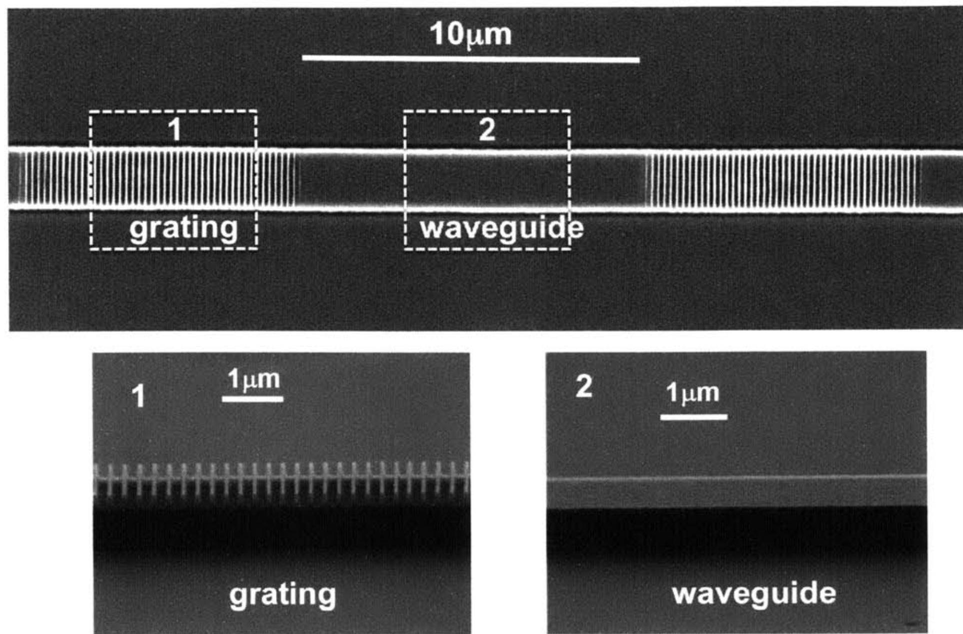

Figure 3-13 Scanning-electron micrographs of the fabricated SBG. The uniform Bragg grating is modulated on and off on top of the silicon ridge waveguide.

nels are seen, which is a characteristic property of sampled Bragg grating. In particular, the -1st channel has a transmission peak, an indicator that a quarter-wave phase shift is formed. Note that the transmission peak is not as sharp as that in simulation, because of the presence of optical loss in the cavity. Simulation shows a high optical loss of 14.6dB/cm exists in the cavity, as shown by the red curve in Fig. 3-14(b). The material absorption loss is around 7.8dB/cm since the device layer of the SOI used in this work is moderately doped. This problem could be solved by use of an SOI with an intrinsic silicon device layer. The blue line in Fig. 3-14(b) simulates the transmission spectrum with the material absorption loss eliminated. The scattering from the rough edges of the waveguide and from the grating accounts for the other 6.6dB/cm loss which could be reduced with an improved fabrication process with a better line edge roughness control.

In this chapter, we developed a method to design any physically possible optical filter based on the sampled Bragg grating (SBG). The method is verified by simulation as well as an experimental demonstration of an SBG with a quarter-

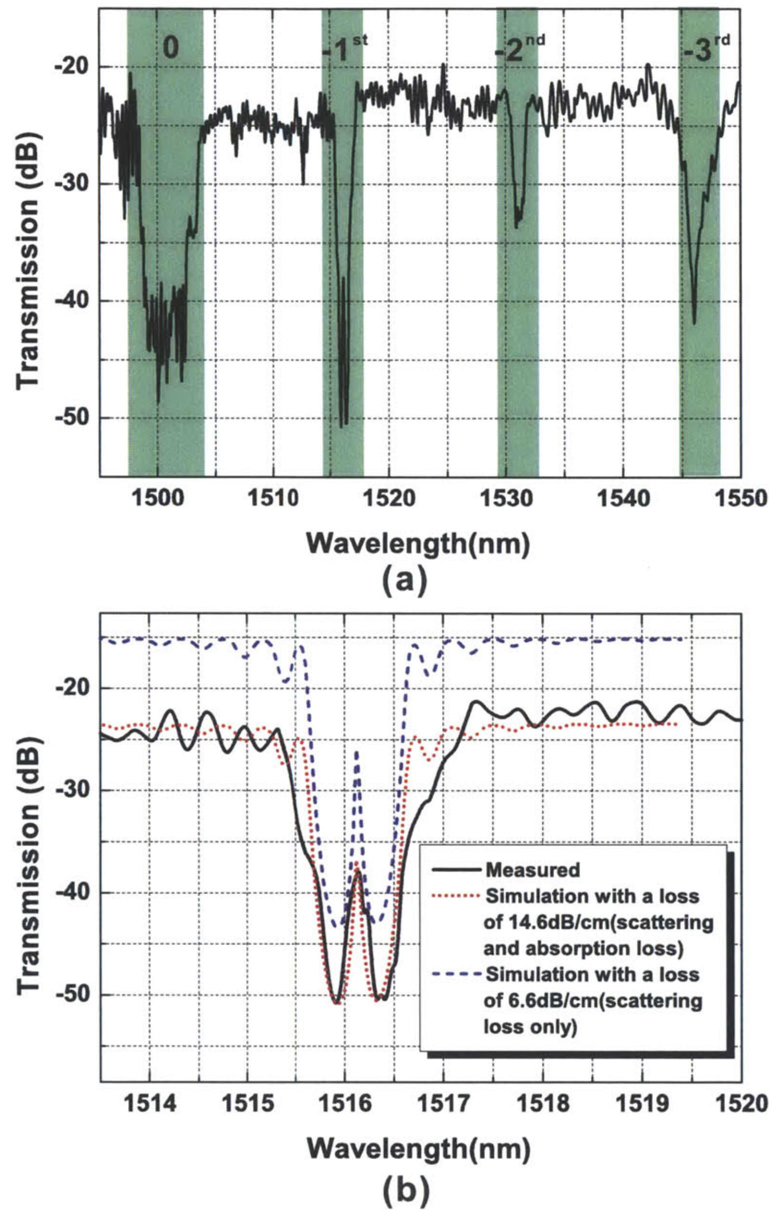

Figure 3-14 (a) Measured transmission spectrum of the fabricated SBG designed to form a quarter-wave phase-shift grating. Multiple channels are seen in the spectrum. (b) A close-up view of the -1st channel. A transmission peak is seen inside the band gap, as seen in ordinary quarter-wave phase-shift gratings. Simulations accounting for the optical losses are also provided.

wave phase shift. The SBG structure shows unique advantage in making arbitrary optical filters in particular the DFB laser arrays using the proposed quarter-wave phase-shift structure. Although silicon is used as the wave-guiding material in the experimental demonstration of the quarter-wave phase-shift structure, the method in general applies to any material system such as the III-V material for semiconductor laser diodes. Even the silicon-based quarter-wave phase-shift structure could find many potential applications for silicon photonic on-chip communications, such as the wavelength-division-multiplexing (WDM) laser arrays with the aide of III-V materials [6] or Erbium doped cladding as gain medium [7].

Part II

Toward Large-scale Silicon Photonic Integration

Chapter 4	Nanophotonic Phased Array: Theory	73
Chapter 5	Large-scale Passive Phased Array	93
Chapter 6	Large-scale Active Phased Array	125

As discussed in Part I, accurate silicon photonic devices can be individually fabricated with high performance through various ways. However, without the successful integration of a large number of such devices to form a functional silicon photonic system, all of the advantages brought by these high-performance components will be in vain. In Part II, a demonstration showing the integration ability of silicon photonics is presented, where more than 4,000 silicon photonic components are successfully integrated on a silicon chip and work together to form a functional system, representing the largest silicon photonic integration demonstrated to date.

CHAPTER 4

Nanophotonic Phased Array: Theory

In his Nobel lecture in 1909, the German physicist Karl Ferdinand Braun remarked: "It had always seemed most desirable to me to transmit the waves, in the main, in one direction only" [42]. The device Braun was referring to and for which he was recognized was later on known as the phased array in which the phase of the electromagnetic wave in an array of antennas is used to shape the radiation. Light, as an electromagnetic wave, can also form optical phased arrays to engineer the optical radiation from an array of optical antennas. This chapter will study the theory of optical phased array, from analytical derivations to numerical simulations. The analysis and simulation discussed in this chapter will be serving as the foundation and a powerful tool in the experimental work that will be shown in the following chapters.

4.1 1-Dimensional Optical Phased Array

4.1.1 A Revisit to Young's Interference Experiment

Optical phased array is familiar to most people from high-school physics. As shown in Fig. 4-1, the famous Young's interference experiment, namely the double-slit experiment, can be considered as a 1-D optical phased array comprising only two optical antenna elements in x-direction located at $x_1 = -d/2$ and $x_2 = d/2$ respectively. According to the superposition principle of electromagnetic waves, the electric field in a far-field point with polar angle θ is the superposition of waves from the two optical antennas

$$E(\theta) = e^{-j\mathbf{k}_1\cdot\mathbf{r}_1} + e^{-j\mathbf{k}_2\cdot\mathbf{r}_2} \tag{4.1}$$

where $\mathbf{k}_1$, $\mathbf{k}_2$ are the wave vectors from the antennas to the far-field point, and $\mathbf{r}_1$, $\mathbf{r}_2$ are the corresponding spatial vectors. The electric field $E(\theta)$ is treated hereon as a scalar since we only consider the transverse-electric (TE) field which is also the predominant polarization that will be used throughout Part II. In the far-field approximation where $d \ll L$, the following assumption can be made: $\mathbf{k}_1 \approx \mathbf{k}_2 \approx \mathbf{k}$, where $\mathbf{k}$ represents the wave vector from the origin to the far-field point. Therefore, the far field becomes

$$E(\theta) = e^{-j\mathbf{k}\cdot\mathbf{r}_1} + e^{-j\mathbf{k}\cdot\mathbf{r}_2} = e^{-j\mathbf{k}\cdot\mathbf{r}} \cdot (e^{-j\mathbf{k}\cdot(\mathbf{r}_1-\mathbf{r})} + e^{-j\mathbf{k}\cdot(\mathbf{r}_2-\mathbf{r})}) = e^{-j\mathbf{k}\cdot\mathbf{r}} \cdot (e^{-j\mathbf{k}\cdot\mathbf{x}_1} + e^{-j\mathbf{k}\cdot\mathbf{x}_2}) \tag{4.2}$$

where $\mathbf{r}$ is the vector pointing to the far field point, and $\mathbf{x}_1$, $\mathbf{x}_2$ are the vectors pointing from $(x_1, 0)$, $(x_2, 0)$ to the origin respectively. Discarding the fast oscillating phase

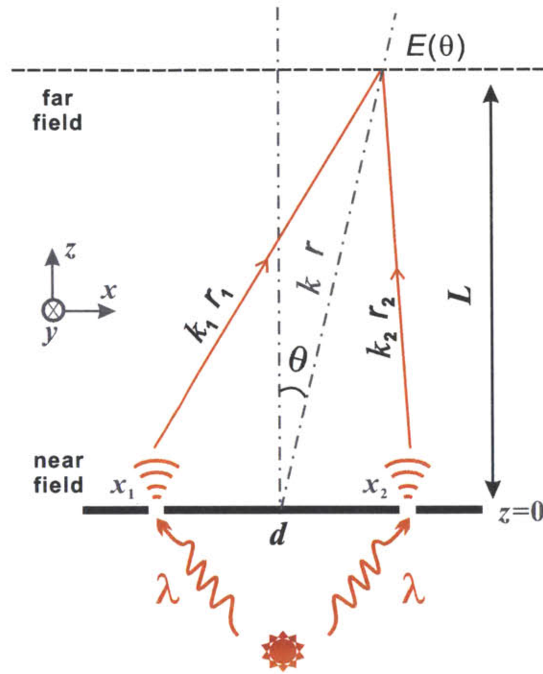

Figure 4-1 The simplest optical phased array: Young's interference experiment.

$e^{-j\mathbf{k}\cdot\mathbf{r}}$ gives (since only the far-field intensity is of interest)

$$E(\theta) = \sum_{n=1}^{2} e^{j2\pi\cdot(x_n \sin\theta)/\lambda} \tag{4.3}$$

where λ is the optical wavelength in the free-space medium. The interference between the two optical antennas produces a bright spot in the center ($\theta = 0$) of the far field with an intensity distribution proportional to $\cos^2(\pi\frac{d}{\lambda}\sin\theta)$. When $d > \lambda/2$, high interference orders come up with multiple bright spots in the far field. This is what we learnt from high-school physics.

More generally, when the phased array contains N antennas placed periodically along x-direction at $x_n (1 \le n \le N)$, and each antenna emits with certain amplitude $|w_n|$ and phase φ_n, the above Equation 4.3 becomes

$$E(\theta) = \sum_{n=1}^{N} w_n \cdot e^{j2\pi\cdot(x_n \sin\theta)/\lambda} \tag{4.4}$$

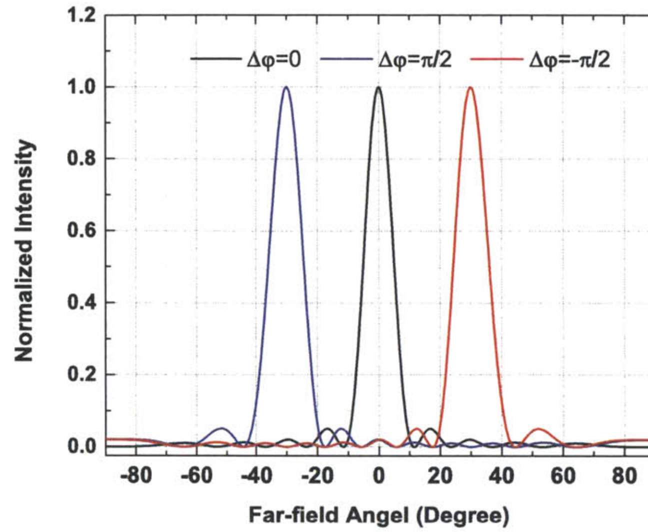

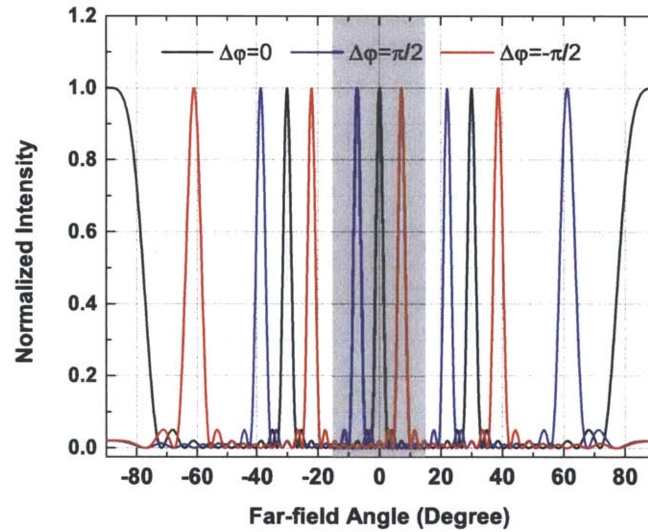

Figure 4-2 (a) The far-field intensity (simulation) of a 1-D optical phased array with 10 optical antennas and antenna spacing $d = \lambda/2$ under different phase increment $\Delta\varphi = \varphi_n - \varphi_{n-1}$. Black: $\Delta\varphi = 0$, Blue: $\Delta\varphi = \pi/2$, and Red: $\Delta\varphi = -\pi/2$. (b) The far-field (intensity) simulation of the same array but with a larger antenna spacing $d = 3\lambda$, where high interference orders show up. The shaded area corresponds to the 0th order.

where $w_n = |w_n| \cdot e^{j\varphi_n}$ describes the emission characteristic of antenna n. Equation 4.4 is a general analytical description of phased array, which can be immediately extended to 2-D case in the following section and will be used extensively throughout this work. Figure 4-2 simulates the far-field intensity pattern of a 10-element optical phased array with different inter-element spacings and phase configurations. It is noted that

- Multiple interference orders are generated in the far field when the inter-element spacing is larger than half of the free-space wavelength λ.
- The far-field intensity lobes move around as the phase configuration changes. This is the basic concept of optical beam steering with optical phased arrays, as will be discussed in Chapter 6.
- As shown in Fig. 4-2(a), there exist many low-intensity side lobes around the main lobe in the far field. This is caused by the finite number of antenna elements in the phased array, which will be discussed in Section 4.1.2 and will be dealt with in Chapter 6.

4.1.2 Phased Array: A Fourier System

In general, all of the linear and time-invariant optic systems are Fourier systems in the sense that the near-field emission and the far-field pattern are related by the simple yet powerful Fourier transform. The Fourier nature of phased arrays can be readily seen from Equation 4.4 when the coordinate transformation $u = \sin(\theta)/\lambda$ is applied

$$E(u) = \sum_{n=1}^{N} w_n \cdot e^{j2\pi x_n \cdot u} = \mathscr{F}(w_n) \tag{4.5}$$

where $\mathscr{F}$ denotes the discrete Fourier transform between the near-field emission w_n and the far-field electric field pattern $E(u)$.

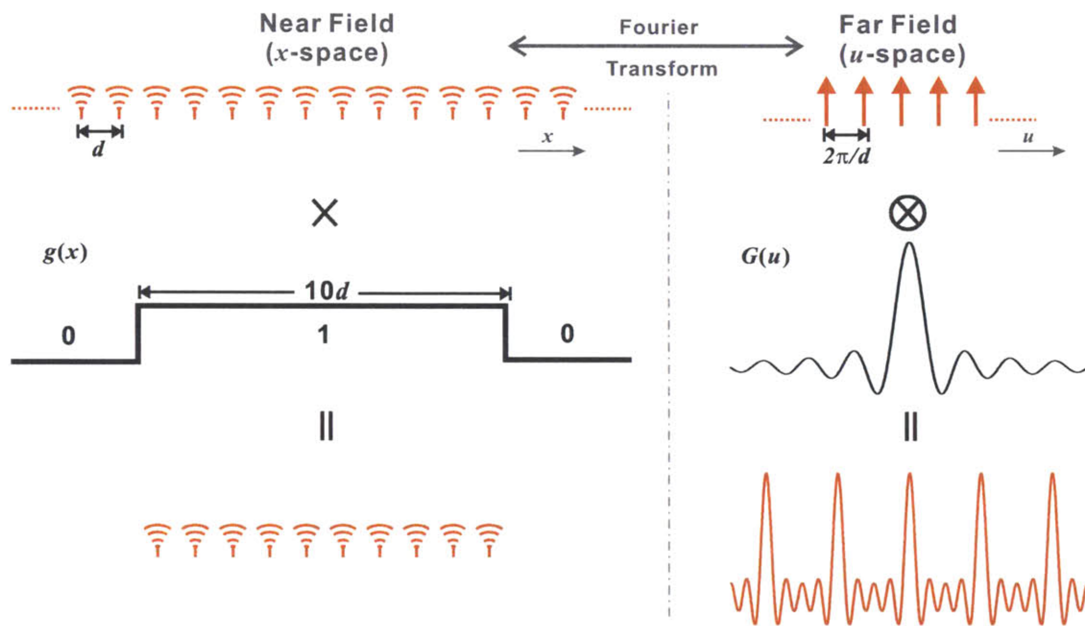

Figure 4-3 Understanding phased array using Fourier transform. The near field of a finite phased array can be seen as the multiplication of an infinite phased array and a rectangular function. Correspondingly, the far field is the convolution of an infinite Dirac comb with a *sinc*-function.

Next let's take a look back at how the far-field interference pattern is formed in Fig. 4-2 from a Fourier transform point of view. As illustrated in Fig. 4-3, the near-field emission $e(x)$of the phased array containing 10 ideal point sources can be considered as a Dirac comb with spatial period d (since each ideal point source can be described by a Dirac δ-function) multiplied by a rectangular envelope $g(x)$ with a width to fit in 10 antennas:

$$e(x) = g(x) \times \sum_{n=-\infty}^{\infty} \delta(x - x_n) \tag{4.6}$$

The far-field pattern $E(u)$ is the Fourier transform of the near-field emission $e(x)$

$$E(u) = \mathscr{F}[g(x)] \otimes \mathscr{F}[\sum_{n=-\infty}^{\infty} \delta(x - x_n)] = G(u) \otimes \sum_{n=-\infty}^{\infty} \delta(u - n\frac{2\pi}{d}) \tag{4.7}$$

where $G(u)$ is the Fourier transform of the rectangular envelope which is a *sinc*-function with a main lobe and many side lobes, as already seen in Fig. 4-2(a). The Fourier transform of the x-space Dirac comb is still a Dirac comb in the u-space with a period of $1/d$. The multiplication in the near field becomes convolution in the far field, which gives the final far-field pattern

$$E(u) = \sum_{n=-\infty}^{\infty} G(u - n\frac{2\pi}{d}) \tag{4.8}$$

It is seen that the far-field pattern is a *sinc*-function train with a separation of $1/d$. Note that u is bounded to $[-1/\lambda, 1/\lambda]$ by definition. Therefore the number of *sinc*-function periods in the far field is given by

$$N_u = \frac{2d}{\lambda} \tag{4.9}$$

indicating that high-order patterns arise when $d > \lambda/2$ as already observed in Fig. 4-2.

In this section, we analyzed the optical phased array with the simple yet powerful Fourier transform tool, both in an analytical form given by Equation 4.5 and in a picturable form as presented in Fig. 4-3. The analytical equation offers a rigorous method to design and simulate phased arrays, while the Fourier transform picture provides valuable intuitions for phased-array design and analysis. Both methods are important and will be extensively used throughout this work.

4.2 Large-scale 2-Dimensional Phased Array

In the last section, we saw that a bright spot can be generated in the far field with only a few antenna elements, and the position of the spot can be adjusted by changing the relative phase of the antennas. Suppose that instead of having only a few antennas lined up in 1D we have thousands of antennas placed in 2D, what can we achieve in the far field out of this large-scale phased array? Given what we have seen in the last section, we should be able to generate a lot of bright spots in the far field; furthermore, by carefully engineering the relative phase of the thousand of antennas to adjust the spot positions, we should be able to form a meaningful image by these spots. The goal of this section is to create a synthesis method to generate arbitrary interference patterns in the far field by properly designing the relative phase of a large number of antennas.

As shown in Fig. 4-4, a large-scale ($M \times N$) phased array is placed on the $x - y$ plane which is also the equator plane of a spherical coordinate system. Under the far-field approximation and the assumption that each antenna is an ideal point source, the far-field expression of the phased array in Equation 4.4 can be immediately extended to this 2-D case

$$E(\theta, \phi) = AF(\theta, \phi) = \sum_{m=1}^{M} \sum_{n=1}^{N} w_{mn} \cdot e^{j2\pi/\lambda(x_m \sin\theta \cos\phi + y_n \sin\theta \sin\phi)} \tag{4.10}$$

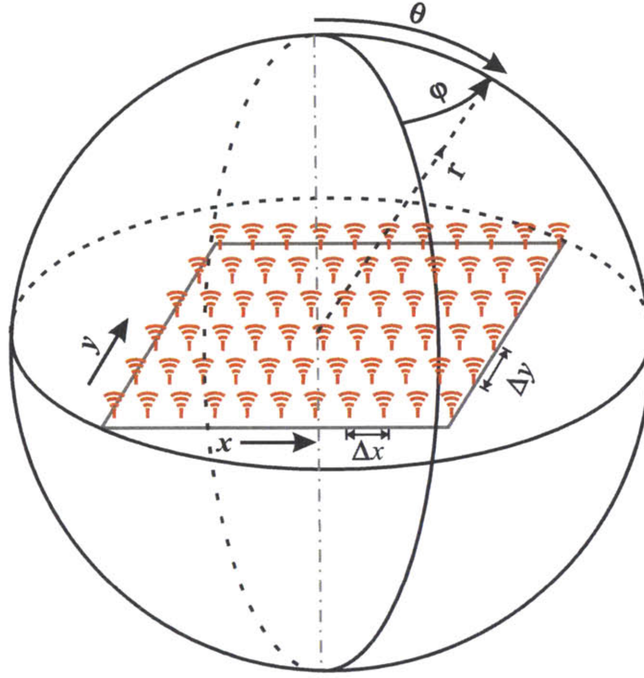

Figure 4-4 Schematic of 2-D phased array. The near field is described in Cartesian coordinate (x, y, z), and the far field is characterized by spherical coordinate (r, θ, ϕ).

where (x_m, y_n) is the position of the antenna element in the near-field Cartesian coordinate, while (θ, ϕ) is the far-field position in a spherical coordinate. w_{mn} defines the emission amplitude $|w_{mn}|$ and emission phase φ_{mn} of the antenna. When each antenna is considered as an ideal point source, the far-field of the phased array is conventionally referred to as the '*Array – Factor*' which is hereby denoted by $AF(\theta, \phi)$. $AF(\theta, \phi)$ is a complex number that can be written as $AF(\theta, \phi) = |AF(\theta, \phi)|e^{j\Phi(\theta,\phi)}$. Similar to the procedure taken in the last section, using the coordinate transformation

$$\begin{cases} u = \sin\theta \cos\phi/\lambda \\ v = \sin\theta \sin\phi/\lambda \end{cases} \tag{4.11}$$

the array factor $AF(\theta, \phi)$ becomes [43]

$$AF(\theta, \phi) = |AF(\theta, \phi)|e^{j\Phi(\theta,\phi)} = \sum_{m=1}^{M}\sum_{n=1}^{N} w_{mn} \cdot e^{j2\pi(x_m \cdot u + y_n \cdot v)} = \mathscr{F}(w_{mn}) \tag{4.12}$$

which again shows the Fourier transform relation between the near-field emission w_{mn} and the far-field pattern $AF(\theta, \phi)$. With Equation 4.12, one should be able to find a unique near-field combination w_{mn} corresponding to a certain far-field $AF(\theta, \phi)$, by simply applying an inverse Fourier transform to $AF(\theta, \phi)$. However, in phased arrays the emission amplitude $|w_{mn}|$ is usually kept uniform across the whole array, meaning $\forall m, n : |w_{mn}| = 1$. With this constraint, it seems not possible to generate arbitrary far field with phased arrays. Fortunately, there exists another degree of freedom that only the amplitude $|AF(\theta, \phi)|$ of the far field is of interest for the purpose of creating images while its phase part $\Phi(\theta, \phi)$ can be arbitrary. The Gerchberg-Saxton (GS) algorithm, [44] which is commonly used in holography, can be modified to solve this complex antenna synthesis problem, as described as follows. Figure 4-5 illustrates the block diagram of this modified GS algorithm. At the kth iteration, an approximated far field $AF^k(\theta, \phi)$ consisting of the desired amplitude $|AF(\theta, \phi)|$ and a trial phase $\Phi^k(\theta, \phi)$ is inversely Fourier-transformed to get the corresponding w_{mn}^k of each antenna, according to the Fourier transform relation between the two given by Equation 4.12. The far-field trial phase $\Phi^k(\theta, \phi)$ is not of interest and is arbitrarily chosen. The amplitude of w_{mn}^k is then set to 1 while its phase $e^{j\varphi_{mn}^k}$ is kept so that the amplitude of the antennas is uniform across the array. Therefore the updated far field $AF^{*k}(\theta, \phi)$ is obtained through Fourier transform whose phase $\Phi^{*k}(\theta, \phi)$ is passed to the $(k+1)^{th}$ iteration as the new trial phase $\Phi^{k+1}(\theta, \phi)$. The initial trial phase of the radiation field is set to $\Phi^1(\theta, \phi) = 0$ or any arbitrary values in the 1st iteration. After several iterations, the final far field $AF^{*k}(\theta, \phi)$ generated by the phase $e^{j\varphi_{mn}^k}$ should converge to the desired pattern $|AF(\theta, \phi)|$.

Figure 4-6 shows two antenna synthesis demonstrations using the modified GS

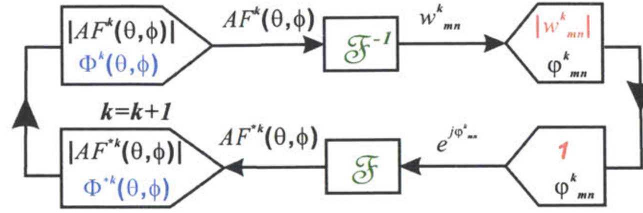

Figure 4-5 The iterative Gerchberg-Saxton (GS) method modified to retrieve the individual antenna phase φ_{mn} for an arbitrarily given far-field pattern $|AF(\theta,\phi)|$.

algorithm. The phased array scale is assumed to be 64×64 with an inter-element spacing (or pixel pitch) $\lambda/2$ in both x and y directions to ensure a single interference order in the far field. Figure 4-6(a) shows the resulting far-field pattern with an "MIT" logo, and Fig. 4-6(c) shows the corresponding phase of the $64 \times 64(4,096)$ antennas synthesized from the modified GS algorithm. Figure 4-6(b) demonstrates a multiple-beam pattern with 9 beams centered at the zenith, and $\theta = l \cdot \frac{\pi}{4}(l \in \mathbb{Z}, 0 \leq l < 8)$, while Fig. 4-6(d) illustrates the corresponding antenna phase. Note that since the Fourier transform pairs (in Equation 4.12) are between the near-field Cartesian coordinate (x,y) and the far-field spherical coordinate (θ,ϕ), the far-field patterns are plot in a polar coordinate with θ as the polar axis, ϕ as the polar angle and the far-field zenith as the origin. Because of the coordinate system of chosen, the shape of the image is stretched, compared to the targeted image shown in the inset of Fig. 4-6(a). Also note that only the upper hemisphere of the far field is shown ($0 \leq \theta \leq \frac{\pi}{2}$) since the lower hemisphere is just a mirror image of the upper hemisphere.

To measure the efficiency of the modified GS algorithm, a figure of merit C^k is defined as the relative far-field pattern change in the kth iteration step:

$$C^k = \frac{\iint\limits_{\Omega} ||E^{*k}(\theta,\phi)|^2 - |E^{*(k-1)}(\theta,\phi)|^2| d\Omega}{\iint\limits_{\Omega} |E^{*k}(\theta,\phi)|^2 d\Omega} \tag{4.13}$$

where $d\Omega = \sin\theta d\theta d\phi$ is the solid angle, and the integral is taken over the upper

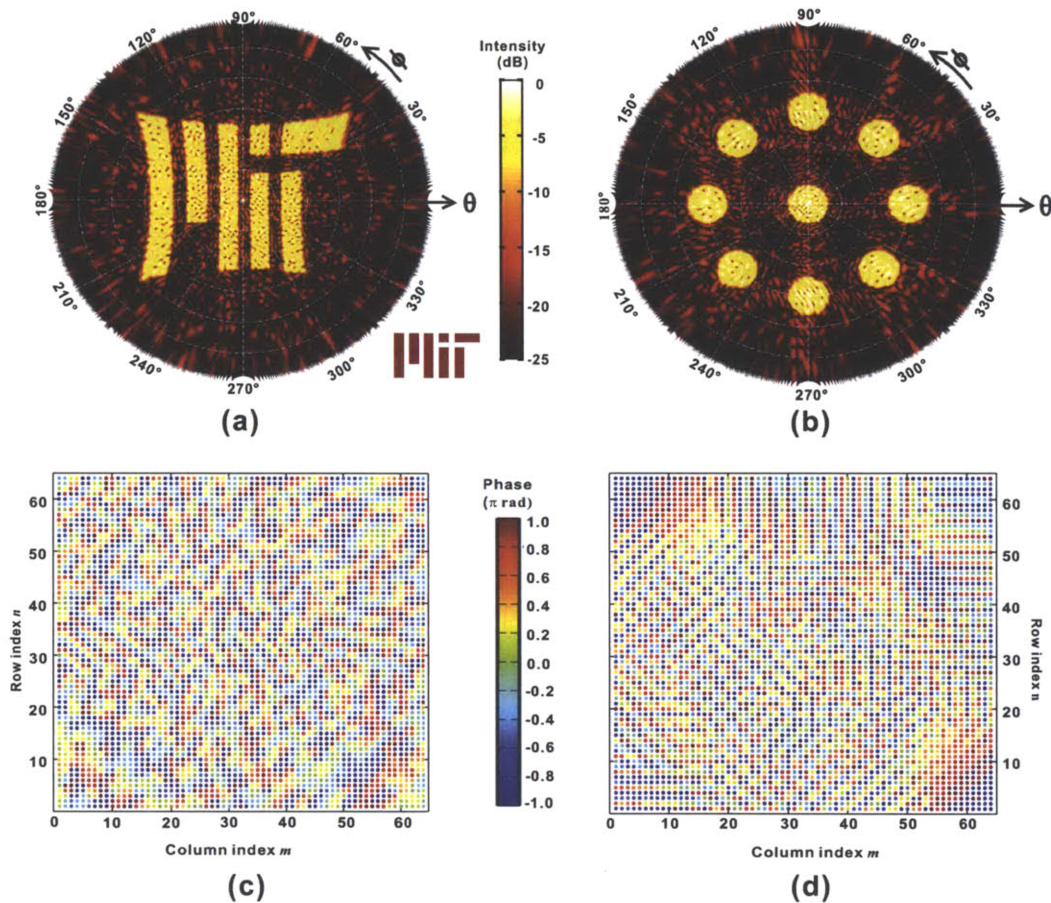

Figure 4-6 Phased array synthesis. (a) The simulated far-field array factor pattern $AF(\theta, \phi)$- the MIT-logo "MIT" by a 64×64 phased array. The inset on the lower-right corner shows the targeted image. (b) The simulated far-field array factor pattern aiming to generate multiple beams with different angles in the far field, which may prove useful in optical free space communications. A pixel pitch of $\lambda/2$ was chosen in these simulations. (c) The color plot of the phase of the array corresponding to the "MIT" pattern. (d) The color plot of the phase of the array corresponding to the multiple-beam pattern.

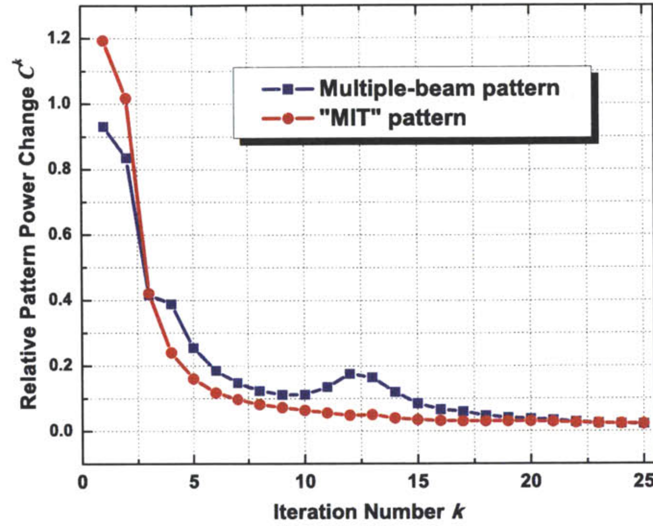

Figure 4-7 The convergence rate of the two examples using the modified GS algorithm. In both cases, the algorithm converges fast toward the targeted pattern, showing the proposed algorithm is efficient in antenna synthesis for large-scale phased arrays.

hemisphere where $\phi \in (0, 2\pi)$ and $\theta \in (0, \pi/2)$. Figure 4-7 shows the convergence curve of the two examples. It is seen that in both cases, the final far-field pattern approximates the desired pattern with a fast convergence rate, which confirms the efficiency of the proposed phased-array synthesis method.

In the far-field simulations in Fig. 4-6, the pixel pitch is assumed to be $\lambda/2$. However, in reality it is really hard to make such a small pixel pitch in optical phased arrays, considering the short optical wavelength ($\lambda = 1.55\mu\text{m}$) that will be used in this work. We have already seen in Fig. 4-2 that multiple interference orders will be formed when the antenna spacing is larger than half of the free space wavelength. It is the same with 2-D phased arrays except that the high-order interference patterns are now replicated in two dimensions. Figure 4-8 simulates the far-field pattern generated by the same 64×64 phased array as in Fig. 4-6(a) with a larger pixel pitch $\Delta_x = \Delta_y = 9\mu\text{m}$. The number of interference orders is again determined by Equation 4.9 which gives 12 ($N_u = 2\Delta_x/\lambda \approx 12, N_v = 2\Delta_y/\lambda \approx 12$) replicated patterns in both directions in the far field, as confirmed by the simulation result.

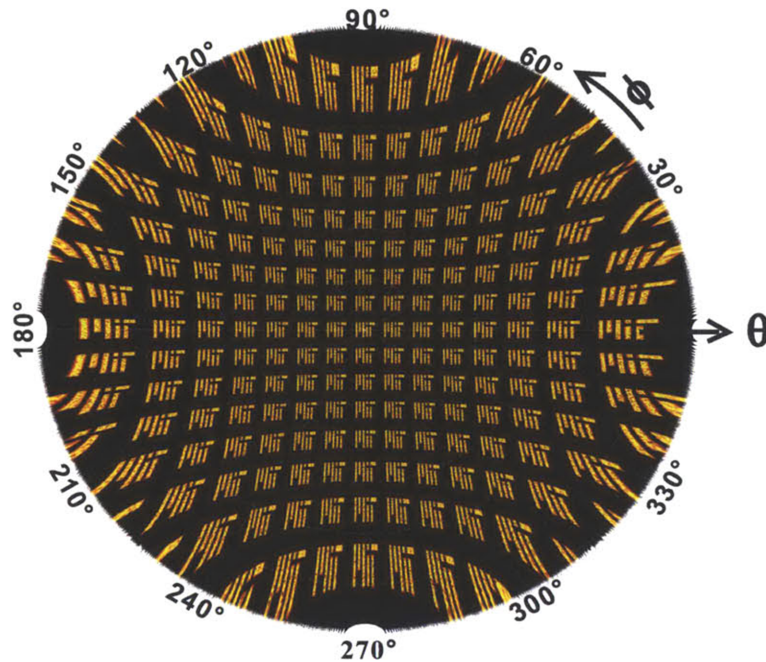

Figure 4-8 The simulated far field of the "MIT" pattern at a wavelength $\lambda = 1.55\mu m$ while the antenna spacing is $\Delta_x = \Delta_y = 9\mu m > \lambda/2$. The resulting far field shows multiple interference orders.

Figure 4-6 and 4-8 demonstrates that arbitrarily complex images can be generated with large-scale phased arrays by carefully designing the emitting phase of all of the elements while keeping the emission amplitude uniform. The far-field pattern, generated by complex interferences from a large number of antennas, is a holographic image that could find future applications such as truly 3-D displays, optical free space communications, and biomedical sciences.

4.3 Noise Analysis of Large-scale Phased Array

In Section 4.2, we demonstrated arbitrary far-field patterns can be generated with large-scale phased arrays by accurately managing the emitting phase of a large number of antennas. In reality however, it is difficult to have all of the thousands of

antennas emit exactly with the designed phase profile. Especially for optical phased array with much shorter optical wavelength compared to its RF counterpart, it is almost impossible to precisely align all of the emitting phase with the designed values. It is therefore necessary to analyze the performance of large-scale phased arrays under certain phase noise.

In phased arrays, in particular the nanophotonic phased array that will be focused on in this work, the phase noise is generally caused by fabrication imperfections which can be considered as a Gaussian white noise $\epsilon_{mn}$with zero mean $\langle\epsilon_{mn}\rangle = 0$ and a standard deviation σ. The actual resulting far-field pattern under the presence of the phase noise is again given by the Fourier transform in Equation 4.12, with the phase noise added to the ideal phase

$$AF^{ac}(\theta,\phi) = \langle\mathscr{F}(e^{j\epsilon_{mn}} \cdot e^{j\varphi_{mn}})\rangle = \langle\mathscr{F}(e^{j\epsilon_{mn}})\rangle \otimes AF^{id}(\theta,\phi) \quad (4.14)$$

where $AF^{ac}(\theta,\phi)$ stands for the actual far-field pattern with noise while $AF^{id}(\theta,\phi)$ is the ideal pattern. '$\otimes$'is the convolution operator. Note that the expectation value (denoted by the angle brackets) is used here, meaning that the average value is taken for the stochastic variables and functions. The discrete Fourier transform of phase noise is given by

$$\langle\mathscr{F}(e^{j\epsilon_{mn}})\rangle = \sum_{m}\sum_{n}\langle e^{j\epsilon_{mn}}\rangle \cdot e^{j(x_m u + y_n v)} \quad (4.15)$$

And the expectation value in Equation 4.15 is by definition calculated as

$$\langle e^{j\epsilon_{mn}}\rangle = \int_{-\infty}^{+\infty} e^{j\epsilon} \cdot \frac{1}{\sqrt{2\pi}\sigma} e^{-\frac{\epsilon^2}{2\sigma^2}} d\epsilon = e^{-\sigma^2/2} \quad (4.16)$$

Substituting Equation 4.16 into Equation 4.15 and then into Equation 4.14 yields

$$AF^{ac}(\theta, \phi) = e^{-\sigma^2/2} \cdot AF^{id}(\theta, \phi) \tag{4.17}$$

The significance of Equation 4.17 lies in that it shows the shape of the far-field array factor pattern is preserved under the white noise, while its amplitude is reduced by a factor of $e^{-\sigma^2/2}$ due to the presence of the phase noise.

To validate the above noise analysis, a Gaussian phase noise with various noise levels, *i.e.* the standard deviation σ, is added to the 64×64 phased array whose phase φ_{mn} is set to generate the MIT-logo "MIT", then the far-field pattern $AF(\theta, \phi)$ is simulated. Figure 4-9 shows the far-field pattern with different phase noise levels, $\sigma = 0$ in Fig. 4-9(a), $\sigma = \pi/16$ in Fig. 4-9(b), $\sigma = \pi/8$ in Fig. 4-9(c), and $\sigma = \pi/4$ in Fig. 4-9(d). It is seen that in all cases, as the phase noise level increases, the shape of the desired pattern remains, as predicted by Equation 4.17; but its signal-to-noise ratio (SNR) drops, compared to the unperturbed pattern in Fig. 4-9(a). The rising background noise comes from the lost power in the desired pattern area since the ideal interference conditions designed to generate the desired pattern are no longer completely satisfied under the presence of the phase noise. We therefore define a signal-to-noise ratio (SNR) of the far-field pattern as

$$SNR = \frac{|\langle AF^{ac} \rangle|^2}{|AF^{id}|^2 - |\langle AF^{ac} \rangle|^2} = \frac{e^{-\sigma^2}}{1 - e^{-\sigma^2}} \tag{4.18}$$

where Equation 4.17 is applied to get the final result. Figure 4-10 shows the SNR of the far-field radiation pattern under different phase noise levels σ. The red dots represent the simulated SNR, calculated from the simulated far-field pattern under different noise level σ. The blue line corresponds to the analytical SNR derived in Equation 4.18. The simulation agrees well with the analytical result, which again validates our noise analysis.

It is noted that even with a considerably large phase noise ($\sigma = \pi/4$) in Fig. 4-

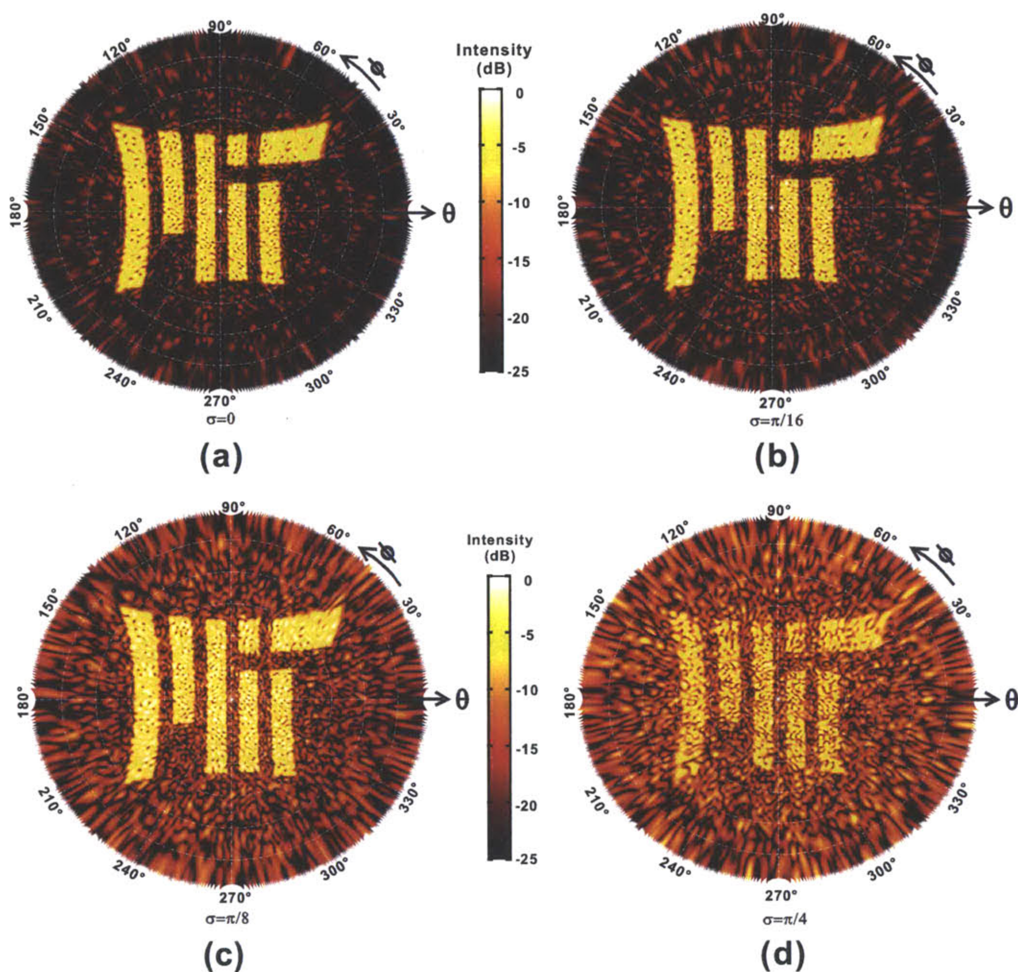

Figure 4-9 The simulated far-field patterns with different phase noise levels, simulated by adding Gaussian phase noise ϵ_{mn} with standard deviations of (a) $\sigma = 0$ (no phase noise), (b) $\sigma = \pi/16$, (c) $\sigma = \pi/8$, and (d) $\sigma = \pi/4$ to the ideal phase φ_{mn}. The designed pattern is still distinguishable even with a considerably large phase noise level $\sigma = \pi/4$, while the background noise rises as the standard deviation σ of the phase noise gets larger.

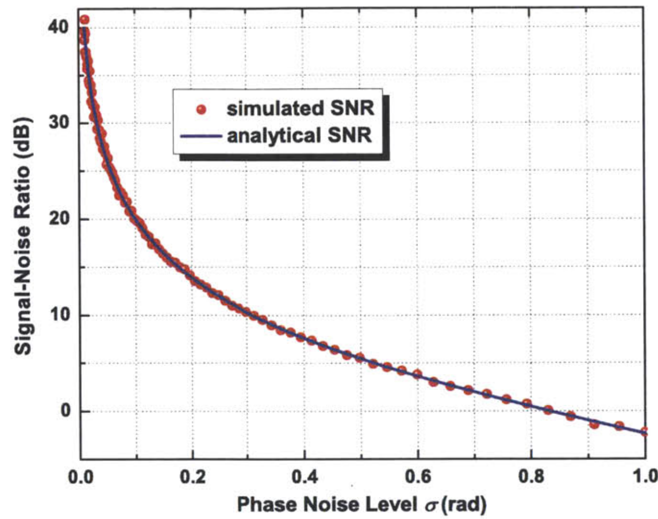

Figure 4-10 The far-field SNR under different near-field phase noise σ. The red dots show the simulated results and the blue line represents the analytical result from Equation 4.18

.

9(d), the designed pattern is still distinguishable. Therefore, the phased array shows high tolerance to phase errors, which largely relaxes the stringent accuracy requirements on fabrication, and hence ensures such a large-scale phased array can be reliably produced with moderate fabrication requirements and function properly. Moreover, this high error-tolerance does not compromise when the scale of the array increases. In fact, the more nanoantennas the array has, the more genuine the above analysis is, from statistical considerations. Therefore, there exist no major obstacles to scale up the pixels of the nanophotonic phased array beyond 64×64 to even millions of pixels.

In this chapter, we have seen in simulation that arbitrary and sophisticated far-field radiation patterns can be generated with large-scale phased arrays where a large number of antenna elements are incorporated in the array. Moreover, the large-scale phased array is highly tolerant of white phase noises caused by fabrication, which ensures the large-scale phased array can actually be made and function as designed. In the next chapter, we will show the physical design and experimental results of the nanophotonic phased array based on the silicon photonic platform

using the state-of-the-art CMOS process.

CHAPTER 5

Large-scale Passive Phased Array

In Chapter 4, it has been shown that arbitrarily complex far-field patterns can be generated with large-scale phased arrays containing a large number of antennas. Although large-scale radio-frequency (RF) phased arrays have been developed and used for decades, it is extremely expensive and cumbersome to make large-scale RF phased arrays [45]. The optical phased array however, where the individual antenna size can be reduced to μm-scale because of the much shorter optical wavelength, has the unprecedented advantage to integrate a large number of optical antennas within a small footprint when combined with the silicon photonic technology to make use of the state-of-the-art complementary metaloxidesemiconductor (CMOS) processing techniques to enable large-scale yet low-cost photonic integration. In this chapter, we will demonstrate a large-scale phased array in silicon photonic platform from the device design to system architecture, and finally an experimentally demonstrated 64×64 nanophotonic phased array system in which the optical power is balanced and phase aligned in all 4,096 optical antennas to form a pre-designed complex far-field radiation pattern.

5.1 Device Design: Dielectric Nanoantenna

In phased array, it is essential to make the individual antenna as small as possible so that more and more antenna elements can be integrated within a small footprint to form a large-scale phased array. In this sense, phased array in optical regime is of particular interest in that it operates at a much shooter wavelength compared to its RF counterparts which significantly reduces the light-matter interaction length and hence enables efficient optical nanoantennas with a sub-μm size.

Optical nanoantennas down to sub-wavelength size has been extensively studied previously [46]-[51], including the aperture antenna [49], the resonant optical antenna [50], the optical Yagi-Uda antenna [51], *etc.* Most of them use metals such as gold as the antenna material to take advantage of the strong metal-light interaction attributed to metal's high refractive index. Though compact in size and efficient in optical emission, metallic antenna is not compatible with standard CMOS process and is therefore hard to be integrated in large-scale phased arrays. As a result, it is desirable to develop compact and efficient dielectric optical antennas. Dielectric optical antennas especially in silicon have also been well researched recently [52]-[54], mainly for the application of the waveguide-fiber vertical coupler which has a large device footprint of tens of micrometers and is thus not suitable for large-scale phased arrays in which compact antennas are preferred to reduce the high-order interference patterns. To this end, a silicon-based compact dielectric nanoantenna is developed in this work which has a small device footprint and efficient optical emission.

Dielectric grating-based optical nanoantenna is used in this work, as shown in Fig. 5-1. The optical waveguide is widened at the end and a circular grating with period Λ is formed to scatter light propagating in the waveguide to all directions. For the phased array application, more upward emission along $+z$-direction is desirable, which is the most important design goal for the optical antenna in this work. However, in conventional optical emitter or vertical coupler designs, the up-emission efficiency is usually compromised by two effects. First, significant

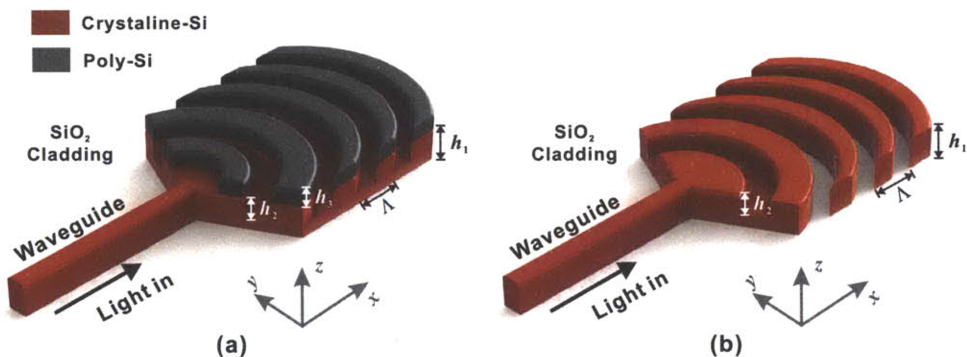

Figure 5-1 Two types of optical nanoantenna design considered in this work: (a) optical nanoantenna design with a layer of polycrystalline silicon and a shallow etch available in process, and (b) optical nanoantenna design with only a shallow etch available in process.

back-reflection normally accompanies with the optical emitters which not only reduces the up-emission efficiency but will also interfere with other signals in the phased array system. Second, the downward emission is usually comparable to the upward emission due to the up-down symmetry of the dielectric antenna. In the following of the section, we will focus on these two problems to achieve a high-efficiency optical nanoantenna.

5.1.1 Minimizing the Back-reflection

In grating based optical antennas or vertical couplers, as shown in Fig. 5-2, light propagating in x-direction in the grating is diffracted into many diffraction orders. The direction of the diffracted beam is given by the phase matching condition

$$\beta_x + l \cdot k_\Lambda = k_x^{(l)} \quad (l \in \mathbb{Z}) \tag{5.1}$$

where β_x is the light propagation constant in grating, $k_\Lambda = 2\pi/\Lambda$ is the grating vector, and l is an integer denoting the diffraction order. $k_x^{(l)}$ is the x-component of the wave vector ($\mathbf{k}^{(l)}$) of the lth diffraction order, where $|k_x^{(l)}| = 2\pi/n_{\mathrm{SiO_2}}$ when the

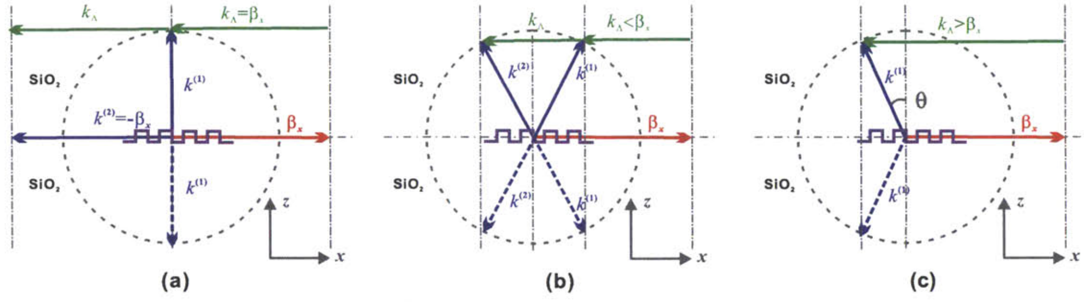

Figure 5-2 Three diffraction conditions with different grating period Λ with regard to the light effective wavelength in the grating λ_{eff}: (a) second-order grating where $\Lambda = \lambda_{\text{eff}}$, (b) $\Lambda > \lambda_{\text{eff}}$, and (c) $\Lambda < \lambda_{\text{eff}}$. The upward emission is maximized in (c).

diffracted light is in the SiO_2 cladding and $|k_x^{(l)}| = \beta_x$ when it falls in the grating (back-reflection).

In vertical couplers, second-order diffraction grating, where the grating period Λ equals the effective wavelength of light in the grating, *i.e.* $\Lambda = \lambda_{\text{eff}} = 2\pi/\beta_x$, is generally used in order to have vertical emissions. However, this exact match of grating period to effective wavelength also gives rise to the strong resonant back-reflection as shown in Fig. 5-2(a), since the back-reflected beam also satisfies the phase matching condition as the 2nd-order diffraction: $k_x^{(2)} = -\beta_x = \beta_x - 2k_\Lambda$. Therefore the grating period can be detuned from λ_{eff} to suppress the back-reflection. However, in the case $\Lambda > \lambda_{\text{eff}}$ as shown in Fig. 5-2(b), second-order diffraction also exists causing two emission directions from one emitter. In order to have a unidirectional emission, the grating period needs to be smaller than the effective wavelength:

$$\frac{\lambda_{\text{eff}}}{2} < \Lambda < \lambda_{\text{eff}} \tag{5.2}$$

so that only one diffraction order occurs, as shown in Fig. 5-2(c). Note that the grating period also has a lower bound since strong Bragg reflection happens when $\Lambda = \lambda_{\text{eff}}/2$ and no diffraction exists when $\Lambda < \lambda_{\text{eff}}/2$. The grating period detuning

also results in a non-vertical diffraction with an angle θ from vertical determine by

$$\sin\theta = \frac{\beta_x - k_\Lambda}{k_1} = \frac{\dfrac{n_{\text{eff}}}{\lambda_0} - \dfrac{1}{\Lambda}}{\dfrac{n_{\text{SiO}_2}}{\lambda_0}} \tag{5.3}$$

where n_{eff} is effective index of light in the grating, λ_0 is the vacuum wavelength of the light, and $\theta > 0$ means the emission is toward the wave propagation direction. The effective index n_{eff} of light in the grating can be determined by the perturbation theory by replacing the periodic grating layer with an artificial layer whose refractive index n_g is given by

$$n_g^2 = D \cdot n_1^2 + (1 - D) \cdot n_2^2 \tag{5.4}$$

where D is the duty cycle of the grating, n_1 and n_2 are the refractive indices of the core layer and the cladding layer, which in this work are Si and SiO_2 respectively. Furthermore, since the light is weakly confined in y-direction due to the widened waveguide region with span of several wavelengths, the grating can be treated simply as a multi-layer dielectric slab to calculate the effective index n_{eff}, as shown in Fig. 5-3(a). Figure 5-3(a) and (b) simulate the optical emission angle due to the grating period detuning for the two different antenna structures shown in Fig. 5-1. In the process with 0.1μm poly-Si layer, any shallow etch depth h_2 can be applied, as shown in Fig. 5-3(b); while in the process with only a shallow etch available, the shallow etch depth has to be larger than 0.16μm to ensure unidirectional emission as indicated by the shaded region in Fig. 5-3(c).

5.1.2 Minimizing the Down-emission

Downward emission is another source that caused the reduced up-emission efficiency in optical antennas. It is also the major cause of the interferential noise in the

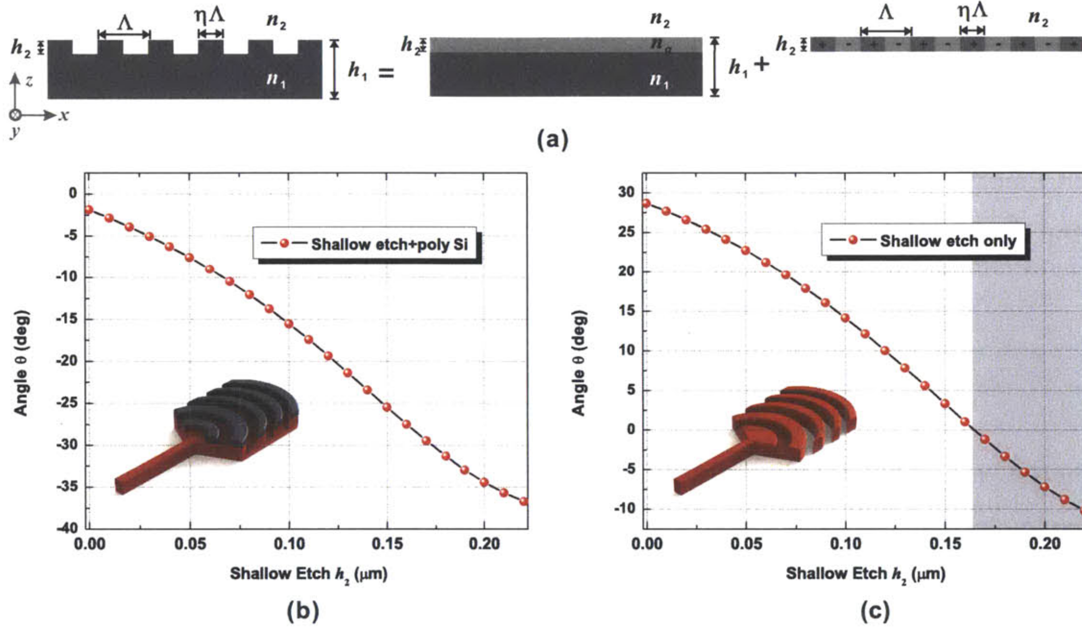

Figure 5-3 (a) The perturbation theory applied to the grating where the grating layer is replaced by an artificial material so that the grating can be considered as a multi-layer slab waveguide. The simulated optical emission angle due to grating period detuning for (b) the structure in Fig.5-1(a) where a poly-Si layer of 0.1μm and a shallow etch with different depth h_2 are available, and (c) for the structure in Fig.5-1(b) where only a shallow etch with depth h_2 is available. The shaded area highlights the unidirectional emission region ($\theta < 0$). A grating duty cycle $D = 0.4$ is assumed in the simulation as will be used later in the fabrication.

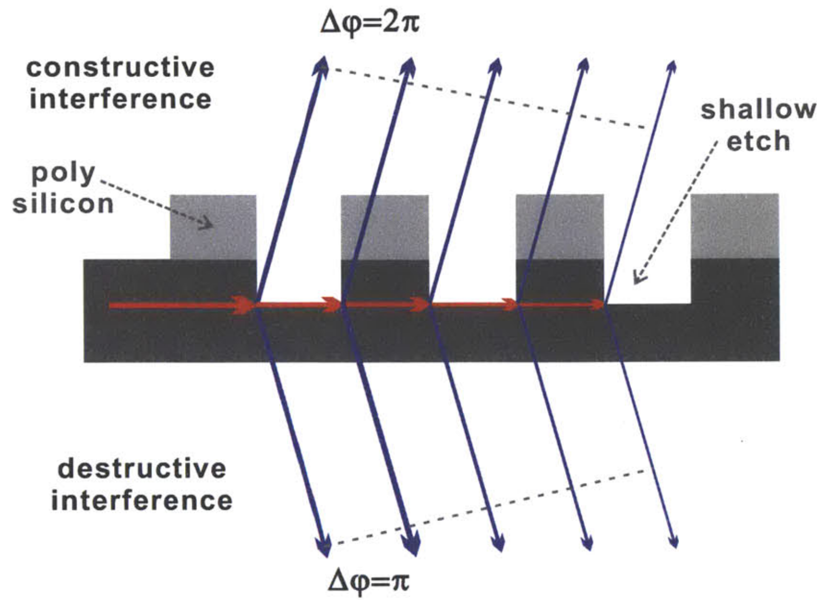

Figure 5-4 More up-emission is achieved by breaking down the symmetry of the grating structure so that the up-emission is enhanced by constructive interference while the down-emission experiences destructive interference.

far-field pattern as will be discussed later in Section 5.4. It is therefore necessary to reduce the down-emission in the optical nanoantenna.

As shown in Fig. 5-2(c), even in the case of 'unidirectional'emission, because the phase matching condition (Equation 5.2) is satisfied in up- and down-direction at the same time due to the symmetry of the structure, the down-emission and the up-emission always coexist and have the same emitting efficiency. Therefore, in order to achieve an unbalanced emission, *i.e.* to have more power emitting up, the up-down symmetry of the structure must be broken down. Figure 5-4 shows the principle of achieving unbalanced emission in such an asymmetric grating structure [55]. Each grating groove can be considered as a scattering center that emits light to all directions. Due to the asymmetry of the grating structure, the up emitted light travels through a different optical path from the down emitted light. At certain optimized design, the up-traveling light experiences constructive interference because the optical phase difference between emissions from adjacent scattering centers is 2π. On the contrary, the down-traveling wave has destructive

interference because of the π phase difference between neighboring light rays. As a result, the down-emission is largely suppressed in this way. This asymmetric structure can be provided by the shallow silicon etch and/or the poly-silicon overgrowth which is available in standard CMOS processes, as shown in Fig. 5-4.

Based on the aforementioned methods to reduce the reflection and down-emission, two nanoantenna designs, which will be referred to as DS-1 and DS-2 hereafter, are proposed as shown in Fig. 5-1(a) and Fig. 5-1(b) respectively. In DS-1, the optical nanoantenna is formed with a shallow silicon etch ($h_2 = 0.1\mu m$) in a silicon-on-insulator (SOI) with 0.22μm device layer ($h_2 = 0.22\mu m$), and a layer ($h_3 = 0.1\mu m$) of polycrystalline silicon grating deposited on top of the crystalline silicon. Grating period $\Lambda = 0.52\mu m$ and duty cyle $D = 0.4$ is assumed to satisfy Equation 5.2 to ensure a single diffraction order. In DS-2, the optical nanoantenna is formed with a shallow silicon etch applied only to the first grating groove and a full silicon etch to define the waveguide. The grating period is 0.72μm with a duty cycle $D = 0.4$. The nanoantennas have a compact size of 2.2μm×2.8μm in DS-1 and 3.0μm×2.8μm in DS-2 with only 5 grating periods in both cases. Note that the layer thicknesses (poly-Si, shallow etch, and waveguide height) used in these designs are not completely optimized, limited by the available fabrication processes. Figure 5-5 shows the optical emission efficiency in all the directions, calculated from a rigorous 3-dimensional (3D) finite-difference in time-domain (FDTD) method. It is seen an up-emission efficiency of 63% and 51% at wavelength $\lambda_0 = 1.55\mu m$ is achieved for the proposed nanoantennas. In both cases, the reflection is greatly reduced and the down-emission is suppressed. The extinction ratio between the up-emission and down-emission is better in DS-1 (3.2) than in DS-2 (1.5), because the overlaid poly-silicon layer increases the asymmetry of the structure so that the constructive-destructive interference condition illustrated in Fig. 5-4 is better satisfied. Another thing to notice is that in both cases, the bandwidth of the optical emission is extremely wide with a 3-dB bandwidth more than 200nm. This is a natural outcome of the fact that the optical bandwidth is reversely proportional to the grating length which is very short here. The efficient and broadband emitters

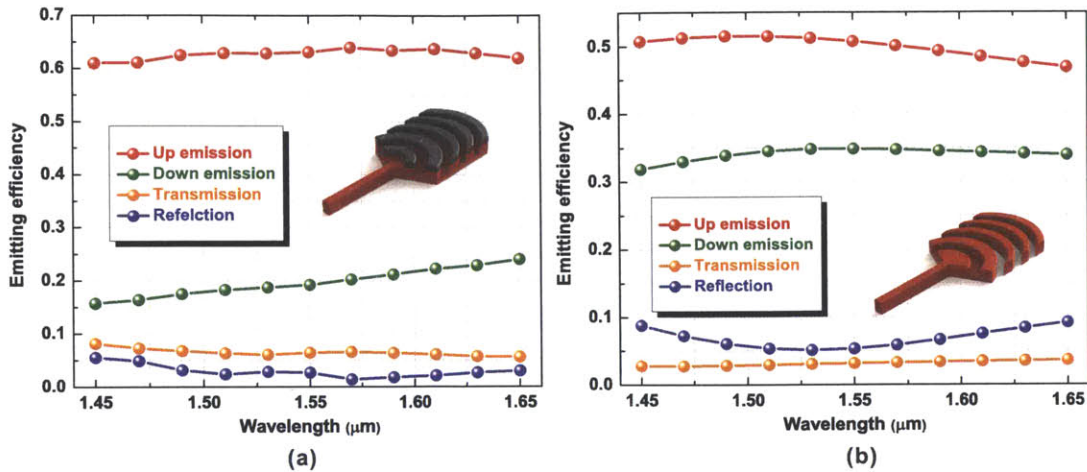

Figure 5-5 The optical emission efficiency of the nanoantennas based on (a) DS-1 where the structure is formed by a shallow etch and a poly-Si layer, and (b) DS-2 where the structure is formed by a shallow etch only. In both cases, back-reflection is greatly suppressed and unbalanced up-down emission is achieved.

could find potential applications such as broadband vertical couplers with further optical field engineering to match the optical emission with the optical fiber mode.

Using the rigorous 3-D FDTD simulation, the near-field optical emission of the proposed nanoantennas is simulated, as shown in Fig. 5-6(a) and (b). It is seen that more power is emitting up especially in DS-1 as indicated by the emission efficiency in Fig. 5-5. It is also noted that, the up-emission (shown by the top surfaces) is more spread out in Fig. 5-6(a), compared to Fig. 5-6(b) where several separated side-lobes are seen in the near field. This is possibly because the scattering by a single scattering center (each grating tooth) is weaker in Fig. 5-6(a) which is also confirmed by the slightly higher transmission as shown in Fig. 5-5(a) compared to Fig. 5-5(b). As shown in Fig. 5-6(c) and (d), the far-field emission pattern of the nanoantenna is also calculated for both designs using the near-to-far-field transformation [56] where the far-field pattern is a simple Fourier transform of the near-field emission shown in Fig. 5-6(a) and (b). The far field of DS-1 is more confined, a consequence of the more spread near field emission as shown in Fig. 5-6(a) considering the Fourier transform relation between the near and far field. Similarly, the far field of DS-2 has more side lobes, also an outcome of the multiple lobes in the near field as

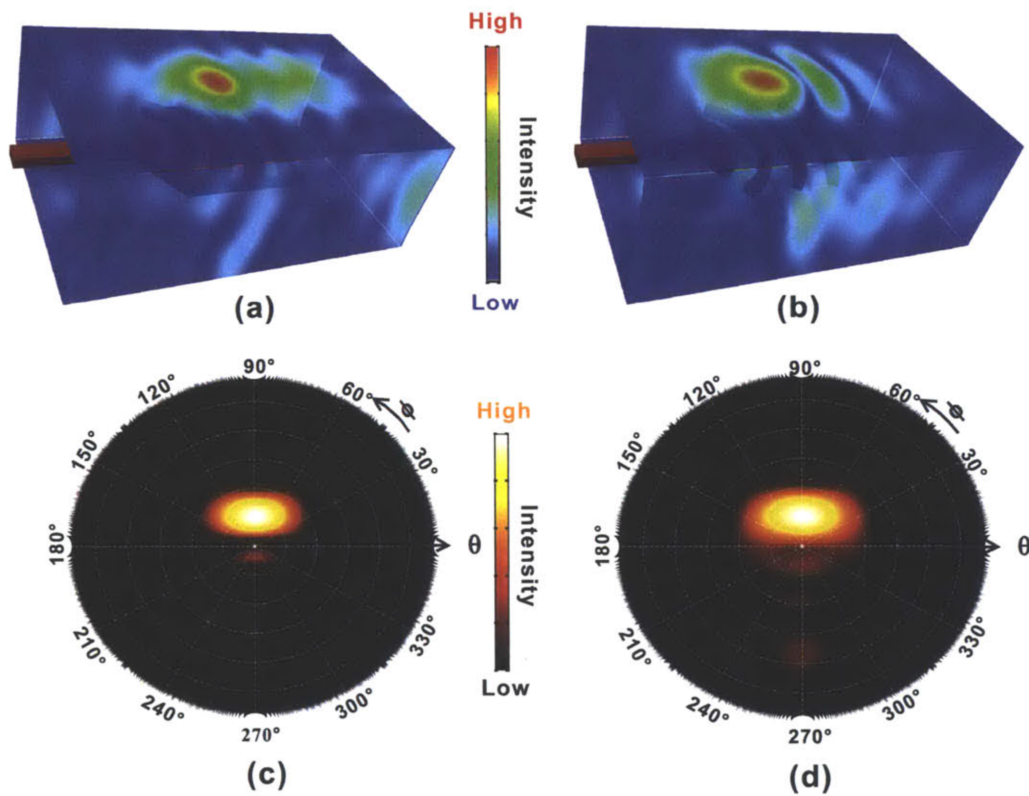

Figure 5-6 Simulated near-field optical emission of (a) DS-1 where the nanoantenna structure is formed by a shallow etch and a poly-Si layer, and (b) DS-2 where the nanoantenna structure formed by a shallow etch only. The simulations are carried out with a rigorous 3-D FDTD tool. Simulated far-field pattern of a single optical nanoantenna of (c) DS-1, and (d) DS-2. The far-field patterns are calculated with the near-to-far-field transformation.

shown in Fig. 5-6(b).

As seen in Fig. 5-5 and Fig. 5-6, the design goals of the optical nanoantenna - efficient up-emission in a compact size with back-reflection and down-emission suppressed - are all achieved in the proposed designs. The performances of the optical nanoantennas can be further improved provided that more flexibility is available in the fabrication process, such as the thickness and position of polycrystalline silicon, number and depth of shallow etches, *etc.* Limited by the fabrication processes available in the CMOS foundry in which the devices will be made, DS-2 is chosen as the optical nanoantenna for our large-scale nanophotonic phased array, though DS-1 shows better performances in simulation. The optical nanoantenna is fabricated in a 300-mm CMOS foundry with a 65-nm technology node, using SOI wafers with a 0.22μm top silicon layer and 2μm buried oxide (BOX) as the under cladding. A shallow silicon etch with a target depth of 0.1μm is first performed with hydrogen bromide (HBr) timed dry etch to form the first grating groove which provides the up-down asymmetry of the optical nanoantenna. A full silicon etch is then carried out to define the rest of the structure with the BOX layer as the etch stop by taking advantage of the high selectivity (>100:1) of HBr in etching Si over SiO_2. Then a layer of 3.6μm tetraethyl orthosilicate (TEOS) SiO_2 is deposited on top of silicon as the over-cladding, followed by a chemical mechanical polishing (CMP) step to planarize the top surface to avoid additional phase errors due to surface corrugation which is essential for the phased array applications. Figure 5-7 shows a scanning-electron-micrograph(SEM) of the fabricated optical nanoantenna. The fabricated device has a similar dimension as in the design (DS-2 as described earlier) which confirms the precision of the fabrication process. Two-step silicon etch including a shallow etch and a full etch is seen in the SEM. The SEM is taken after the over-clad SiO_2 is removed by a controlled buffered oxide etch (BOE) in hydrofluoric acid (HF).

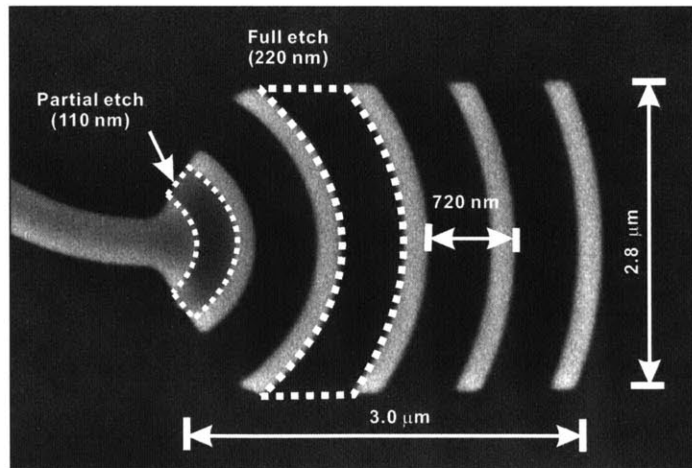

Figure 5-7 Scanning-electron-micrograph (SEM) of the fabricated optical nanoantenna. Two etching steps, a shallow silicon etch and a full silicon etch, are observed.

5.2 System Design: Power Balance and Phase Alignment

The key device of the optical phased array, *i.e.* the optical nanoantenna, has been studied and developed in Section 5.1. However, to integrate thousands of or even millions of such nanoantennas in a small footprint with all of the nanoantennas balanced in power and aligned in phase to generate a desired complex far-field pattern is extremely challenging. To this end, this section will discuss from a system level (1) how to distribute the optical power so that the large-scale phased array can emit with a certain amplitude pattern, and (2) how to manage the optical phase so that each nanoantenna can emit with the designed phase pattern such as the one shown in Fig. 4-6(a) and (b).

5.2.1 Optical Power Distribution

Optical phased arrays have been researched for decades on many platforms [57]-[62] including the recent studies with integrated photonics [63]-[65]. However, almost all of the demonstrations to date employed the same optical power distribu-

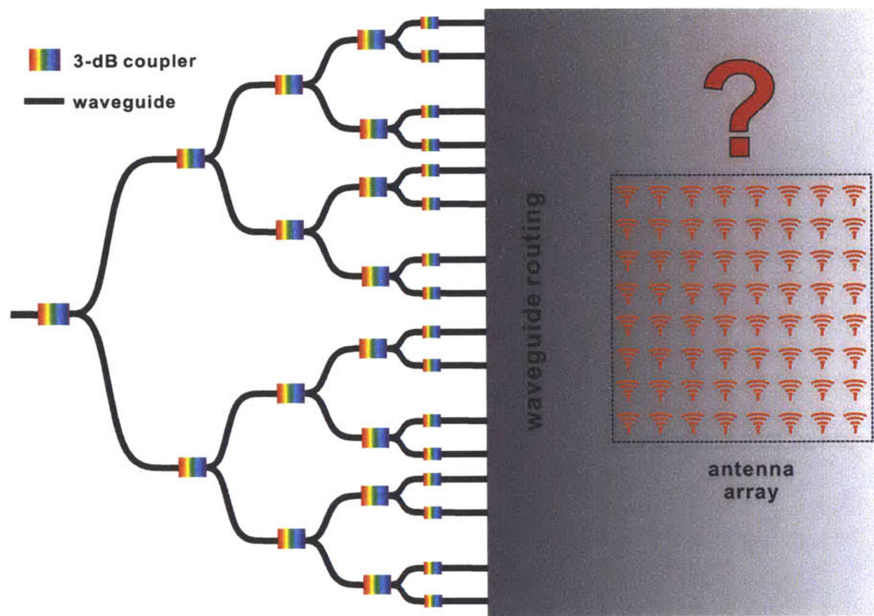

Figure 5-8 Schematic of the conventional optical phased array architecture. Many 3-dB couplers are cascaded to equally distribute optical power into a large number of waveguides, and the waveguides are routed (if possible) to feed the antenna array.

tion architecture as shown in Fig. 5-8. A large number 3-dB couplers are cascaded to equally divide optical power from an input waveguide into $2^l (l \in \mathbb{N})$ waveguides, followed by sophisticated waveguide routing to feed individual optical antennas. Though this architecture is exclusively used in previous demonstrations, there exist several major drawbacks as discussed in the following:

1. Though most optical phased arrays require uniform optical emission from all the antennas, the optical emission needs to follow certain nonuniform amplitude pattern in some cases as will be discussed in Chapter 6. However, it is impossible to achieve arbitrary amplitude patterns other than uniform in this conventional architecture.

2. The cascaded 3-dB coupler architecture makes the system cumbersome and vulnerable. A large number of 3-dB couplers are required for large-scale phased arrays, wasting a lot of valuable chip space and compromising the significance of on-chip integration. Moreover, since the same 3-dB couplers

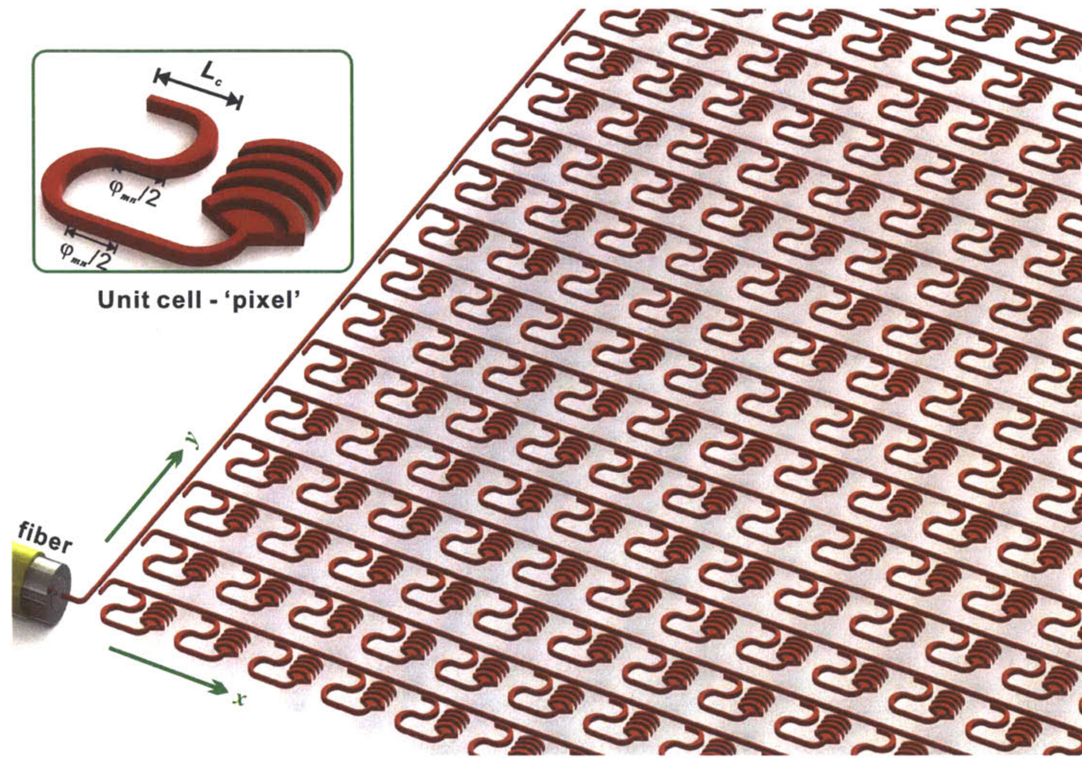

Figure 5-9 Schematic of the proposed system architecture of the large-scale nanophotonic phased array. The optical power from an input optical fiber is divided into each unit cells, or 'pixels', through a bus waveguide and many row waveguides. The inset shows the schematic of a pixel.

are cascaded many times, slight design and fabrication deviations will aggregate and lead to significant performance degradation. Therefore, it is extremely hard to obtain uniform emission in such an architecture especially when it goes to large scale.

3. Most importantly, it is extremely difficult, if possible at all, to route the large number of waveguides to feed all of the densely packed nanoantennas.

For these very reasons, especially the waveguide routing difficulty, all of the integrated optical phased arrays to date are limited to 1-D or small-scale 2-D demonstrations with no more than 16 antennas. Therefore, the conventionally used architecture is inherently not suitable for optical phased arrays.

In this work, we propose a completely different optical phased array architecture that is suitable for large-scale optical phased arrays, as shown in Fig. 5-9. The optical power is coupled from an input fiber to a silicon bus waveguide. The optical power in the bus waveguide is then divided into M row waveguides through M bus-to-row directional couplers. Finally the optical power in each row waveguide is coupled into N unit cells, or 'pixels ', through N row-to-unit directional couplers so that the whole $M \times N$ array is optically fed. Since the coupling ratio of the directional coupler can be arbitrarily adjusted from 0 to 1, it is possible to achieve any designed amplitude pattern for the phased array. Suppose a certain amplitude pattern $|w_{mn}|$ is required, the coupling ratio c_m of the mth bus-to-row coupler is

$$c_m = \frac{\sum_{j=1}^{N} |w_{mn}^2|}{\sum_{i \geq m}^{M} \sum_{j=1}^{N} |w_{mn}^2|} \tag{5.5}$$

and the coupling ratio of the nth row-to-unit coupler in the mth row is

$$c_{mn} = \frac{|w_{mn}^2|}{\sum_{j \geq n}^{N} |w_{mn}^2|} \tag{5.6}$$

Through Equations 5.5 and 5.6, the directional couplers can be configured to generate any amplitude pattern. In this chapter, we will focus on uniform emission where each pixel is equally fed. Figure 5-10 illustrates the optical power in the bus waveguide with a width of 0.46μm is equally distributed into M row waveguides, by properly adjusting the length $L_c(m)$ of the directional coupler. The bus-to-row directional coupler is composed of a straight waveguide coupling region and a 90°-bend with an outer radius of 3μm and inner radius of 2.54μm. It is noted that the last part of the optical power is intentionally discarded through a gradually tapered waveguide to avoid the need of 100% coupling ratio for the last row which

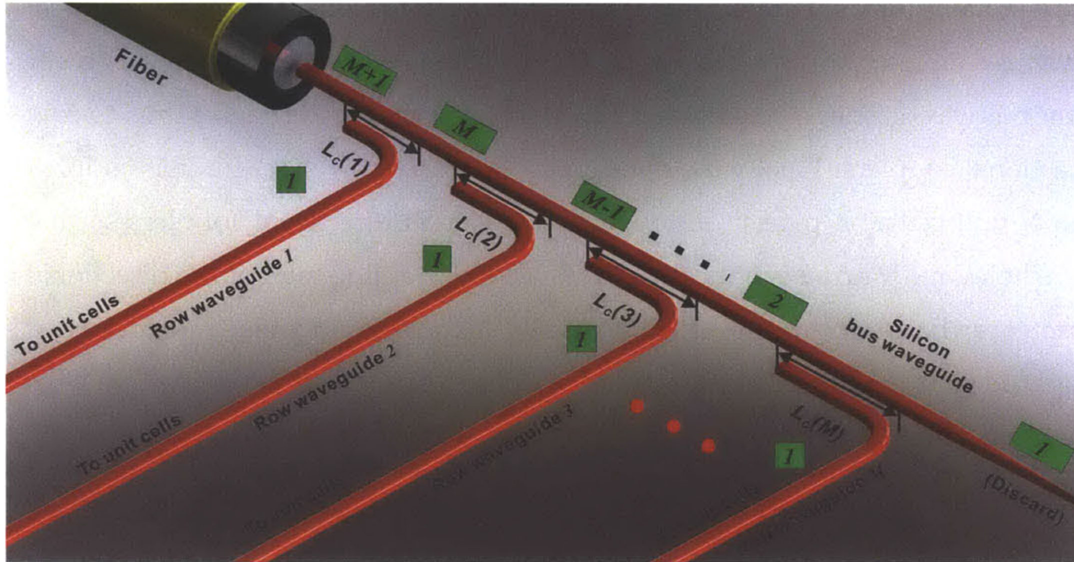

Figure 5-10 Power distribution network where the optical power in the bus waveguide is equally coupled to M row waveguides. The green boxes indicate the optical power in each segment of the network.

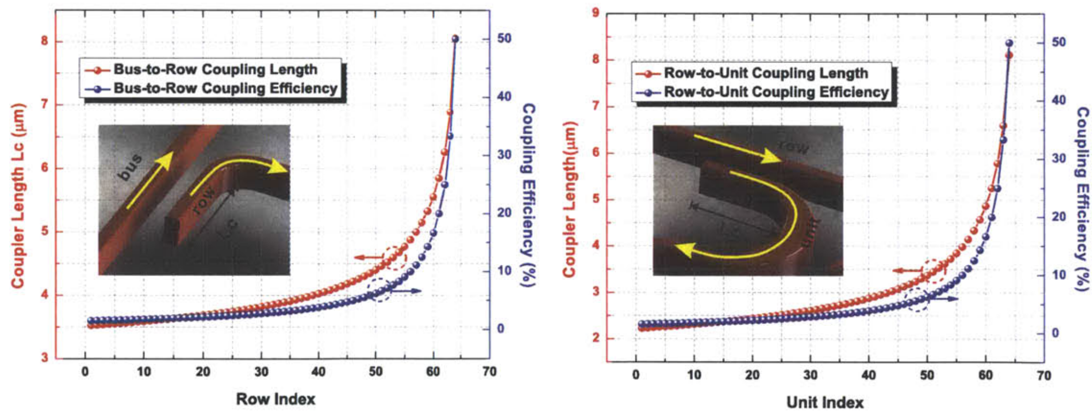

Figure 5-11 (a) The bus-to-row and (b) the row-to-unit coupler lengths in order to equally distribute the optical power to all the 4,096 pixels in a 64×64 nanophotonic phased array with the proposed architecture. The coupler becomes longer and longer as the light propagates along the waveguide.

would otherwise require an overlong coupler length and enlarges the pixel size. The row-to-unit coupler is managed in the same way, except that the bend used there is an adiabatic bend which has a circular outer edge with 2.0μm radius and an elliptical inner edge with 1.0μm x-axis and 1.54μm y-axis to make an adiabatic bend with wider center part, as shown in the inset of Fig. 5-9. The adiabatic bend is for the future implementation of active phase control as will be discussed in Chapter 6. The percentage loss α_L due to the discarded optical power is

$$\alpha_L = \frac{1 + \frac{N}{N+1}}{M + 1} \tag{5.7}$$

which is negligible in large-scale arrays when $M \gg 1, N \gg 1$. For instance, the discarded optical power loss is only 3% in a 64×64 array. Although the coupling ratio can also be adjusted by the coupling gap, it is more controllable to change the length $L_c(m)$ since the coupling ratio is less sensitive to the length variation.

Using a rigorous 3-D FDTD simulation, the coupling ratio at different coupler lengths L_c is calculated for the bus-to-row and the row-to-unit directional couplers, and the coupler length corresponding to a certain coupling ratio can be further calculated. Figure 5-11 shows the bus-to-row and the row-to-unit coupler lengths in a 64×64 nanophotonic phased array in order to achieve uniform emission. In Fig. 5-11(a), the bus-to-row coupler length L_c varies from 3.53μm with a coupling ratio 1.53% in the first coupler to 8.05μm with a coupling ratio 50% in the last coupler. And in Fig. 5-11(b), the row-to-unit coupler length L_c varies from 2.23μm with a coupling ratio 1.53% in the first coupler to 8.12μm with a coupling ratio 50% in the last coupler. The coupler gets longer and longer as the light propagates along the waveguide since the coupling ratio increases. The longest coupler length 8.2μm still fits into the pixel which measures 9μm×9μm.

5.2.2 Optical Phase Management

In Section 5.2.1, we have proposed a novel phased array architecture that is capable of arbitrarily distributing optical power to a large-scale phased array. The remaining task is to manipulate the optical phase of each nanoantenna so that it is aligned with the designed phase patterns such as those in Fig. 4-6 to generate the desired far-field patterns. This is realized by placing an optical-delay-line-based phase-adjustment part before each emitter. In the proposed phased array structure, the phase adjustment part can be either placed in-line in the row waveguide before light is coupled into each pixel, or inserted in each pixel after light coupled into the pixel as shown in Fig. 5-9. The former approach, though has some advantages such as being able to realize continuous beam steering in active phased arrays as will be discussed in Chapter 6, its main drawback is that the phase error in each phase-adjustment part aggregates as the light propagates along the waveguide, producing correlated non-white phase noise that invalidates the previous noise analysis in Section 4.3 and would largely degrade the image quality in the far field. Therefore, the latter approach, where the phase-adjustment part is directly inserted in each pixel, is used in this work.

Figure 5-12(a) illustrates a schematic of the pixel with the phase-adjustment part. The phase-adjustment part contains two identical optical delay lines placed in parallel in x-direction, each of which provides an optical phase shift of $\varphi_{mn}/2$ so that the nanoantenna will emit with a desired relative phase φ_{mn}. The phase delay is divided into two identical segments to make the final position of the nanoantenna independent on the emitting phase φ_{mn} needed in the pixel so as to have the nanoantennas placed in a periodic grid that is required in phased array. The pixel also contains a row-to-unit directional coupler with two adiabatic 180°-bends for future implementation of integrated thermo-optic heaters for active phased arrays as will be discussed in Chapter 6, as well as the proposed compact nanoantenna. The dimensions of the directional coupler and the nanoantennas were previously defined in Section 5.1.2 and Section 5.2.2 respectively. Figure 5-12(b) shows an SEM

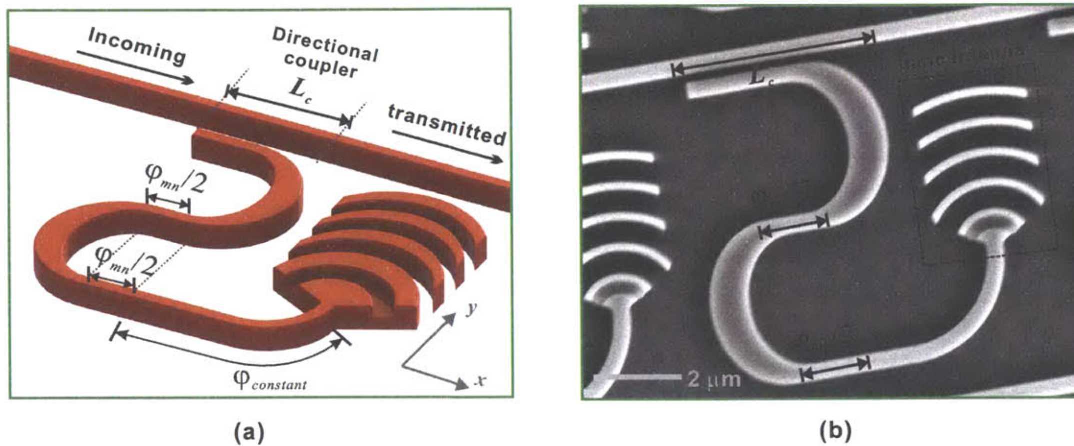

(a) (b)

Figure 5-12 (a) Schematic of the pixel. (b) SEM of the fabricated pixel. Each pixel contains a directional coupler whose length is carefully adjusted to deliver the desired amount of optical power to the pixel, and two separate optical delay lines to have the nanoantenna emit with the desired relative phase φ_{mn}.

of the fabricated pixel in a 64×64 nanophotonic phased arrays. It is seen the design is well reproduced.

5.3 The Fabricated 64×64 Nanophotonic Phased Array

The proposed large-scale nanophotonic phased array is fabricated in a 300-mm CMOS foundry at 65-nm technology node using 193-nm optical immersion lithography. The fabrication details were previously discussed in Section 5.1.2. Figure 5-13 (a) shows an optical image of a portion of the fabricated 64 × 64 nanophotonic phased array. The image is taken with the 3.6μm SiO_2 over-cladding on. The grating-based nanoantennas are seen with golden color in the image. Figure 5-13(b) shows an SEM of the same phased array after removing the over-cladding in the BOE. A close-up SEM of the fabricated pixel is also shown in Fig. 5-12(b). The pixel size is 9μm×9μm.

The near field and far field of the large-scale nanophotonic phased array are measured with the setup shown in Fig. 5-14. The fabricated phased array chip is placed on an optical stage with 1.55μm laser side-coupled in through an optical

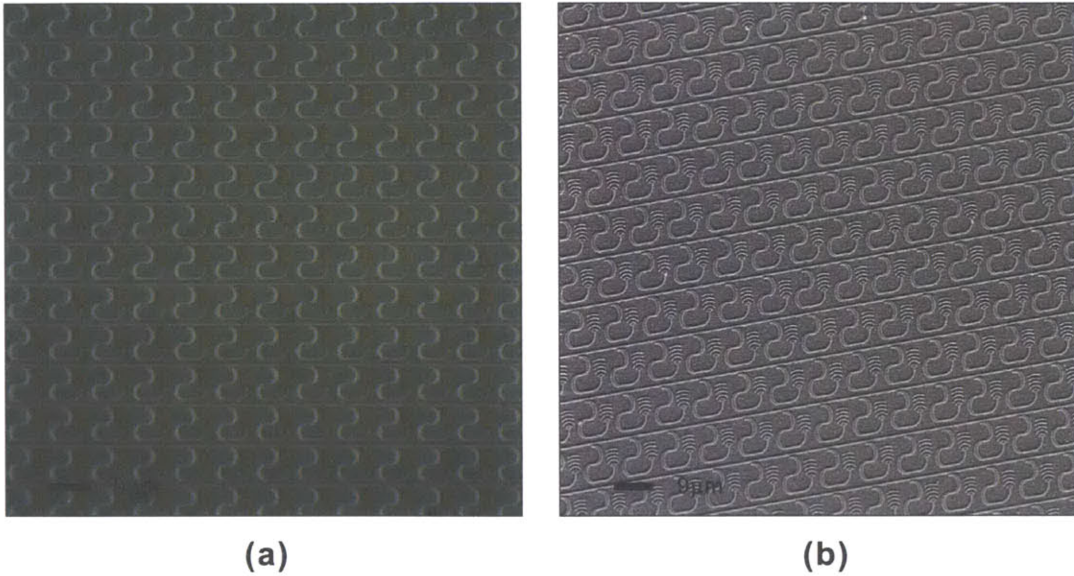

Figure 5-13 (a) Optical image of a portion of the fabricated 64 × 64 nanophotonic phased array, with 3.6μm SiO_2 over-cladding. (b) The SEM image of the same phased array with SiO_2 over-cladding removed in BOE. The pixel size is 9μm×9μm.

fiber. The near-field image is formed by a single-lens imaging system with objective Lens-1 only, as shown by the green rays in Fig. 5-14. Lens-1, which has a focal length of 10mm and a numerical aperture (NA) 0.4, magnifies and projects the near-field emission pattern onto the infrared (IR) charge-coupled-device (CCD). The far-field image is captured by inserting another Lens-2 into the imaging column and adjusting the positions of the two lenses, as shown by the blue rays in Fig. 5-14. The objective Lens-1 now serves as a near-to-far-field converter that focuses all the near-field emission with the same emission angle (**k**-vector) to a single point on its back-focal plane (Fourier plane), so that the far-field pattern is created on the back-focal plane of Lens-1. Lens-2, as a magnification lens, projects the far-field pattern from the back-focal plane to the IR CCD.

Figure 5-15 shows the near-field measurement of a 64×64 nanophotonic phased array designed to emit uniformly across all of the 4,096 nanoantennas. It is seen in Fig. 5-15(a) that uniform emission is achieved across the whole phased array. Note that the fiber is coupled in from the top-left corner of the array, causing extra

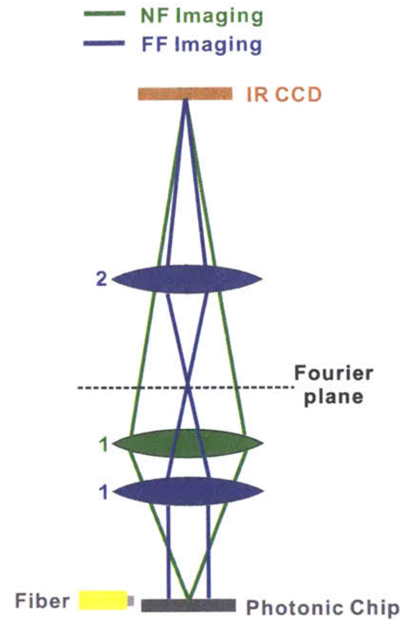

Figure 5-14 A schematic of the near and far field measurement setup. Lens-1 alone is used to image the near field, shown by the green rays. Lens-2 is inserted to capture the far field together with Lens-1, represented by the blue rays.

background noise in that part due to the strong scattering from the fiber-waveguide coupling; but this does not reflect non-uniformity in the array itself and can readily be addressed with a larger separation from the fiber input. Figure 5-5(b) shows a close-up near-field image of the bottom-right corner of the phased array containing 8×8 nanoantennas. It is seen the near-field emission is strong and uniform even at the farthest corner from the input point of the large-scale phased array, an evidence of a robust photonic design and a reliable device fabrication. Figure 5-5(c) shows a quantitive statistical result of the intensity distribution measured from a large number of nanoantennas in the phased array. A Gaussian-shaped intensity distribution is observed with a normalized average intensity $\mu = 0.69$ and standard deviation $\sigma = 0.09$.

Before the far-field measurement results are presented, we would like to review the relation between the near-field emission and the resulting far-field pattern again through the Fourier transform, in order to understand from a mathematical point of view how the far-field pattern is formed and especially how the individual

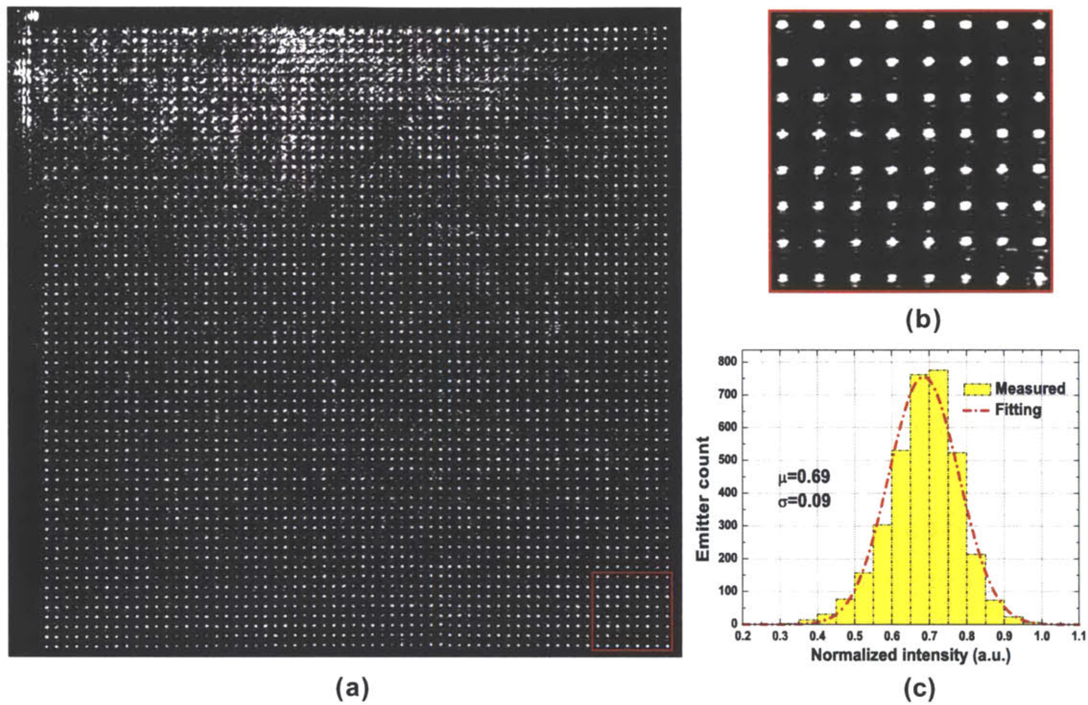

Figure 5-15 (a) The near-field image of the 64 × 64 nanophotonic phased array with a designed uniform emission from all of the 4,096 optical nanoantennas. The fiber is coupled in from the top-left corner of the image. (b) A close-up view of the near field of the farthest corner (bottom-right) of the phased array, where strong uniform emission is still observed. (c) The statical measurement of the intensity distribution out of a large number of nanoantennas in this phased array.

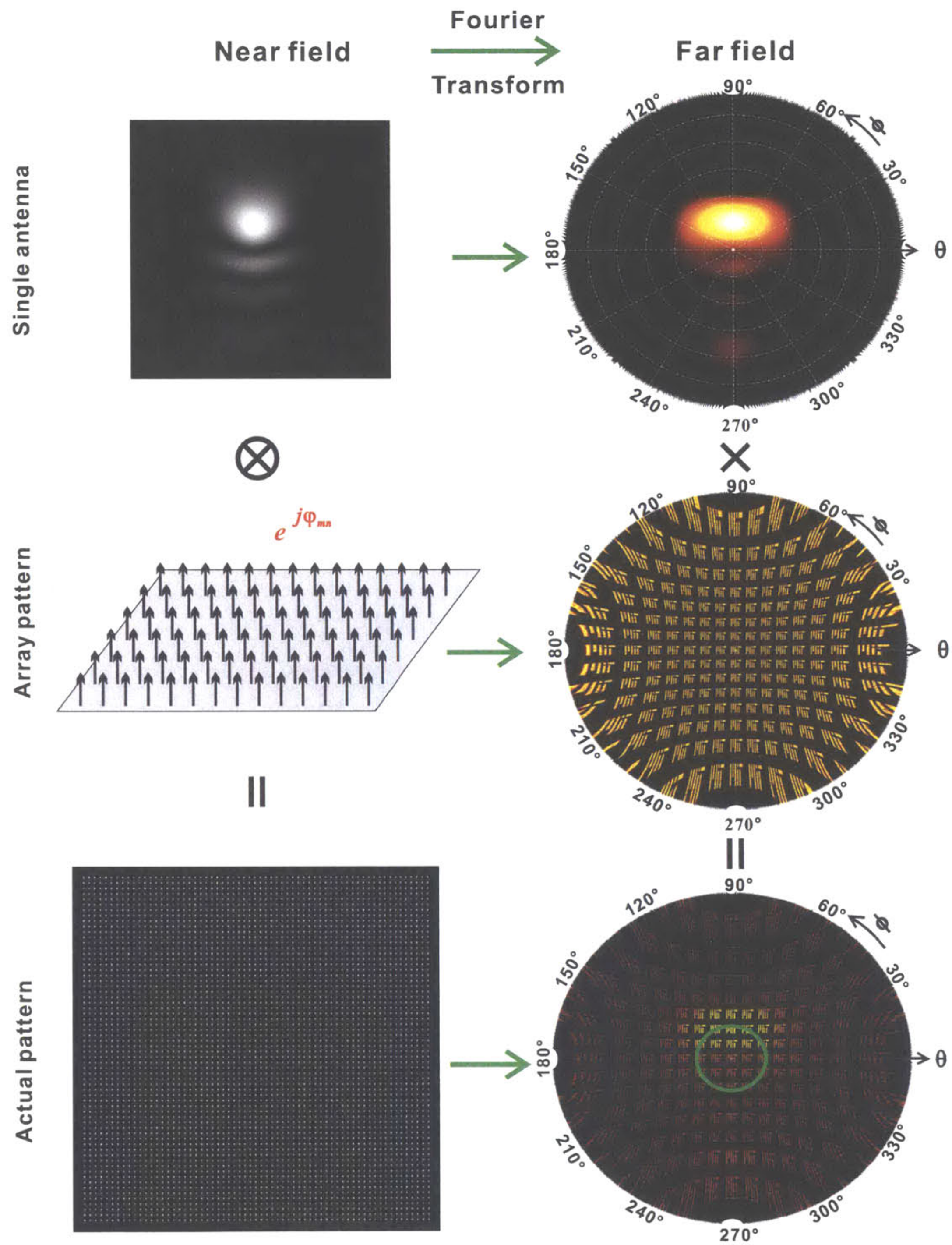

Figure 5-16 The Fourier relation between the near-field emission and its far-field pattern. All of the images are generated by simulation.

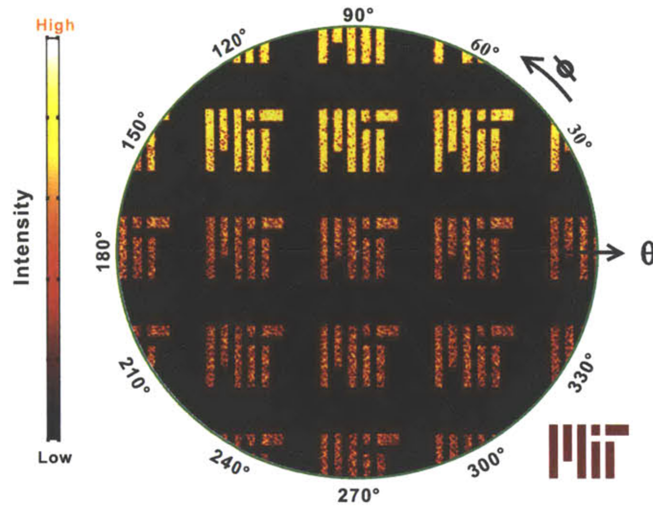

Figure 5-17 A close-up image of the simulated viewable far field. The far field is cropped by the aperture of Lens-1 with a numerical aperture NA=0.4 where the polar angle is limited by $-23.5^\circ \leq \theta \leq 23.5^\circ$. The inset shows the targeted far-field image - the "MIT"-logo.

nanoantenna emission pattern affects the far-field pattern of the whole phased array. As shown in Fig. 5-16, the near-field emission of the phased array, which is uniform in amplitude for all the 64×64 elements and with a phase configuration φ_{mn} shown in Fig. 4-6(c) to generate an "MIT"-logo in the far field, can be seen as the near-field emission of a single nanoantenna convolves with a 64×64 2-D δ-array with the corresponding phase φ_{mn}. The far-field pattern is a discrete Fourier transform of the near field, given by Equation 4.11. The Fourier transform of the near-field emission of a single nanoantenna is its far-field radiation pattern which has already been shown in Fig. 5-6(d). The Fourier transform of the 2-D δ-array (*i.e.* point-source array) with phase configuration φ_{mn} is the array factor pattern $AF(\theta, \phi)$ as shown in Fig. 4-8. The convolution '$\otimes$'in the near field becomes '$\times$'in the far field through Fourier transform. Therefore, the final far-field pattern $E(\theta, \phi)$ of the whole phased array is the array factor pattern $AF(\theta, \phi)$ multiplied by the far field $S(\theta, \phi)$ of a single nanoantenna

$$E(\theta, \phi) = AF(\theta, \phi) \times S(\theta, \phi) \tag{5.8}$$

Accordingly, the generated far-field pattern of the 64 × 64 nanophotonic phased array is simulated in Fig. 5-16. It is seen the pattern is visible only around the zenith in the far field due to the directional emission of the single nanoantenna. The green circle in the far field pattern corresponds to the numerical aperture (NA=0.4) of the objective Lens-1, which limits the viewable field that could be captured by the IR CCD. Figure 5-17 shows a close-up view of the cropped far-field pattern where the designed "MIT"-logo pattern is only visible in the top rows.

Using the setup illustrated in Fig. 5-14, the far-field radiation pattern of the aforementioned 64 × 64 nanophotonic phased array is measured, as shown in Fig. 5-18(a). The designed "MIT"-logo pattern is exactly produced in the far field. The experimental result perfectly matches to the simulation result shown in Fig. 5-17, in terms of the shape of the pattern and the intensity distribution of all of the interference orders. This highlights the robustness of the phased array system as predicted by the noise analysis in Section 4.3, as well as the reliability of the CMOS fabrication technique. The background of the far-field pattern is nosier compared to the simulation, and this is caused again by the intense light scattering from fiber-waveguide coupling which could be readily addressed by a larger separation between the coupling point and the phased array in the design. Figure 5-18(b) shows the far field of a 32 × 32 nanophotonic phased array fabricated on the same chip, where the design pattern is again reproduced in the far field. It is also noted that the far-field radiation patterns, especially in the 32 × 32 array, are slightly modulated by a concentric ring pattern. This is because of the equal-inclination interference from the multiple reflection of the light in the SOI substrate, which will be discussed in more details in Section 5.4.

Comparing Fig. 5-15(a) with Fig. 5-18, the near-field image of the nanophotonic phased array contains no information because it shows plain uniform emission everywhere; however, the far field explicitly delivers the information - an image with the "MIT" logo. Until now, image information has generally been stored and transmitted through the intensity of the pixels; in contrast, this large-scale nanophotonic phased array technology opens up another dimension for imaging:

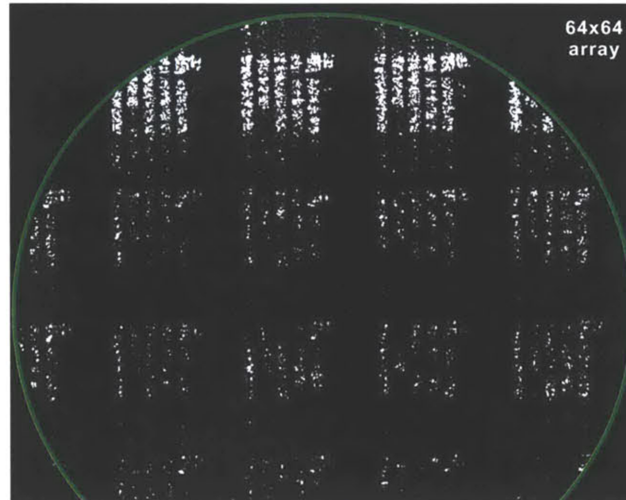

(a)

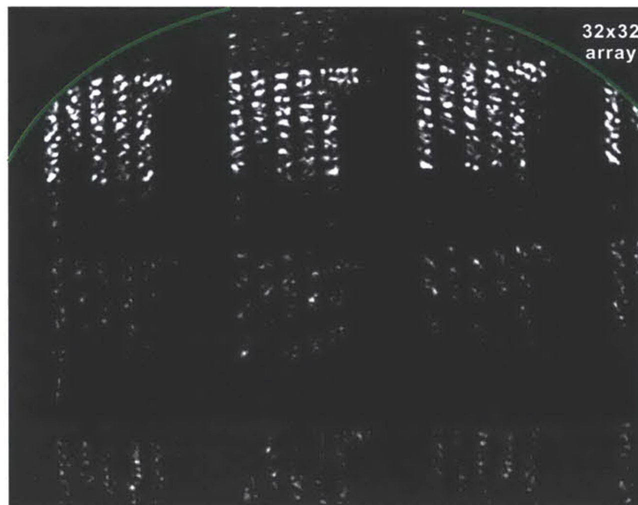

(b)

Figure 5-18 The measured far-field patterns of (a) a 64×64 nanophotonic phased array, and (b) a 32×32 nanophotonic phased array that is designed to generate the "MIT"-logo. The green circles represents the aperture of Lens-1 which has a numerical aperture NA=0.4, corresponding to a polar angle range $-23° \leq \theta \leq 23°$.

the image information is now encoded in the optical phase of the pixels, much like a hologram, but generated from a single point. This demonstration, as a static phased array capable of generating truly arbitrary radiation patterns, would find immediate applications in, for example, complex beam generation [67] and mode matching in optical space-division multiplexing [68].

5.4 Image Noise in Nanophotonic Phased Array

In the last section, we experimentally demonstrated large-scale nanophotonic phased arrays that are capable of generating arbitrary and sophisticated far-field patterns. Although the experiment results, as shown in Fig. 5-18, agree very well with the simulation in Fig. 5-17, there are still some features in the measured patterns that are not predicted by the simulations. Most noticeably, the far-field pattern is modulated by a series of concentric rings which is more obvious in the 32×32 case in Fig. 5-18(b). In this section, we will investigate of this issue.

As discussed in Section 5.1, the nanoantennas have both up-emission and down-emission. The down-emission, though lower in intensity, has a contribution to the far-field pattern which has not been taken into account in previous simulations. Especially with the nanoantenna design used in the experiment, the down-emission with 35% emission efficiency is almost comparable with the up-emission and hence should not be neglected. Next we will take into account the down-emission in the simulation and show the concentric ring modulation is actually caused by the multiple reflection of the down-emission in the SOI. Figure 5-19(a) illustrates the reflections in different material interfaces in the SOI. Reflection occurs when light emits out of the top surface (①), travels from SiO_2 to Si handle (②) and the inverse direction (④), and when light hits the bottom of the Si handle (③). The reflection coefficient (r_{ij}) and transmission coefficient (t_{ij}) at the material interface when light travels from material n_i to material n_j is given by Fresnel equation which for TE

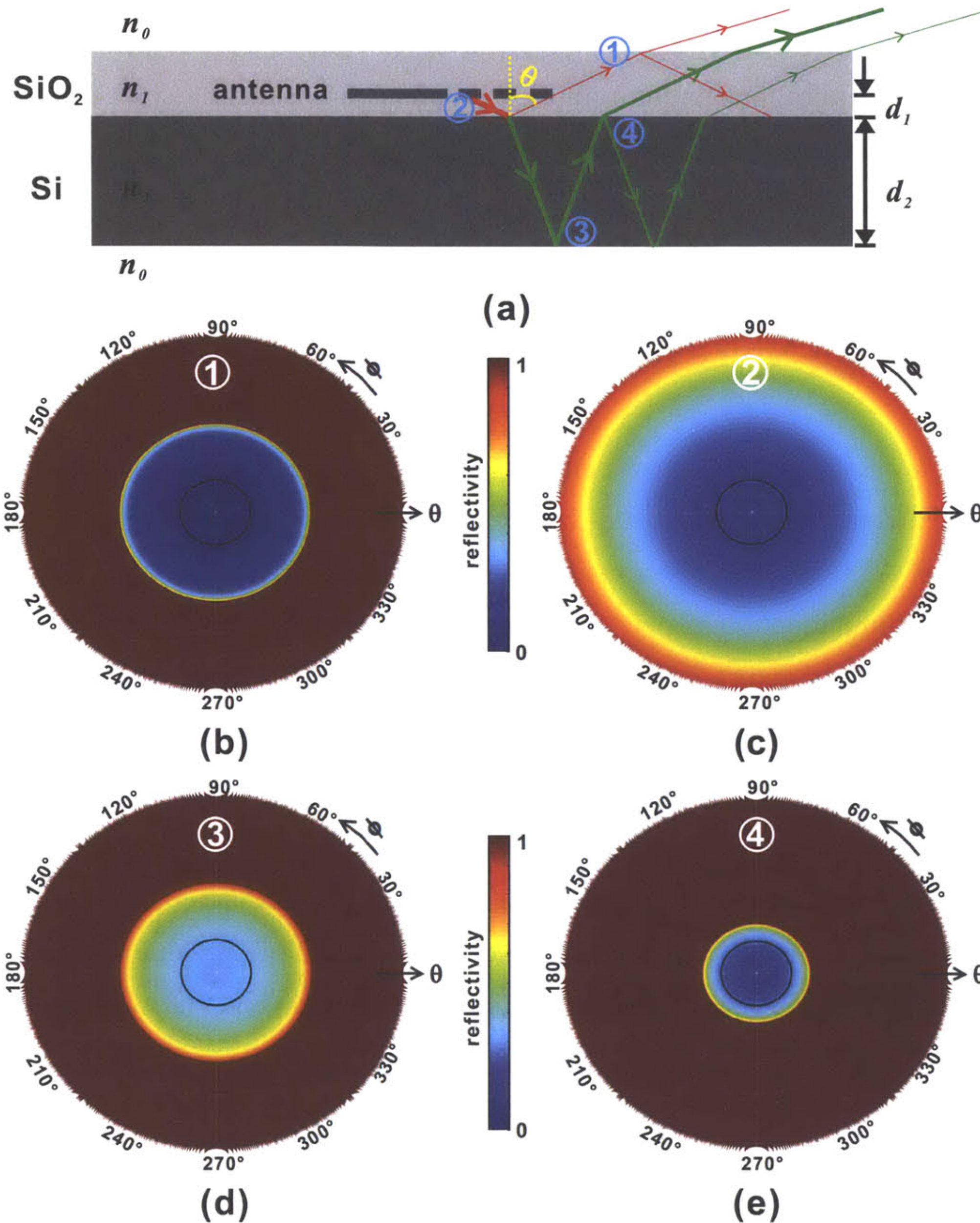

Figure 5-19 (a) A s chematic of the multiple reflection problem from the down-emission in the layered SOI. (b)-(e) The simulated reflectivity on different layer interfaces. The angle θ is the angle in SiO_2. The black circle represents the aperture of Lens-1.

wave is

$$r_{ij} = \frac{n_i \cos\theta_i - n_j \cos\theta_j}{n_i \cos\theta_i + n_j \cos\theta_j}, \quad t_{ij} = \frac{2n_i \cos\theta_i}{n_i \cos\theta_i + n_j \cos\theta_j} \tag{5.9}$$

where θ_i and θ_j are the angle of incident light and the angle of refraction respectively. Obviously θ_i and θ_j are related by Snell's law

$$n_i \sin\theta_i = n_j \sin\theta_j \tag{5.10}$$

Using these two equations, the reflectivity of light at different angles on different interfaces are calculated in Fig. 5-19(b)-(e), with the black circle indicating the viewable area with Lens-1 (NA=0.4). It is seen the top surface has very low reflection in the viewable region, thus the top-emission can transmit through with negligible reflection. The SiO_2-Si interface (② and ④) and bottom surface (③) have considerable reflections. Therefore, the multiple reflection occurs mainly between the SiO_2-Si interface and the Si-air interface, and is mainly from the down-emission which is bounced back and forth in the Si handle, as shown by the green rays in Fig. 5-19(a). For an emission angle θ, the multiple reflections interfere with each other in the far field which can be characterized by a geometric series

$$E_d(\theta) = \sum_{l=1}^{\infty} a \cdot t_{12}t_{21} \cdot \exp(j\frac{2d_1}{\cos\theta}) \cdot q^l \tag{5.11}$$

where a is the down-emission amplitude of the nanoantenna, and q is the round-trip factor of the light in the Si handle

$$q = \exp(j\frac{2d_2}{\cos\theta}) \cdot r_{20} \tag{5.12}$$

where d_1 and d_2 are the thickness of the BOX and Si handle respectively. Note that

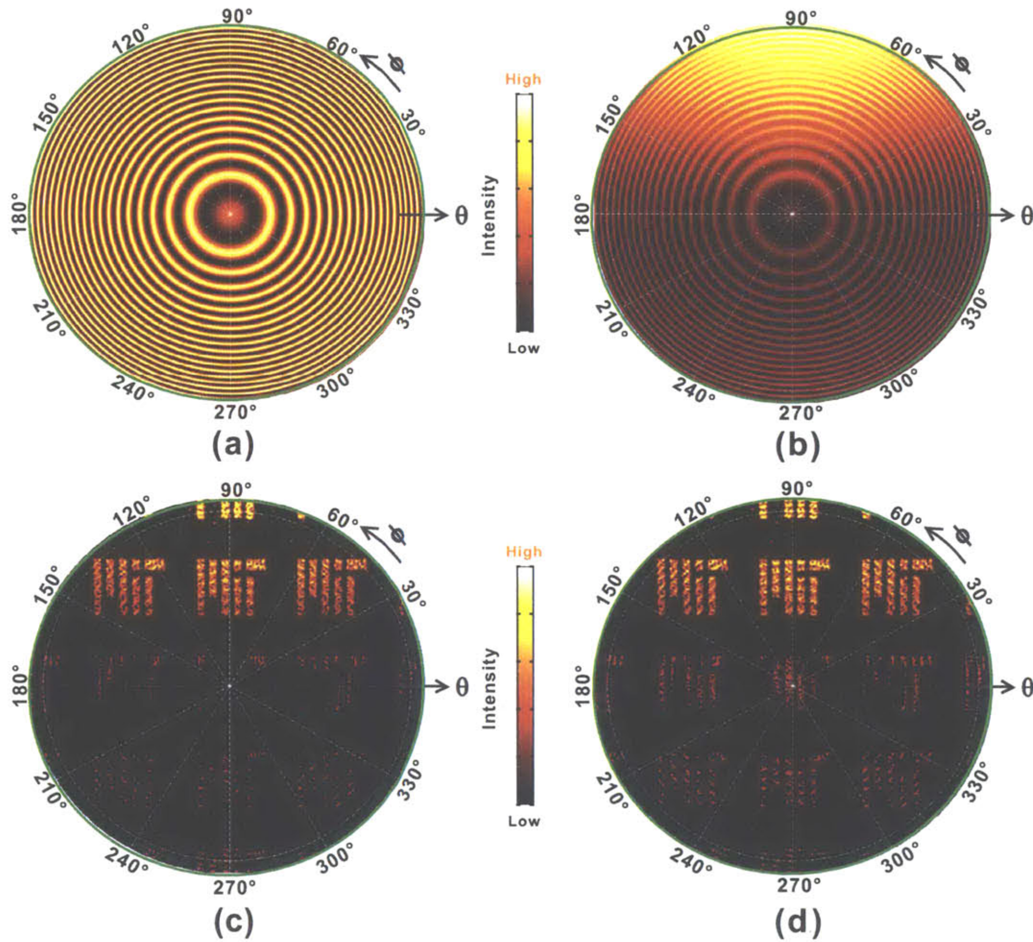

Figure 5-20 (a) The far field of the down-emission from a single point-source nanoantenna. (b) The far field of the down-emission from the single directional nanoantenna used in this work. (c) The far-field radiation pattern of the large-scale phased array formed by the down-emission only. (d) The final far-field radiation pattern of the large-scale phased array formed by the up and down emission. The green circles again represent the aperture of Lens-1.

in the above equations, the phase and amplitude of the light are relative to the up-emission. Figure 5-20(a) simulates the far field formed by the down emission from a single nanoantenna using Equations 5.9-5.12. It is seen the concentric rings are formed in the far field. This phenomenon is often referred to as equal-inclination interference since the far-field in tensity depends only on the inclination angle θ. The nanoantenna in Fig. 5-20(a) is assumed as a point-source with uniform far-field emission, and the Si thickness h_2 is 600μm. However, the nanoantenna used in the actual phased array is a directional antenna, whose far-field pattern from down-emission is similar to that from the up-emission shown in Fig. 5-6(d). With this effect taken into account, the far-field pattern from the down-emission of a single nanoantenna is simulated in Fig. 5-20(b). The far field of the phased array from the down-emission, as shown in Fig. 5-20(c), is again given by Equation 5.8 as the multiplication of the far field of the single antenna shown in Fig. 5-20(b) and the array factor pattern shown in Fig. 4-6(b). The final far-field radiation pattern of the large-scale nanoantenna phased array is simulated in Fig. 5-20(d) by taking into account both the up-emission shown in Fig. 5-17 and the down-emission shown in Fig. 5-20(c). It is noted that in Fig. 5-20(c) and Fig. 5-20(d), the designed pattern is modulated by the concentric rings which is more obvious in the low-intensity region, agreeing well with the experiment in Fig. 5-18.

Figure 5-20 explains that the concentric ring modulation in the measured far field comes from the equal inclination interference of the down-emission of the nanoantennas. The simulated final far-field pattern shown in Fig. 5-20(d) now matches very well to the experiment. However, there is still one thing that is missing from the simulation in Fig. 5-20(d), which is the phase noise as discussed earlier in Section 4.3. Figure 5-21 simulates the far-field patterns under white phase noise with different standard deviation σ. It is seen the simulation now better resembles the experimental results.

In this chapter, we have seen from the experiment that the designed large-scale nanophotonic phased array is accurately reproduced in a state-of-the-art CMOS process, with all of the 4,096 nanoantennas precisely balanced in power

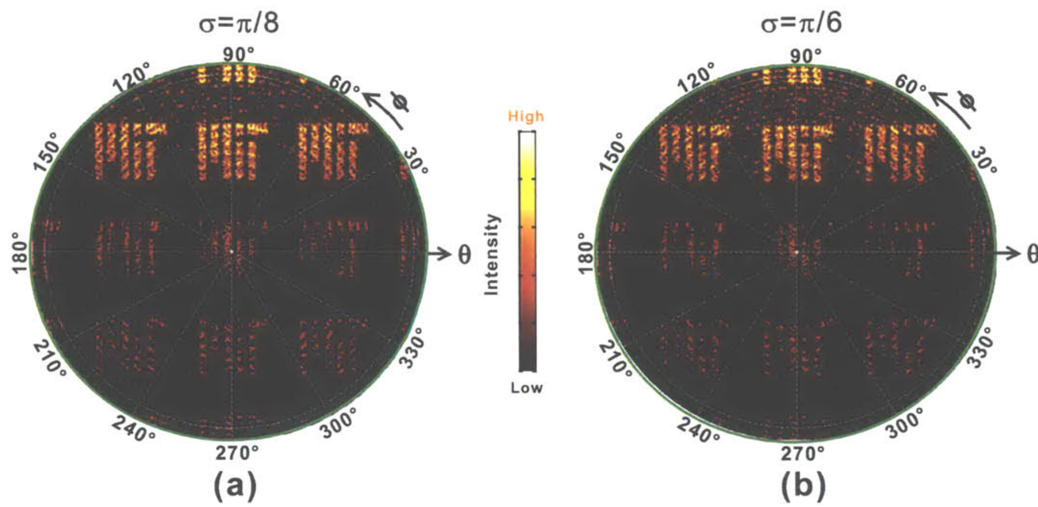

Figure 5-21 (a) Far-field pattern under a white phase noise with standard deviation (a) $\sigma = \pi/8$, and (b) $\sigma = \pi/6$. The green circles again represent the aperture of Lens-1.

and aligned in phase to create a sophisticated pattern, the "MIT" logo, in the far field as designed. This not only confirms the robust design of the nanophotonic phased array, but also demonstrates the ability and suitability of the CMOS process in fabricating large-scale integrated nanophotonic systems.

CHAPTER 6

Large-scale Active Phased Array

In Chapter 5, we experimentally demonstrated large-scale passive nanophotonic phased arrays, in which arbitrary, sophisticated patters are generated in the far field. Although the passive phased arrays that can generate static far-field patterns are interesting and have many potential applications, it is less flexible as the pattern is fixed once the phased array is fabricated. The nanophotonic phased array would be much more useful if tunabilities are built in to enable dynamic patterns in the far field. To this end, individual phase tunability has to be incorporated in each pixel so that the emitting phase of the nanoantenna can be actively controlled to have the same phased array generate arbitrary far-field patterns at will. In this chapter, we will talk about first the phase tuning mechanism used in this work and then the experimental results of the active nanophotonic phased arrays.

6.1 Integrated Silicon Thermo-optic Heater

In order to realize active nanophotonic phased array to generate dynamic far-field patterns, certain phase tuning mechanism must be applied so that the phase of

the optical emission from each nanoantenna can be actively controlled. Two major phase tuning mechanisms are generally used in silicon, the thermo-optic effect and the plasma dispersion effect. The thermo-optic effect uses the temperature dependence of the refractive index of silicon, which has a large phase tuning effect

$$\Delta n = \xi_T \cdot \Delta T = 1.8 \times 10^{-4} \Delta T \tag{6.1}$$

where ξ_T is the thermo-optic coefficient of silicon, but a relatively slow response time in the μs-scale. The plasma dispersion effect, where free carriers namely the electrons and holes are injected to or extracted from the silicon, has a much faster response time (carrier lifetime ~1ns) but a small effect on the refractive index change [69]

$$\Delta n = A \cdot N^B + jC \cdot N^D \tag{6.2}$$

where N is the electron (N_e) or hole (N_h) free-carrier concentration with unit cm^{-3}, and the parameters for electrons and holes are $A_e = -2.4 \times 10^{-22}$, $B_e = 1.1$, $C_e = 4.9 \times 10^{-26}$, and $D_e = 1.2$, and $A_h = -3.9 \times 10^{-18}$, $B_h = 0.8$, $C_h = 2 \times 10^{-24}$, and $D_h = 1.1$, which are generally very small numbers. The selection of phase tuning mechanism depends on the applications of the nanophotonic phased arrays. For example, in some applications where high-speed phase tuning is required, the plasma dispersion effect can be used. In most cases, such as the holographic display in Chapter 5 and beam shaping, large Δn is preferred so the thermo-optic effect is usually chosen. In this chapter, we will focus on the active nanophotonic phased array using the thermo-optically tunable phase shifters.

Thermo-optic effect has been widely used in silicon photonics as a typical wavelength/phase tuning mechanism in resonant filters [10][?], microring modulators, optical switches, *etc.* Most of them adopt the same scheme where metaliic heaters are used on top of the silicon structures, as illustrated by Fig. 6-1(a). Since metal

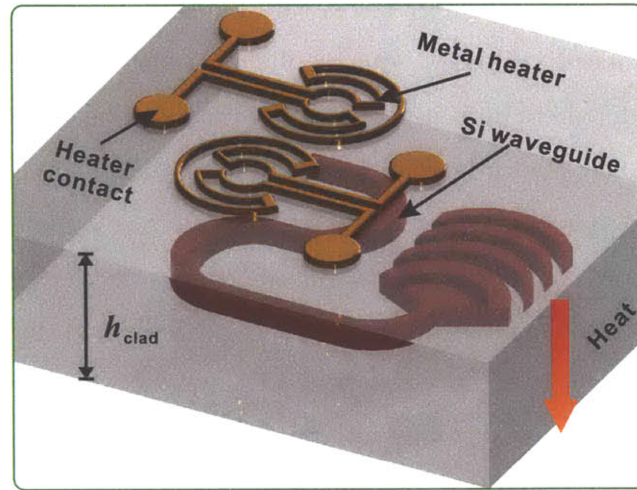

(a)

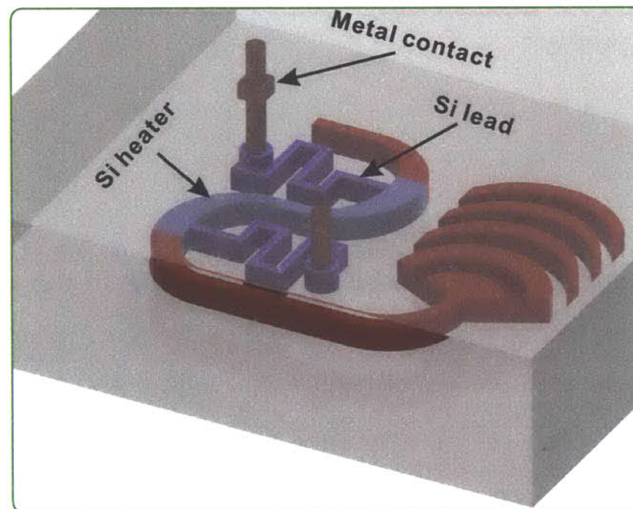

(b)

Figure 6-1 (a) Indirect thermo-optic heating of silicon waveguide where the metal heaters are placed on top of the waveguide with a vertical separation h_{clad} by SiO_2 cladding. (b) Direct thermo-optic heating of silicon waveguide where doped silicon heater is intimately integrated in the silicon waveguide to provide the most efficient heating of the silicon waveguide.

usually has large refractive index and is lossy at optical wavelength, the metallic heater has to be placed with certain vertical distance from the silicon waveguide separated by the SiO_2 over-cladding. The separation is normally as large as $\sim 1\mu m$ to to avoid significant optical losses. This results in a much less efficient heating of the silicon waveguide where light travels in since the metal heater has to heat itself and then the bulky over-cladding before it can heat up the silicon waveguide. The highest temperature in such a heating scheme is found in the metal, and then the SiO_2, and the silicon waveguide itself actually has the lowest temperature. This is not power-efficient because a lot of power is wasted in heating up the unwanted over-cladding and metal itself, nor fast-speed because the thermal diffusivity of SiO_2 is very low ($0.34mm^2/s$). Usually low power consumption and fast responding speed are preferred in thermo-optic phase tuning. We therefore define a figure of merit F to measure the performance of thermo-optic phase tuning, which is given by the power-time product

$$F = P_\pi \times \tau \quad (\mathrm{mW} \cdot \mu\mathrm{s}) \tag{6.3}$$

where P_π represents the power to achieve π phase shift in the waveguide, and τ is the thermal time constant for the waveguide to heat up or cooling down, whichever process takes longer time (usually the cooling down time). The smaller the number F is, the better the performance of the thermo-optic phase tuning is. The π-phase-shift power consumption is given by $P_\pi = \Delta T_\pi \cdot G$ where G is the thermal conductance of the waveguide to the heat sink (*i.e.* the substrate), and ΔT_π is the temperature needed to obtain π phase shift. Conversely, the thermal time constant depends on the heat capacity C_H of the heating system and the thermal conductance G as $\tau = C_H/G$. Therefore, the figure of merit is finally determined by

$$F = P_\pi \times \tau = \Delta T_\pi \cdot C_H \quad (\mathrm{mW} \cdot \mu\mathrm{s}) \tag{6.4}$$

The temperature change ΔT_π to obtain a π phase shift is fixed for a certain waveguide length since the thermo-optic coefficient $\xi_T = \Delta n/\Delta T$ is a constant. Therefore Equation 6.4 reveals that the figure of merit actually depends only on the heat capacity C_H of the heating system. A large heat capacity exists in the metal heating scheme, which results in a large F with a lot power consumption and slow phase response.

It is now obvious that the performance of the thermo-optic phase shifter can be optimized by minimizing the heat capacity C_H of the heating system. Taking advantage of the semiconductor property of silicon, the silicon waveguide itself can be converted into a heater to achieve the smallest heat capacity C_H and the most optimized figure of merit F. Figure 6-1(b) shows a schematic of such a thermo-optic phase shifter with an embedded silicon heater integrated in the waveguide. The silicon waveguide is lightly doped with ions (n-type or p-type) as shown by the blue color in Fig. 6-1(b), and is thus converted from an insulator into a resistor to provide direct heating through the electrical connections attached to the waveguide as shown by the purple color in Fig. 6-1(b). Silicon leads with heavy ion doping is used here as the electrical connection to the waveguide. The use of silicon simplifies the fabrication process as the silicon connection can be formed together with waveguides in the same etch step, and the heavy doping offers a small resistance so that most of the electrical potential drops on the waveguide heater to increase the heating efficiency. However, it is nontrivial to design a low-loss electrical connection that is intimately in contact with the silicon waveguide where light travels through, because direct contacting a narrow waveguide with a silicon lead causes significant optical scattering loss. Here we use a novel waveguide structure [71]-[72], namely the adiabatic bend proposed by Watts *et. al.*, to provide electrical connections to the waveguide while minimizing the optical loss.

Figure 6-2 illustrates the principle of the adiabatic bend to provide low-loss electrical connections. The adiabatic bend, as shown in Fig. 6-2(b), is achieved by slowly changing the inner radius of the waveguide, moderately stretching the width of the waveguide bend from a single-mode input width w_0 to a multi-

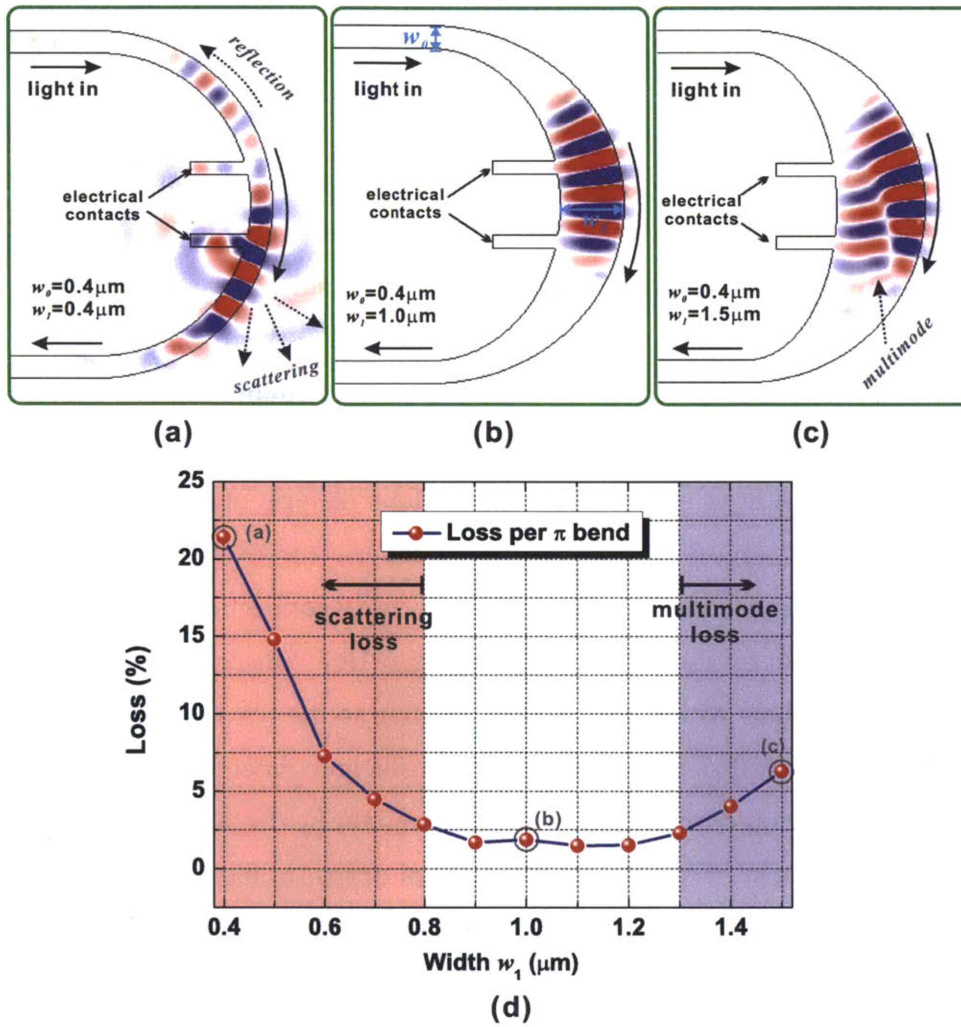

Figure 6-2 (a) Electrical contacts that are intimately connected to a narrow waveguide bend ($w_1 = w_0$)create strong scattering loss. (b) Electrical contacts that are attached to the inner side of an adiabatic bend ($w_1 > w_0$)eliminate the scattering loss. (c) Non-adiabatic bend ($w_1 \gg w_0$) generates high-order modes and is thus lossy. (d) The optical loss per 180°-bend at different bend width w_1

mode region with a wider width w_1 where contacts can be introduced where there is little optical field. Contact with the wide waveguide region ensures minimal perturbation to the waveguide mode and therefore eliminates the scattering loss, while the waveguide width changes in an adiabatic manner to avoid mode coupling into high-order mode that will finally radiate to generate optical loss. Using 3-D FDTD, optical propagation is simulated at different width w_1. Figure 6-2(a) shows the case when the bend is not widened ($w_0 = w_1$), where significant scattering loss is seen because of the strong perturbation of the electrical contact to the optical mode tightly confined in the narrow waveguide. Figure 6-2(c) shows the case when the bend is largely widened ($w_0 \ll w_1$), where the scattering loss is suppressed but strong coupling to high-order modes occurs because of the rapid change of waveguide width in a non-adiabatic manner. The high-order modes will finally radiate in the transition to narrow waveguide following the bend and causes optical loss. Figure 6-2(d) simulates the optical transmission loss per 180°-bend at different width w_1. It is seen the scattering loss dominates when the width is too small while high-order mode loss emerges when the width w_1 is too large. The optimal point happens at a moderate width w_1, which is 1.0μm in the simulated structure with a bend radius R = 3.0μm and initial waveguide width w_0 = 0.4μm. Note that the structure used in this simulation is slightly different from what we will use in the active phased array demonstration, but it shows the basic principle that applies to all adiabatic-bend structures.

Based on this adiabatic bend, the active pixel for the tunable phased array is designed with a directly embedded silicon heater, as illustrated in Fig. 6-3. The basic waveguide structure of the active pixel resembles the passive pixel as described in Chapter 5. The straight waveguide width is 0.46μm. The adiabatic bend has a circular outer edge with 2.0μm radius and an elliptical inner edge with 1.0μm x-axes and 1.54μm y-axes to make a wider center part in the bend of 1.0μm. Part of the waveguide is lightly doped with Arsenic (**As**) at a dosage of 4×10^{13}cm^{-2} which gives a free carrier concentration of 1.8×10^{18}cm^{-3}, as shown by the light-blue color in Fig. 6-3. Two narrow silicon leads with a width of 0.2μm are connected to the

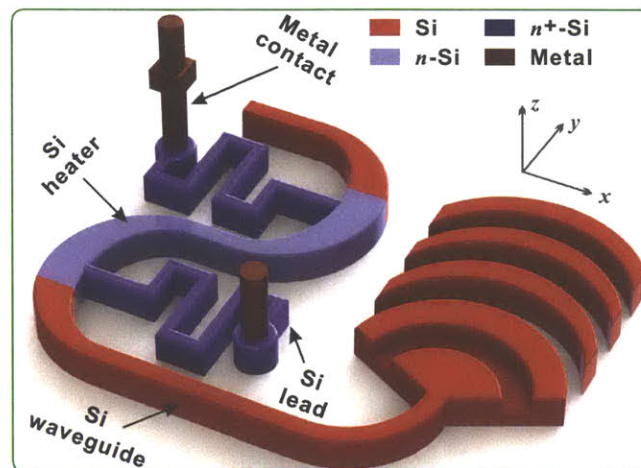

Figure 6-3 Schematic of an active pixel with a tunable phase shifter in the dynamic phased array. The heavily-doped silicon leads are connected to the inner side of an adiabatic waveguide bend. The silicon leads are contacted with metals which are subsequently connected to metal layers.

widened region of the adiabatic bends to provide electrical connections. The silicon leads are heavily-doped with Phosphorus (**P**) at a dosage of 5×10^{15}cm^{-2} which gives a dopant concentration of 2.3×10^{20}cm^{-2}. The heavy doping minimizes the resistance of the silicon leads so that the electrical power drops mainly on the heater. The silicon leads are made narrow and zigzagged to provide thermal isolation between the silicon heater and the metal contacts to prevent metal from melting at high temperatures. The other end of the silicon lead is contacted with metal which then connects to subsequent metal layers for electrical interconnections.

6.2 8×8 Active Phased Array

With the directly integrated silicon heater, the optical phase of the nanoantennas can be individually adjusted from 0 to 2π so that arbitrary patterns can be dynamically generated by applying different phase patterns on the array. Ideally, each pixel in the large-scale nanophotonic phased array should be separately addressed and electrically controlled in order to independently tune the phase of each pixel. In order to realize this, a large number of electrical interconnection wires has to

Figure 6-4 Schematic of an 8×8 active phased array consisting of 64 active pixels shown in Fig. 6-3. The electrical interconnections are simplified by connecting together the tunable phase shifters in the same rows and in the same columns.

be densely packed and routed to fit in the small pixel pitch which will require multiple metal levels; or instead, the pixels can be addressed in a digital way by implementing a CMOS control circuit on the same chip by 3-D electronic-photonic integration. However, none of these fabrication process options is available in the current stage for our design. Therefore, the active nanophotonic phased array demonstration is reduced to an 8×8 case with 64 nanoantenna, but still it represents the largest optical phased array that has ever been demonstrated. The 8×8 phased array is further simplified in which the tunable phase shifters in the same rows and columns are electrically connected together and adjusted simultaneously, as shown in Fig. 6-4. This interconnection scheme enables much easier electrical routing in the small $9\mu m\times9\mu m$ pixels using only 2 metal levels which are readily available in our fabrication process.

The designed 8×8 active phased array with the interconnection structure shown in Fig. 6-4 is fabricated in a standard 300-mm CMOS foundry. The passive silicon waveguides and nanoantennas as well as the integrated silicon heaters are fabricated with CMOS processing techniques described earlier in Section 5.1.2 and 6.1.

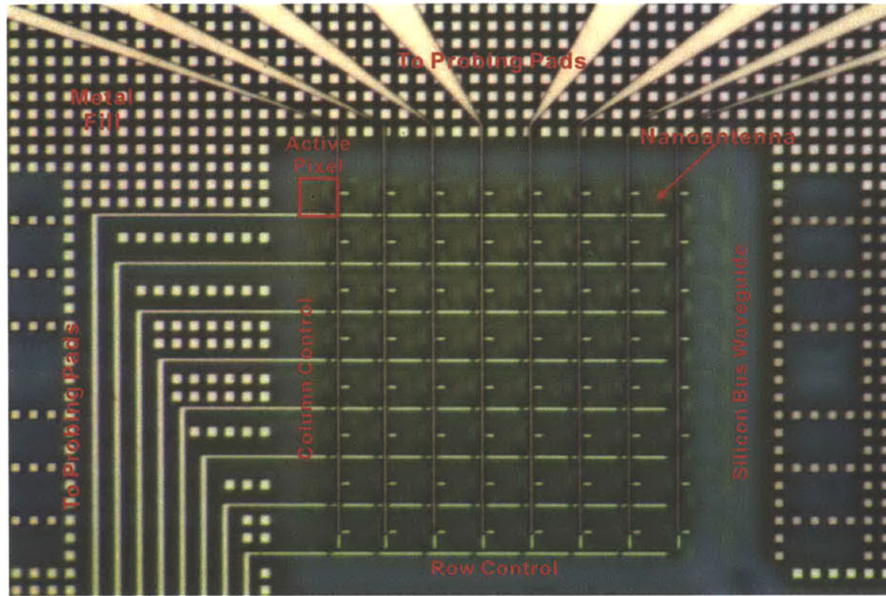

Figure 6-5 Optical micrograph of a fabricated 8 × 8 active phased array. The silicon waveguides are seen as green, while the lower and upper copper interconnection layers are seen as bright yellow and pink, respectively. The two metal levels are connected by copper vias.

Figure 6-5 shows an optical micrograph of the fabricated 8 × 8 active nanophotonic phased array, where two copper (**Cu**) layers are used to provide electrical interconnections to the integrated silicon heaters. The probing pads, which are 50μm×50μm squares with 100μm pitch, are also made in the upper metal layer to provide electrical potentials to the rows and columns from outside sources when connected by electrical characterization probes.

The fabricated 8 × 8 active nanophotonic phased array shown in Fig. 6-5 is optically fed by 1.55μm laser from a fiber and electrically powered by 16 electrical potentials from two 9-pin probes, and the far-field of the phased array is measured with an infrared camera in the setup shown by Fig. 5-14. The phased array is designed to emit with the same phase from all of the 64 nanoantennas, creating a focused beam in the center of the far field, as shown by Fig. 6-6(a). Multiple interference orders are seen again here because the pixel pitch (9μm×9μm) used here is much larger than the half wavelength. By applying different voltages on the

rows and columns, various phase patterns can be generated to create corresponding radiation patterns in the far field, as shown in Fig. 6-6(b)-(e). The left column in Fig. 6-6 illustrates the phase patterns in the near field, while the central and right columns show the corresponding simulated and measured far-field patterns respectively.

By applying a phase pattern with an incremental phase change $\Delta\varphi_0$ between adjacent rows or columns, the focused beam can be steered in vertical and in horizontal. The steering angle α is given by

$$\sin\alpha = \frac{\Delta\varphi_0 \cdot \lambda_0}{2\pi \cdot p} \tag{6.5}$$

where λ_0 is the wavelength in the far-field medium (such as air in this work), and p is the pixel pitch. The maximum steering angle at 1.55μm wavelength with 9μm×9μm pixel pitch is $\alpha_{\max} \approx 10^\circ$ which is also the field of view of the far field interference pattern. Note that since the tunable phase shifter works in the range $(0, 2\pi)$, the additional phase φ_i provided by the thermo-optic phase shifters in the ith row or column is the residue of $(i-1)\Delta\varphi_0$ modulo 2π. Figure 6-6(b) and (c) show the focused beam is steered by 5° to the edge of the interference order in vertical and horizontal directions. The applied voltage is 4.6V on every other row or column to create a phase difference $\Delta\varphi_0 = \pi$ so that the phase pattern is $(0, \pi, 0, \pi, 0, \pi, 0, \pi)$ row-wise or column-wise as shown by the left column in Fig. 6-6. The measured resistance per silicon heater is around 2.5kΩ, and the electrical power required to achieve π-phase-shift in a unit pixel is 8.6mW which is very power-efficient in comparison with previous thermo-optic phase shifter demonstrations.

Figure 6-6(b) and (c) demonstrate the 2-D beam steering capability of the fabricated 8×8 active nanophotonic phased array. This represents the first-ever 2-D integrated optical phased array that has truly 2-D beam steering ability, benefiting from the optimized photonic design with a compact phase shifter. While beam steering is the conventional functionality of RF phased arrays as well as optical

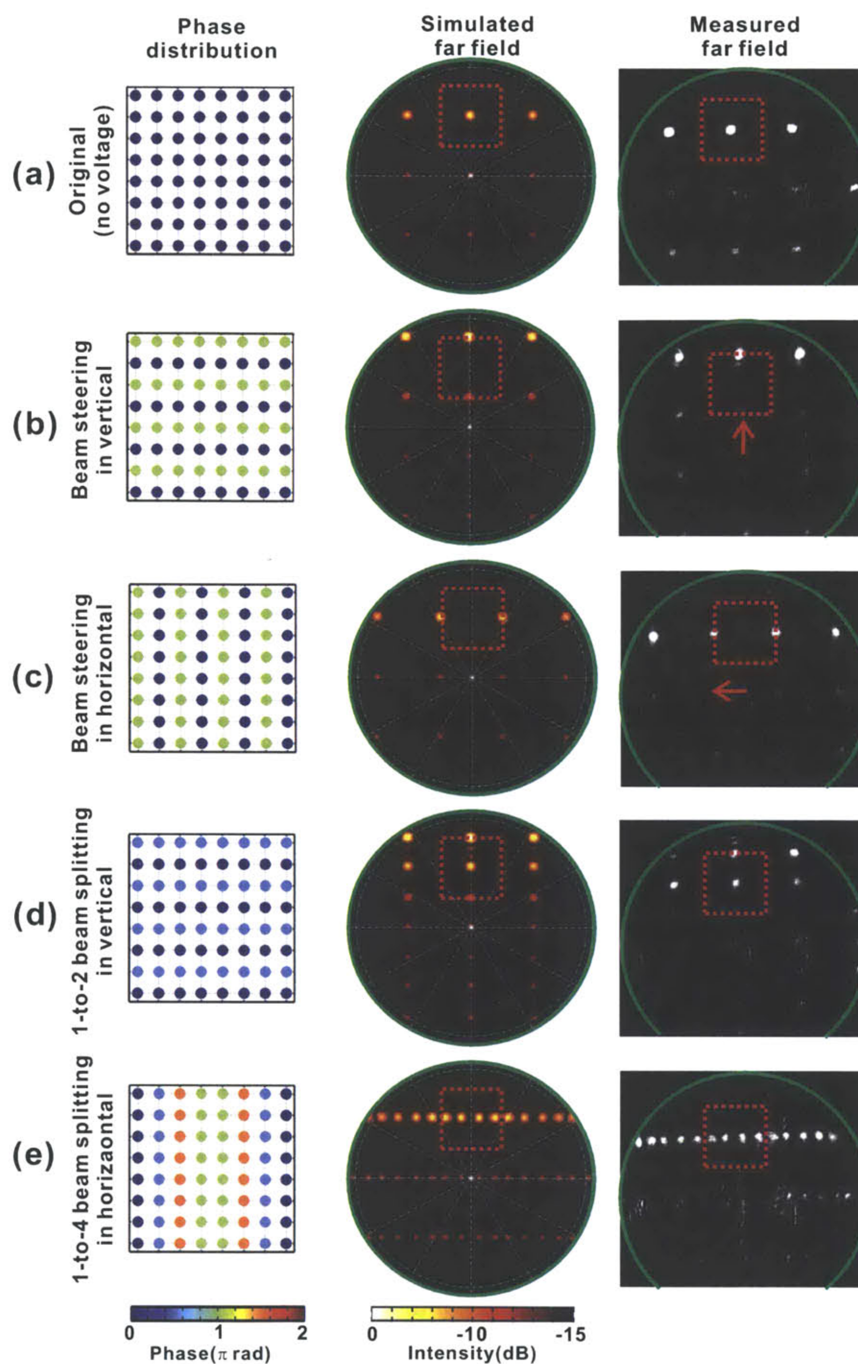

Figure 6-6 Experimental results of the 8 × 8 active phased array for beam steering and shaping. (a) The original single-beam pattern with no voltage on. (b) The focused beam is steered by 5° to the edge of each interference order in the vertical, and (c) in the horizontal. (d) The single beam is split into two beams in the vertical direction. (e) The single beam is split into four beams in the horizontal direction.

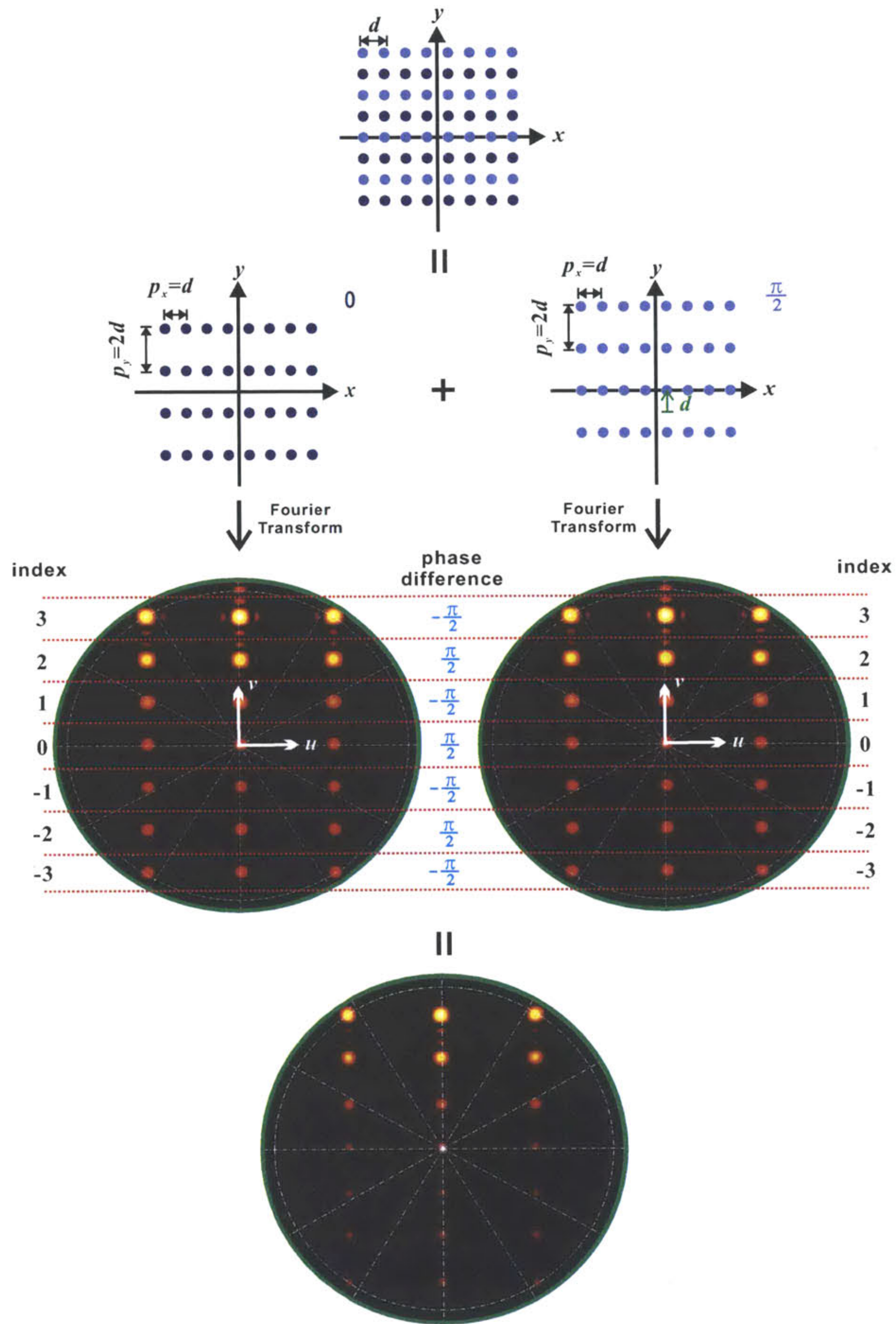

Figure 6-7 An explanation of the beam splitting in the 8 × 8 nanophotonic phased array. The phased array with alternating phase can be treated as a combination of two 4 × 8 phased arrays which have the same far-field intensity but different far-field phase. The final far field results from the interference of the two arrays.

phased arrays studied previously, more complex beam manipulations can be realized by applying other phase patterns on the array. Figure 6-6(d) shows the single focused beam is split into 2 beams vertically with the row-wise phase configuration $(0, \frac{\pi}{2}, 0, \frac{\pi}{2}, 0, \frac{\pi}{2}, 0, \frac{\pi}{2})$, and Fig. 6-6(e) shows the single beam is split into 4 beams horizontally with the column-wise phase configuration $(0, \frac{\pi}{2}, \frac{3\pi}{2}, \pi, \pi, \frac{3\pi}{2}, \frac{\pi}{2}, 0)$. Next we will analyze the mechanism of the beam splitting in the phased array, taking the phase configuration shown in Fig. 6-6(d) as an example. As shown in Fig. 6-7, the 8×8 nanoantenna array with emitting phase alternating between 0 and $\frac{\pi}{2}$ can be seen as a combination of two 4×8 phased arrays, one with all of the antennas emitting at phase 0 and another with all of the antennas emitting at phase $\frac{\pi}{2}$. The first array on the left side of Fig. 6-7 is centered at $y = 0$ in the y-direction and has a far field given by Equation 4.12 as

$$AF_1(u, v) = \sum_{m=1}^{M} \sum_{n=1}^{N} e^{j2\pi(x_m \cdot u + y_n \cdot v)} \tag{6.6}$$

where u and v are the far-field coordinates which were defined earlier by Equation **??**. The generated far field from this single 4×8 array is shown in the left side of Fig. 6-7. It is seen that the period of the far-field pattern is doubled in the v direction because the y-direction pitch of this 4×8 array is doubled. The other array on the right side is the same except that the position of the array is shifted toward $+y$-direction by d. The far field of the right-side 4×8 array is again given by

$$AF_2(u, v) = \sum_{m=1}^{M} \sum_{n=1}^{N} e^{j\frac{\pi}{2}} \cdot e^{j2\pi[x_m \cdot u + (y_n + d) \cdot v]} \tag{6.7}$$

Combining Equations 6.6 and 6.7, one can find

$$AF_2(u, v) = e^{j(\frac{\pi}{2} + d \cdot v)} \cdot AF_1(u, v) \tag{6.8}$$

Equation 6.9 shows that the two 4×8 arrays have the same intensity distribution but with phase difference $\frac{\pi}{2} + d \cdot v$. The phase difference depends on the far-field position v. The far-field pattern is periodic with the focused beams locate at $u = l \cdot p_u$ and $v = k \cdot p_v$ where (p_u, p_v) are the far-field period in u and v directions, and (l, k) are the index indicating the order of the far-field beams in u and v directions. Because of the Fourier relation between the array and its far field, the far-field periods are given by $p_u = 2\pi/p_x = 2\pi/d$ and $p_v = 2\pi/p_y = \pi/d$. Therefore the phase difference between the far fields of the two 4×8 phased arrays is $\frac{\pi}{2} + k \cdot \pi$ which depends on the interference order k of the beam. When the far fields of generated by the two arrays add up, this phase difference creates interference patterns. Under the phase configuration shown in Fig. 6-6(d) or in Fig. 6-7, the adding gives a factor of $1 + e^{\pm j\frac{\pi}{2}}$ to all of the interference orders of the 4×8 phased array, so that all of the orders have the same intensity. As a result, it is seen the beam is equally split into two beam. On the contrary, under the phase configuration shown in Fig. 6-6(a), the adding gives a factor of $1 + e^{j(k+1)\cdot\pi}$, meaning the beams in the odd orders ($k = \pm 1, \pm 3, \cdots$) stay because of constructive interference while the even order beams ($k = 0, \pm 2, \cdots$) vanish due to destructive interference. As a consequence, it appears the beam is steered in Fig. 6-6(a). The above analysis gives an intuitive explanation of beam splitting in phased arrays and also provides an easy way to design the phase configuration to split one focused beam into the desired number of beams. This beam steering and beam splitting capability enabled by an ultra-compact nanophotonic phased array can find many potential applications such as optical tweezers where the beams can be used to manipulate small particles or biological cells.

In this section, we have demonstrated an active nanophotonic phased array whose far-field patterns can be dynamically changed by applying voltages on the thermo-optic phase shifters in the array. Although a small-scale phased array and simplified electrical connections are used in the demonstration to facilitate fabrication, the 8×8 active phased array, which can generate rather complex patterns in spite of the limited number of antennas and electrical connections, still represents

the largest active 2-D optical phased array that has ever been demonstrated. Moreover, with the aid of a digital circuitry integrated with the nanophotonic phased array by means such as 3-D eletrical-optical integration, large-scale active phased array up to millions of pixels with individual phase control of each pixel can be realized, which has the ability to generate complex dynamic images and is an enabling technique for a broad range of applications such as the truly 3-D holographic displays.

6.3 Amplitude-modulated Phased Array

Coherent light, or electromagnetic waves in general, is characterized by two independent properties: amplitude (or intensity) and phase. The previous demonstrations of nanophotonic phased array makes use of the optical phase alone to shape the radiation field. There is another degree of freedom in light, *i.e.* the amplitude, that is yet to be used to manipulate the radiation in phased arrays. That is, instead of keeping the emission amplitude uniform across the whole array as we already demonstrated earlier, one can have the optical emissions of the phased array follow a certain intensity pattern in the near field to generate a corresponding radiation profile in the far field. This is attractive in the sense that this additional degree of freedom to control the phased array completes the one-to-one mapping between near field and far field which are related by Fourier transform as shown by Equation 4.13, because now not only arbitrary phase configuration φ_{mn} but also arbitrary amplitude profile $|w_{mn}|$ can be achieved in the phased array. However, all of the previously demonstrated optical phased arrays using 3-dB couplers to divide optical power as shown in Fig. 5-8 are not capable of arbitrarily distributing optical power to each antenna. In comparison, the nanophotonic phased array architecture we proposed in this work where directional couplers are used to distribute optical power provides unique opportunities to achieve arbitrary emission amplitude profile since the coupling to each nanoantenna can be adjusted at will, which in turn creates many features that cannot be realized in uniform phased

arrays, as will be discussed in the following.

In the phased array with uniform emission amplitude, unwanted side lobes always exist aside the main focused beam, as shown in Figure 6-8. Figure 6-8(a) and (b) show the simulated and experimental near-field emission from a uniform 8×8 nanophotonic phased array, where the emission amplitude from all of the 64 nanoantennas is designed to be uniform. Figure 6-8 (c) and (d) show the simulated and measured far-field pattern of the uniform phased array, where side lobes are seen around each of the focused beams. Note that these side lobes were not seen in previous results of 8×8 uniform phased array in Section 6.2 because of the contrast ratio used in those images, but the side lobes do exist as verified by both simulation and experiment in Fig. 6-8. These side lobes arise from the fact that the uniform phased array with finite number of antennas has a box-like amplitude profile that through Fourier transform creates the *sinc*-like beams in the far field with many side lobes, as already seen with the 1-D phased array in Fig. 4-3. Also note that the term 'side lobe'used here should be distinguished from the term 'side order'used earlier in this work which refers to the multiple focused beams as high interference orders in the far field.

Much like the apodization technique in Bragg gratings where the grating strength is modulated along the grating length to suppress the side lobes in the grating spectrum, the unwanted side lobes in phased array can also be suppressed by modulating the amplitude of the optical emissions with, for example, a Gaussian-shaped profile, so that the focused beam in the far field has a corresponding Gaussian shape instead of a *sinc*-shaped beam. As shown in Fig. 6-9, an 8×8 nanophotonic phased array is by design modulated by a Gaussian-shaped amplitude profile which has an expression

$$|w_{mn}| = e^{-2.2 \cdot \frac{(x_m - x_0)^2 + (y_n - y_0)^2}{r_{\max}^2}} \tag{6.9}$$

where (x_m, y_n) is the coordinate of pixel (m, n), and (x_0, y_0) is the center of the

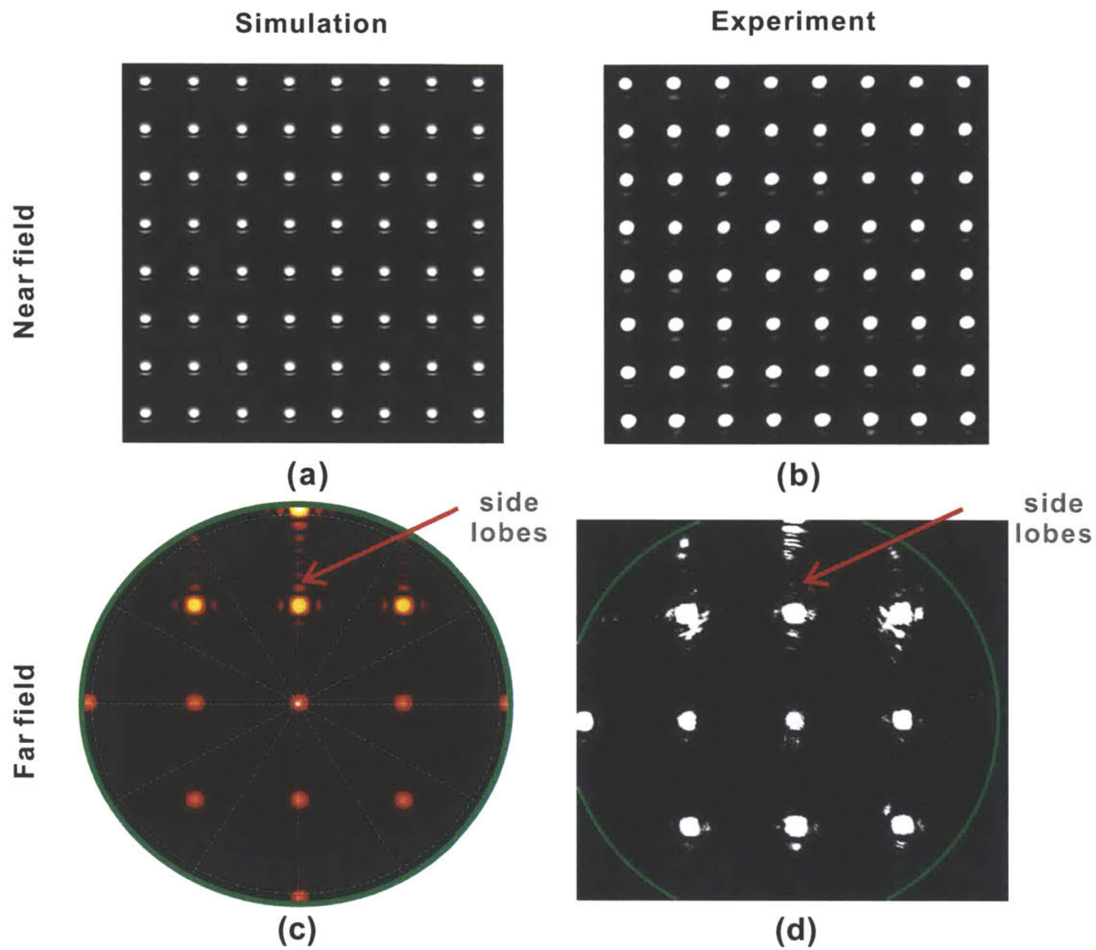

Figure 6-8 Illustration of side lobes in the 8×8 nanophotonic phased array with uniform emission amplitude. (a) Simulated and (b) measured near-field emission from the 8×8 uniform phased array, where uniform emission intensity is observed from all of the 64 nanoantennas. (c) Simulated and (d) measured far-field pattern of the uniform 8×8 phased array, where side lobes are seen around the main lobe.

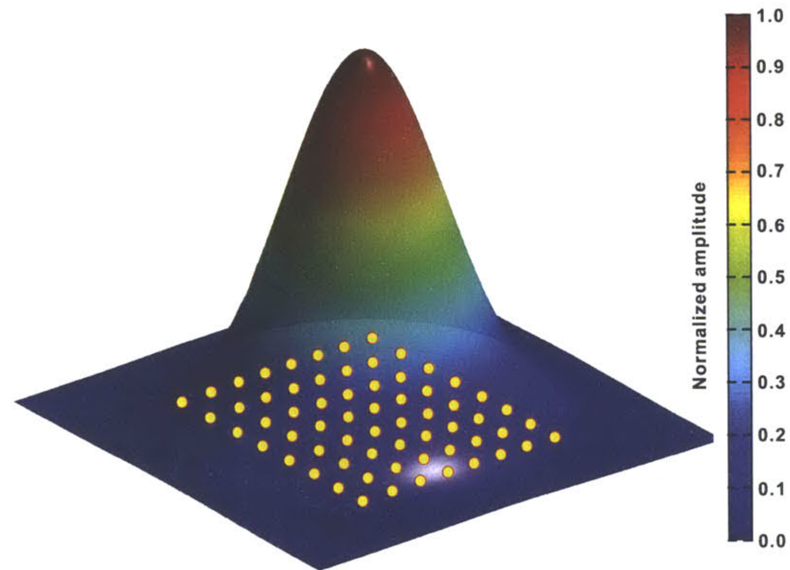

Figure 6-9 The 8×8 nanophotonic phased array is modulated by a Gaussian profile. The yellow dots on the bottom stand for the phased array.

phased array. $r_{\max}$ stands for the maximum distance from any antenna to the center of the phased array. This amplitude modulation profile $|w_{mn}|$ can be realized in the proposed nanophotonic phased array architecture by accordingly adjusting the coupler length and hence the coupling efficiency in the bus-to-row directional couplers and the row-to-unit directional couplers. The coupling efficiency can be calculated from Equations 5.5 and 5.6, and the corresponding coupler length can be derived from the 3-D FDTD simulation as shown in Fig. 5-11.

Figure 6-10(a) and (b) show the simulated and measured near-field emission of the amplitude modulated 8×8 phased array. A centrally symmetric nonuniform amplitude modulation is seen in the measured near field, as designed. Note that some pixels in the corner are too dark to be observed by the IR CCD. This Gaussian-shaped amplitude modulation suppresses the side lobes in each interference order, as seen in the simulated far-field pattern in Fig. 6-10(c). Each of the beams in the far field should have a Gaussian shape in its cross section. This is easy to understand since the near-field emission and the far-field pattern are related by Fourier transform as given by Equation 4.13, and the Fourier transform of a Gaussian function is still a Gaussian function. Therefore it is straightforward to generate focused optical beams with other complex shapes using amplitude modulated phased arrays. Figure 6-10(d) shows the measured far-field pattern of the amplitude modulated 8×8 phased array where no side lobe is seen. An excellent agreement with simulation is again observed. It is noticed that the beam size in the modulated phased array is larger than the uniform phased array with the same scale, because the amplitude modulation decreases the effective length of the phased array in both x and y directions which through Fourier transform results in a larger beam in the far field.

Now we have seen that the far-field radiation pattern can also be shaped by controlling the emission amplitude of the phased array. There is another degree of freedom of light, *i.e.* the optical phase, yet to be used in the amplitude-modulated phased array. As discussed in the last section, the optical phase in the phased array can be adjusted to realize various beam shaping functions such as beam steering and beam splitting. Now we use the same principle to dynamically shape

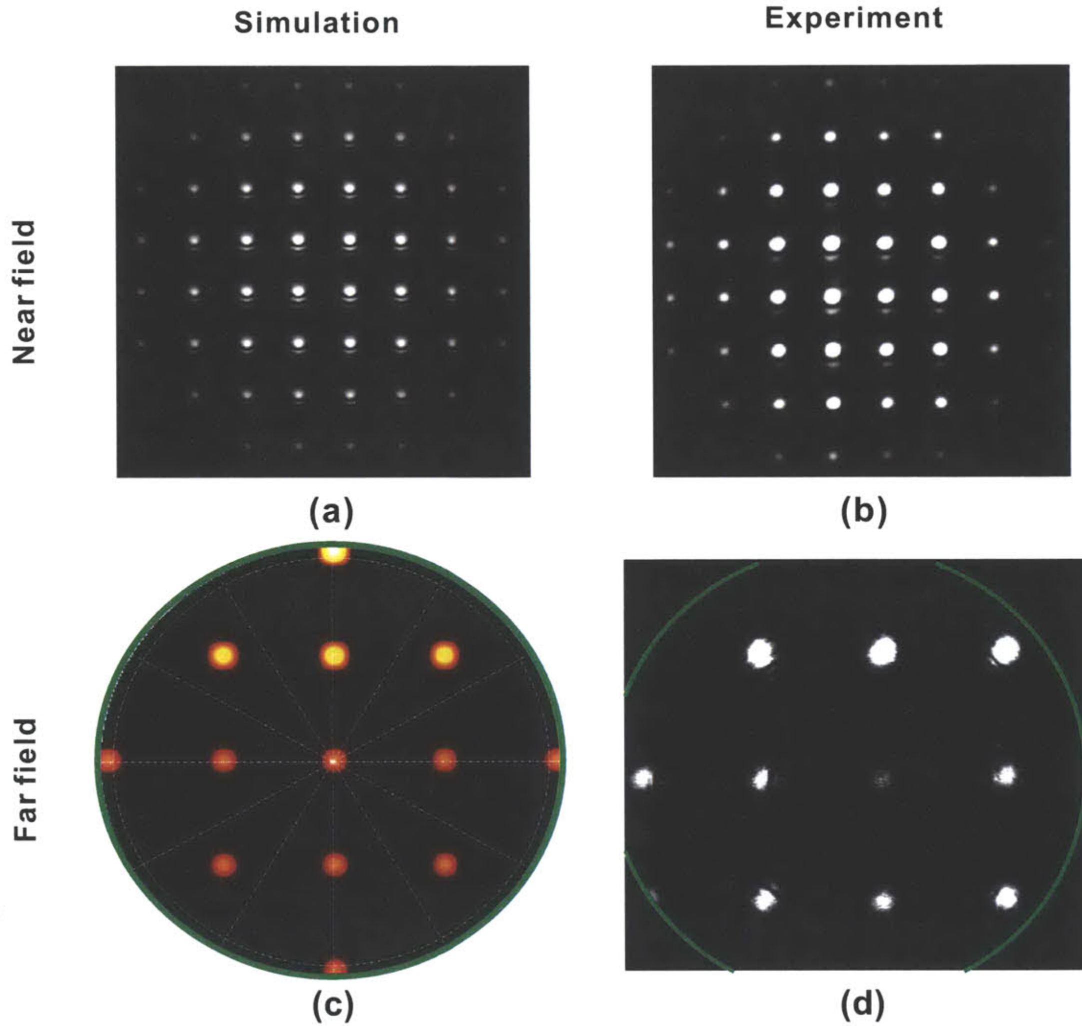

Figure 6-10 8 × 8 nanophotonic phased array with Gaussian-shaped amplitude modulation. (a) Simulated and (b) measured near-field emission from the 8 × 8 phased array, where the emission amplitude is modulated by a Gaussian profile given by Equation 6.9. Note that some pixels in the corner are too dark to be seen. (c) Simulated and (d) measured far-field pattern of the amplitude modulated 8 × 8 phased array, where side lobes are largely suppressed.

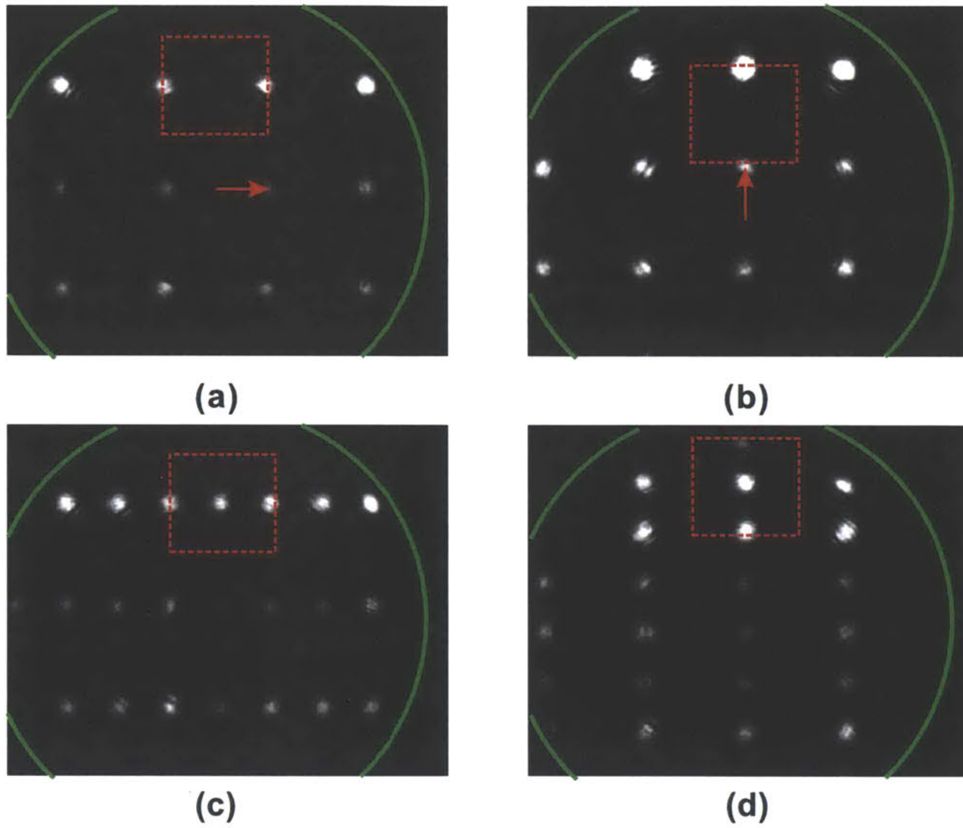

Figure 6-11 Active tuning of the 8×8 nanophotonic phased array with Gaussian-shaped amplitude modulation. The Gaussian-shaped focused beam is steered by 5° in (a) x-direction and (b) y-direction; and the beam is split into 2 beams in (c) x-direction and (d) y-direction.

the amplitude modulated phased array by actively controlling its phase pattern as well. Figure 6-11 shows the experimental beam shaping results of the phased array used in Fig. 6-10 by adjusting its phase configurations using the thermo-optic phase shifters. Figure 6-11(a) and (b) show the Gaussian-shaped optical beam is steered in x and y direction respectively, and Fig. 6-11(c) and (d) show the beam is split into 2 beams in x and y directions respectively.

In this chapter, we have demonstrated a compact and efficient thermo-optic phase shifter that can be directly integrated into each pixel in the nanophotonic phased array so that dynamic patterns can be generated in the far field. The far-field radiation pattern can be shaped not only by the optical phase but also the optical amplitude of the phased array, as well as the combination of the two. The active phased arrays demonstrated here are limited to a relatively small-scale with simplified electrical controlling circuitry, however, with the aid of an advanced CMOS digital circuitry, it is possible to actively tune the phase of each of the pixels in a large-scale phased array which will enable the dynamic generation of holographic patterns in the far field.

CHAPTER 7

Conclusions and Perspectives

7.1 Summary of Accomplishments

This thesis work focused on two main challenges in silicon photonics: the device accuracy and the integration capability. The fabrication technique and the design strategy toward accurate silicon photonic devices were discussed and demonstrated, and the large-scale integration of a large number of silicon photonic devices was experimentally realized in a small silicon chip to form a functional silicon photonic system.

Silicon photonic devices, like transistors in microelectronics, are fundamental building blocks in silicon photonic circuits. To achieve accurate silicon photonic devices is extremely challenging due to the short wavelength of light and high refractive-index of silicon that make the devices very sensitive to even nanometer scale dimensional errors. Advanced fabrication technique by reducing the systematic displacement error in the scanning electron-beam-lithography system was applied in making second-order microring resonator filters, where the average frequency mismatch between adjacent microrings was improved from -8.6GHz to

0.28GHz. Novel silicon photonic filters based on the sampled Bragg grating techniques were also demonstrated where arbitrary filter shapes can now be realized from uniform gratings which possess the best nano-scale accuracy thanks to the excellent coherence provided by the interference lithography.

The great benefit of silicon photonics lies in its potential to make use of the well-established complementary metal-oxide-semiconductor (CMOS) technology to realize large-scale integration on a chip. A large-scale integration of more than 4,000 silicon photonic units in an optical phased arrays was presented, taking advantage of the state-of-the-art CMOS technology. All of the 64×64 silicon photonic nanoantennas were balanced in power and aligned in phase to function as a silicon photonic system that create intricate holographic patterns in the far field. Active phased arrays with the ability to project dynamic patterns were also demonstrated, showing a possible pathway to achieve truly 3-dimensional holographic displays. Besides the immediate applications enabled by this large-scale silicon photonic phased array technology such as Laser Detection And Ranging (LADAR), optical tweezers, biomedical sensing, *etc*, the successful integration of more than 4,000 silicon photonic elements shows the incredible integration capability of silicon photonics that has never been demonstrated before. With this large-scale integration ability together with the well-established CMOS technology, large-scale integration of silicon photonics to form functional systems such as on-chip optical interconnections can be envisioned and an era of silicon photonics is truly on the horizon.

7.2 Future Work

The advantage of the sampled Bragg grating structure is its ability to accurately control the resonant frequency of filters. This could find potential applications in wavelength-division-multiplexing (WDM) laser arrays, where the wavelength spacing needs to be accurately controlled to as narrow as 0.25nm. The SBG structure is in particular suitable for this demanding task as indicated by Equation 3.36.

Using the Erbium doped glass as the cladding layer to provide optical gain when pumped with a 980nm laser, a technique that has revolutionized the long-haul optical communication in the last century, an SBG-based WDM laser array can be made in a silicon chip together with other silicon photonic components to enable an on-chip WDM optical interconnection system, as shown in Fig. 7-1. This on-chip WDM system combines the advantage of silicon to transmit and process light and the advantage of low-loss SiN at the pump wavelength (980nm) to create lasers with Erbium doped cladding [7]. The WDM laser array can be made by the proposed quarter-wave phase-shifted SBG to achieve a series of precise lasing wavelengths, and the wavelengths are then modulated, transmitted, and detected in the silicon photonic platform. This integration approach has the unique advantage in that it generates multiple wavelengths by use a single laser input at 980nm, which to a large extent eases the packaging and reduces the cost of the on-chip WDM system.

In the active phased array, the phase tuning is achieved by a delay line with thermo-optic tunability. Although this tuning mechanism is straightforward to implement, it has some disadvantages in that a relatively high power is needed and the tuning speed is on the scale of ~ μs. This is not suitable when the power budget is limited in the system or high tuning-speed is required. The development of other phase tuning mechanisms could further improve the performances of active phased arrays in terms of power consumption and speed, for example, by use of microelectromechanical devices or liquid crystals. Figure 7-2 shows an alternative approach to active change the phase of light. In a microring or microdisk that is overly coupled to a waveguide, the phase of the transmitted light changes from 0 to 2π around the resonance, as shown by Fig. 7-2(a). By changing the resonant wavelength of the microring or the microdisk, the phase of the transmitted light at the working wavelength can thus be modified from 0 to 2π. The resonant wavelength can be realized by thermo-optic effect through an embedded silicon heater as shown in Fig. 7-2(b), as well as the plasma dispersion effect through a *p-n* junction as shown in Fig. 7-2(c). This provides a more power-efficient way

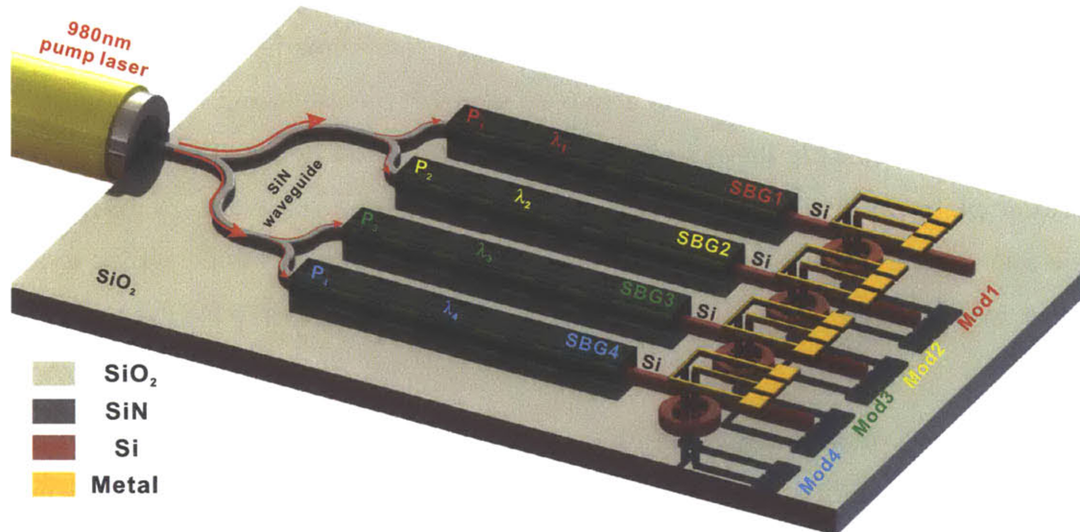

Figure 7-1 Potential application of the SBG-based quarter-wave phase-shift array for the on-chip optical wavelength division multiplexing (WDM) communication. This on-chip system combines two compatible materials: SiN is used to generate WDM lasers and Si is used to transmit and process light. The gain of the lasers is provided by Erbium(Er) doped glass cladding fed by a 980nm pump laser. SiN is used in the laser part to avoid absorption of the pump light in silicon. The SBG array provides multi-wavelength laser output from a single 980nm input light. Silicon is used to modulate light to communicate with other components on the chip.

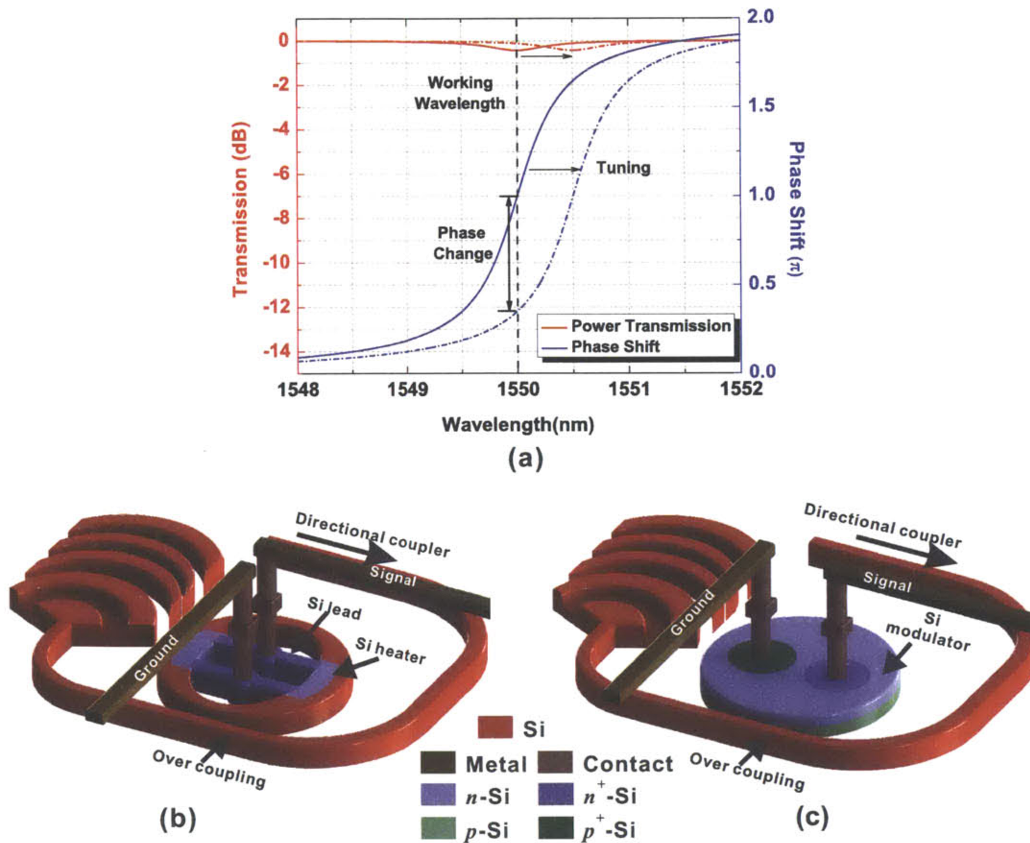

Figure 7-2 (a) In an over-coupled resonant structure, the phase of the transmitted light can be actively changed by almost 2π while maintaining a constant amplitude by shifting the resonant wavelength. This could be potentially used as the phase-tuning mechanism in phased arrays. The resonant structure could be (b) a microring resonator whose resonance is controlled by the thermo-optic effect through a thermal heater integrated in the microring, or (c) a micodisk resonator whose resonance is shifted by the plasma dispersion effect through a *p-n* junction in the micro disk.

to change the phase of light since resonant structures magnify the phase change by having light travel in the structure for a longer time which is controlled by the coupling efficiency. Through this method, especially the plasma dispersion effect shown in Fig. 7-2(c), ultra-fast beam steering can be realized, an enabling technique for applications such as the free space optical switching, *etc*. However, the challenge in this tuning mechanism lies in the fact that it is hard to align all of the microrings or microdisks in the phased array to the same resonant wavelength because of the fabrication errors. This problem could potentially be mitigated by the fabrication approach described in Chapter 2.

Other future work of the large-scale phased array includes its applications in holographic display where visible light can be used instead of the infrared wavelength as used in this work, the optical space division multiplexing where the phased array can be used to excite high-order modes of fiber, and the optical tweezer where the beams generated from the phased array can be used to handle particles like ions and molecules.

Bibliography

[1] R. Soref, "The past, present, and future of silicon photonics," *IEEE J. Sel. Topics Quantum Electron.* **12**, 1678-1687 (2006).

[2] K. K. Lee, D. R. Lim, L. C. Kimerling, J. Shin, and F. Cerrina , "Fabrication of ultralow-loss Si/SiO_2 waveguides by roughness reduction," *Opt. Lett.* **26**, 1888-1890 (2001).

[3] A. Biberman, M. J. Shaw, E. Timurdogan,J. B. Wright, and M. R. Watts, "Ultralow-loss silicon ring resonators," *Opt. Lett.* **37**, 4236-4238 (2012).

[4] Y. A. Vlasov, and S. J. McNab, "Losses in single-mode silicon-on-insulator strip waveguides and bends," *Opt. Express* **12**, 1622-1631 (2004).

[5] H. Rong, A. Liu, R. Jones, O. Cohen, D. Hak, R. Nicolaescu, A. Fang, and M. Paniccia, "An all-silicon Raman laser," *Nature* **433**, 292-294 (2005).

[6] A. W. Fang, H. Park, O. Cohen, R. Jones, M. J. Paniccia, and J. E. Bowers, "Electrically pumped hybrid AlGaInAs-silicon evanescent laser," *Opt. Express* **14**, 9203-9210 (2006).

[7] E. H. Bernhardi, H. A. G. M. van Wolferen, L. Agazzi, M. R. H. Khan, C. G. H. Roeloffzen, K. Wörhoff, M. Pollnau, and R. M. de Ridder, "Ultra-

narrow-linewidth, single-frequency distributed feedback waveguide laser in Al_2O_3:Er^{3+} on silicon," *Opt. Lett.* **35**, 2394-2396 (2010).

[8] R. E. Camacho-Aguilera, Y. Cai, N. Patel, J. T. Bessette,M. Romagnoli, L. C. Kimerling, and J. Michel, "An electrically pumped germanium laser," *Opt. Express* **20**, 11316-11320 (2012).

[9] J. Liu, X. Sun, R. Camacho-Aguilera, L. C. Kimerling, and J. Michel, "Ge-on-Si laser operating at room temperature," *Opt. Lett.* **35**, 679-681 (2010).

[10] M. S. Dahlem, C. W. Holzwarth, A. Khilo, F. X. KŁrtner, H. I. Smith, and E. P. Ippen, "Reconfigurable multi-channel second-order silicon microring-resonator filter banks for on-chip WDM systems," *Opt. Express* **19**, 306-316 (2011).

[11] M. A. Popović, T. Barwicz, M. R. Watts, P. T. Rakich, L. Socci, E. P. Ippen, F. X. Kärtner, and H. I. Smith, "Multistage high-order microring-resonator add-drop filters," *Opt. Lett.* **31**, 2571-2573 (2006).

[12] R. A. Soref, and B. R. Bennett, "Electrooptical effects in silicon," *IEEE J. Quant. Electron.* **23**, 123-129 (1987).

[13] E. Timurdogan, C. M. Sorace-Agaskar, A. Biberman, and M. R. Watts, "Vertical junction silicon microdisk modulators at 25Gb/s," *Proc. Opt. Fiber Commun. Conf.*, paper OTh3H (2013).

[14] Q. Xu, B. Schmidt, S. Pradhan, and M. Lipson, "Micrometre-scale silicon electro-optic modulator," *Nature* **435**, 325-327 (2005).

[15] M. R. Watts, D. C. Trotter, R. W. Young, and A. L. Lentine, "Ultralow power silicon microdisk modulators and switches," *Proc. 5th IEEE Int. Conf. Group IV Photonics*, 4-6 (2008).

[16] C. T. DeRose, D. C. Trotter, W. A. Zortman, A. L. Starbuck, M. Fisher, M. R. Watts, and P. S. Davids, "Ultra compact 45 GHz CMOS compatible Ger-

manium waveguide photodiode with low dark current," *Opt. Express* **19**, 24897-24904 (2011).

[17] L. Vivien, J. Osmond, J. Fédéli, D. Marris-Morini, P. Crozatl, J. Damlencourt, E. Cassan, Y. Lecunff, and S. Laval, "42 GHz p.i.n Germanium photodetector integrated in a silicon-on-insulator waveguide," *Opt. Express* **17**, 6252-6257 (2009).

[18] C. W. Holzwarth, R. Amatya, M. Dahlem, A. Khilo, F. X. KŁrtner, E. P. Ippen, R. J. Ram, and Henry I. Smith, "Fabrication strategies for filter banks based on microring resonators," . *Vac. Sci. Technol. B* **26**, 2164-2167 (2008).

[19] J. V. Hryniewicz, P. P. Absil, B. E. Little, R. A. Wilson, and P. T. Ho, "Higher-order filter response in coupled microring resonators," *IEEE Photon. Technol. Lett.* **12**, 320-322 (2000).

[20] Y. Yanagase, S. Suzuki, Y. Kokubun and S.T. Chu, "Box-like filter response and expansion of FSR by a vertically triple coupled microring resonator filter," *IEEE J. Lightwave Technol.* **20**, 1525-1529 (2002).

[21] B. E. Little, S. T. Chu, H. A. Haus, J. Foresi, and J. P. Laine, "Microring resonator channel dropping filters," *IEEE J. Lightwave Technol.* **15**, 998-1005 (1997).

[22] H.I. Smith, T. Barwicz, C.W. Holzwarth, M.A. Popović, M.R. Watts, P.T. Rakich, M. Qi, R. Barreto, F.X. K'artner, and E.P. Ippen, "Strategies for fabricating strong-confinement microring filters and circuits," *Proc. Opt. Fiber Commun. Conf.*, paper OThC2 (2007).

[23] T. Barwicz, M. A. Popović. P. T. Rakich, M. R. Watts, H. A. Haus, E. P. Ippen, and H. I. Smith, "Microring-resonator-based add-drop filters in SiN: fabrication and analysis," *Opt. Express* **12**, 1437-1442 (2004).

[24] T. Barwicz, M. A. Popović, M. R. Watts, P. T. Rakich, E. P. Ippen and H. I. Smith, "Fabrication of Add-Drop Filters Based on Frequency-Matched Microring Resonators," *IEEE J. Lightwave Technol.* **24**, 2207-2218 (2006).

[25] S. Xiao, M. H. Khan, H. Shen, and M. Qi, "Compact silicon microring resonators with ultra-low propagation loss in the C band," *Opt. Express* **15**, 11467-14475 (2007).

[26] M. R. Watts, T. Barwicz, M. A. Popović, P. T. Rakich, L. Socci, E. P. Ippen, H. I. Smith, and F.X. K′artner, "Microring-resonator filter with doubled free-spectral-range by two-point coupling," *Conference on Lasers and Electro-Optics (CLEO)*, paper CMP3 (2005).

[27] C. W. Holzwarth, T. Barwicz, M. A. Popović, P. T. Rakich, E. P. Ippen, F. X. K′artner, and H. I. Smith, "Accurate resonant frequency spacing of microring filters without postfabrication trimming," *J. Vac. Sci. Technol. B* **24**, 3244-3247 (2006).

[28] E. H. Anderson, V. Boegli, M. L. Schattenburg, D. Kern, and H. I. Smith, "Metrology of electron-beam lithography systems using holographically produced reference samples," *J. Vac. Sci. Technol. B* **9**, 3606-3610 (1991).

[29] J. G. Goodberlet, J. T. Hastings, and H. I. Smith, "Performance of the Raith 150 electron-beam lithography system," *J. Vac. Sci. Technol. B* **19**, 2499-2502 (2001).

[30] J. Sun, C. W. Holzwarth, M. Dahlem, J. T. Hastings, and H. I. Smith, "Compact silicon microring resonators with ultra-low propagation loss in the C band," *Opt. Express* **16**, 15958-15963 (2008).

[31] B. E. Little, "A variational coupled-mode theory including radiation loss for grating-assisted couplers," *IEEE J. Lightw. Technol.* **14**, 188-195 (1996).

[32] T. E. Murphy, "Design, fabrication and measurement of integrated Bragg grating optical filters," *Ph.D. Thesis*, Massachusetts Institute of Technology, Cambridge MA (2000).

[33] K. A. Winick, and J. E. Roman "Design of corrugated waveguide filters by Fourier-transform techniques," *IEEE J. Quantum Electron.* **26**, 1918-1929 (1990).

[34] J. Sun, Y. Dai, X. Chen, Y. Zhang, and S. Xie "Thermally tunable dispersion compensator in 40-Gb/s system using FBG fabricated with linearly chirped phase mask," *Opt. Express* **14**, 44-49 (2006).

[35] Y. Dai, X. Chen, L. Xia, Y. Zhang, and S. Xie "Sampled Bragg grating with desired response in one channel by use of a reconstruction algorithm and equivalent chirp," *Opt. Lett.* **29**, 1333-1335 (2004).

[36] K. Utaka, S. Akiba, K. Sakai, and Y. Matsushima, "$\lambda/4$-shifted InGaAsP/InP DFB lasers," *IEEE J. Quantum Electron.* **22**, 1042-1051 (1986).

[37] S. Akiba, M. Usami, and K. Utaka; , "1.5μm $\lambda/4$-shifted InGaAsP/InP DFB lasers," *J. Lightw. Technol.* **5**, 1564-1573 (1987)

[38] Y. Dai, X. Chen, D. Jiang, S. Xie and C. Fan, "Equivalent phase shift in a fiber Bragg grating achieved by changing the sampling period," *IEEE Photon. Technol. Lett.* **16**, 2284-2286 (2004).

[39] J. Li, H. Wang, X. Chen, Z. Yin, Y. Shi, Y. Lu, Y. Dai, and H. Zhu, "Experimental demonstration of distributed feedback semiconductor lasers based on reconstruction-equivalent-chirp technology," *Opt. Express* **17**, 5240-5245 (2009)

[40] J. Sun, C. W. Holzwarth, and H. I. Smith, "Phase-Shift Bragg Grating in Silicon Using Equivalent Phase-Shift Method," *IEEE Photon. Technol. Lett.* **24**, 25-27 (2012).

[41] T. Barwicz, C. W. Holzwarth, P. T. Rakich, M. A. Popović, E. P. Ippen, and H. I. Smith, "Optical loss in silicon microphotonic waveguides induced by metallic contamination," *Appl. Phys. Lett.* **92**, 131108 (2008).

[42] K. F. Braun, "Electrical oscillations and wireless telegraphy," *Nobel Lecture* (1909)

[43] R. L. Haupt, *Antenna arrays: a computational approach*, Wiley, New Jersey, 2010.

[44] R. W. Gerchberg, and W. O. Saxton, "A practical algorithm for the determination of phase from image and diffraction plane pictures," *Optik* **35**, 237-246 (1972).

[45] M. Cherry, "Astronomy in South Africa: the long shot," *Nature* **480**, 308-309 (2011).

[46] P. J. Schuck, D. P. Fromm, A. Sundaramurthy, G. S. Kino, and W. E. Moerner, "Improving the mismatch between light and nanoscale objects with gold bowtie nanoantennas," *Phys. Rev. Lett.* **94**, 017402 (2005).

[47] A. Alù, and N. Engheta, "Tuning the scattering response of optical nanoantennas with nanocircuit loads," *Nature Photon.* **2**, 307-310 (2008).

[48] L. Tang, S. E. Kocabas, S. Latif, A. K. Okyay, D. Ly-Gagnon, K. C. Saraswat, and D. A. B. Miller, "Nanometre-scale germanium photodetector enhanced by a near-infrared dipole antenna," *Nature Photon.* **2**, 226-229 (2008).

[49] A. Yaacobi, E. Timurdogan, and M. R. Watts, "Vertical emitting aperture nanoantennas," *Opt. Lett.* **37**, 1454-1456 (2012).

[50] P. Mühlschlegel, H.-J. Eisler, O. J. F. Martin, B. Hecht, and D. W. Pohl, "Resonant optical antennas," *Science* **308**, 1607-1609 (2005).

[51] T. Kosako, Y. Kadoya, and H. F. Hofmann, "Directional control of light by a nano-optical Yagi-Uda antenna," *Nature Photon.* **4**, 312-315 (2010).

[52] G. Roelkens, D. Van Thourhout, and R. Baets. "High efficiency silicon-on-insulator grating coupler based on a poly-silicon overlay," *Opt. Express* **14**, 11622-11630 (2006).

[53] D. Taillaert, P. Bienstman, and R. Baets, "Compact efficient broadband grating coupler for silicon-on-insulator waveguides," *Opt. Lett.* **29**, 2749-2751 (2004).

[54] F. Van Laere, G. Roelkens, M. Ayre, J. Schrauwen, D. Taillaert, D. Van Thourhout, T. F. Krauss, and R. Baets, "Compact and highly efficient grating couplers between optical fiber and nanophotonic waveguides," *IEEE J. Lightwave Technol.* **25**, 151–156 (2007).

[55] M. Fan, M. A. Popović, and F. X. K′artner, "High directivity, vertical fiber-to-chip coupler with anisotropically radiating grating teeth," *Conference on Lasers and Electro-Optics (CLEO)*, paper CTuDD3 (2007)

[56] A. Taflove, and S. C. Hagness, *Computational Electrodynamics: The Finite-Difference Time-Domain Method*, Artech House, Boston MA, 3rd edition, 2005.

[57] P. F. McManamon, T. A. Dorschner, D. L. Corkum, L. J. Friedman, D. S. Hobbs, M. Holz, S. Liberman, H. Q. Nguyen, D. P. Resler, R. C. Sharp, E. A. Watson, "Optical Phased Array Technology," *Proc. IEEE* **84**, 268- 298 (1996).

[58] R. A. Meyer, "Optical beam steering using a multichannel lithium tantalite crystal," *Appl. Opt.* **11**, 613-616 (1972).

[59] D. P. Resler, "High-efficiency liquid-crystal optical phased array beam steering," *Opt. Lett.* **21**, 689-691 (1996).

[60] W. Ng, A. A. Walston, G. L. Tangonan, J. J. Lee, I. L. Ncwberg, and N. Bernstein, "The first demonstration of an optically steered microwave phased array antenna using true-time-delay," *IEEE J. Lightwave Technol.* **9**, 1124-1131 (1991).

[61] D. Kwong, A. Hosseini, Y. Zhang, and R. T. Chen, "1×12 unequally spaced waveguide array for actively tuned optical phased array on a silicon nanomembrane," *Appl. Phys. Lett.* **99**, 051104 (2011).

[62] N. W. Carlson, G. A. Evans, R. Amantea, S. L. Palfrey, J. M. Hammer, M. Lurie, L. A. Carr, F. Z. Hawrylo, E. A. James, C. J. Kaiser, J. B. Kirk, and W. F. Reichert, "Electronic beam steering in monolithic grating-surface-emitting diode laser arrays," *Appl. Phys. Lett.* **53**, 2275-2277 (1988).

[63] J. K. Doylend, M. J. R. Heck, J. T. Bovington, J. D. Peters, L. A. Coldren, and J. E. Bowers, "Two-dimensional free-space beam steering with an optical phased array on silicon-on-insulator," *Opt. Express* **19**, 21595-21604 (2011).

[64] K. Van Acoleyen, H. Rogier, and R. Baets, "Two-dimensional optical phased array antenna on silicon-on-insulator," *Opt. Express* **18**, 13655-13660 (2010).

[65] K. Van Acoleyen, W. Bogaerts, J. Jágerská, N. Le Thomas, R. Houdré, and Roel Baets, "Off-chip beam steering with a one-dimensional optical pahsed array on silicon-on-insulator," *Opt. Lett.* **34**, 1477-1479 (2009).

[66] J. Sun, E. Timurdoğan, A. Yaacobi, E. shah Hosseini, and M. R. Watts, "Large-scale nanophotonic phased array," *Nature* **493**, 155-159 (2013).

[67] M. Padgett, J. Courtial, and L. Allen, "Lights orbital angular momentum," *Phys. Today* **57**, 35-40 (2004).

[68] C. Xia, N. Bai, I. Ozdur, X. Zhou, and G. Li, "Supermodes for optical transmission," *Opt. Express* **19**, 16653-16664 (2011).

[69] M. R. Watts, W. A. Zortman, D. C. Trotter, R. W. Young, and A. L. Lentine, "Low-voltage, compact, depletion-mode, silicon MachZehnder Modulator," *IEEE J. Sel. Top. Quantum Electron.* **16**, 159-164 (2010).

[70] F. Gan, T. Barwicz, M. A. Popović, M. S. Dahlem, C. W. Holzwarth, P. T. Rakich, H. I. Smith, E. P. Ippen, and F. X. Kärtner, "Maximizing the thermo-

optic tuning range of silicon photonic structures," *Photonics in Switching*, 67-68 (2007).

[71] M. R. Watts, "'Adiabatic microring resonators,' *Opt. Lett.* **35**, 3231-3233 (2010).

[72] C. T. DeRose, M. R. Watts, R. W. Young, D. C. Trotter, G. N. Nielson, W. Zortman, and R. D. Kekatpure, "Low power and broadband 2×2 silicon thermo-optic switch," *Proc. Opt. Fiber Commun. Conf.*, paper OThM3 (2011).